THE UNIVERSITY OF CHICAGO

ENGINEERED METABOLITES & EFFEROCYTIC BRIDGE PROTEIN ANTIGEN FUSIONS FOR THE MODULATION OF IMMUNE PHENOTYPE & DISEASE PATHOLOGY IN CHRONIC INFLAMMATORY DISEASE

A DISSERTATION SUBMITTED TO
THE FACULTY OF THE DIVISION OF THE BIOLOGICAL SCIENCES
IN CANDIDACY FOR THE DEGREE OF
DOCTOR OF PHILOSOPHY

COMMITTEE ON MOLECULAR METABOLISM & NUTRITION

BY
TARYN NOELLE BECKMAN

CHICAGO, ILLINOIS
AUGUST 2025

Abstract

Butyrate is a gut microbiome-derived short chain fatty acid with pleiotropic favorable effects on inflammation and metabolism. In murine models of atherosclerosis, butyrate has been shown to significantly reduce atherosclerotic lesions, rectify routine metabolic parameters such as low-density lipoprotein cholesterol (LDL-C), and reduce systemic inflammation. However, its foul odor, rapid metabolism in the gut and thus low systemic bioavailability, limit its therapeutic effectiveness. Our laboratory has engineered an ester-linked L-serine-conjugate to butyrate (SerBut) to mask its taste and odor and to co-opt amino acid transporters in the gut to increase its systemic bioavailability as determined by tissue measurements of free butyrate, produced by hydrolysis of SerBut. In vitro, SerBut maintains the anti-inflammatory, NFκB-suppressing capacity of butyrate while allowing higher dosing without cytotoxicity. In an apolipoprotein-E (ApoE)$^{-/-}$ mouse model of atherosclerosis, SerBut reduced systemic LDL-C and pro-inflammatory cytokines, plaque burden in the aortic root, and monocytes in the aorta. In addition, SerBut suppressed circulating liver injury markers and early steatosis in the liver. SerBut overcomes several barriers to the translation of butyrate and shows superior promise in slowing atherosclerosis and liver injury than equidosed sodium butyrate.

Efferocytosis maintains homeostasis by suppressing secondary necrosis and promotes immune tolerance through propagation of TAM receptor signaling. Growth arrest-specific 6 (GAS6), a bridge protein mediating efferocytosis through TAM receptors, has been implicated in regulation of inflammatory cycles. However, the mechanism of tolerogenic antigen presentation is incompletely understood. To unravel the interplay between an efferocytic antigen, the dendritic cell (DC) collecting it, and the T cell engaged in that immune synapse, we engineered a GAS6 bridge protein by fusing it to the model antigen ovalbumin yielding GAS6-OVA (GO), providing an experimental tool enabling characterization of efferocytic myeloid-lymphoid signaling. A non-PS-binding proteoform of GO (ΔGO) distinguished be-

tween effects mediated by TAM receptor signaling alone or associated with apoptotic debris. GO induced tolerogenic antigen presentation by both MHC-I and MHC-II under both homeostatic and inflammatory conditions, resulting in antigen-specific tolerance including Treg proliferation and terminal exhaustion of $CD8^+$ T cells. Flow cytometry revealed reciprocal tolerogenic polarization by both myeloid and lymphoid sides of the immune synapse. GO pre-exposure ameliorated inflammatory airway pathology in a murine model, demonstrating functional potency of the GAS6-mediated tolerogenic pathway with an endogenous repertoire. Thus, when antigen is collected and presented via the GAS6-mediated pathway of efferocytosis, reciprocal tolerogenic antigen presentation occurs by both MHC-I and MHCII in a PS binding dependent manner regardless of inflammatory conditions.

Dedicated to moms, sisters, and best girlfriends.

"I am a thing which thinks, that is to say, which doubts, which affirms, which denies, which knows a few things, which is ignorant of many, which loves, which hates, which ills, which rejects, which imagines also, and which senses. For as I have previously remarked, although the thing which I sense and which I imagine are perhaps nothing at all apart from me and in themselves, I am nonetheless sure that those modes of thought which I call sensations and imaginations, only just as far as they are modes of thought, reside and are found with certainty in myself."

Rene Descartes, *First Meditations on Philosophy. Meditation Three.*

TABLE OF CONTENTS

LIST OF FIGURES

LIST OF TABLES

ACKNOWLEDGMENTS

There are many people that have given to me without expectation of reciprocation. This generosity has shaped me and my desire to contribute to the pursuit of knowledge and the application of that knowledge to bettering the quality of life of people like me. Although the list below is non-exhaustive, thank you for your support, trust, and belief in me. I hope this work lives up to the expectations of my mentors, funding sources, and family. I will continue to try and make you proud.

I want to thank my mentor and PI, Jeffrey Hubbell. There was no better match for me in this process. I am unbelievably proud to be a student of yours and to contribute to your future.

I want to thank my mentor, Lisa Volpatti. Working closely with you changed the course of my PhD. In addition to producing diligent and high quality science, you are incredibly morally principled.

I want to thank my committee: Eugene Chang, Yun Fang, and Ada Weinstock. Few scientists have had the wonderful experience of getting to work closely with each of their committee members. I have the utmost respect for each of your bodies of work and am honored to be evaluated by you. I have felt incredibly supported throughout my PhD by each of you, from early rotations in the Chang and Fang lab to hours of discussion with Ada in the Weinstock lab.

I want to thank the coauthor of Chapters 3 and 4 of this dissertation, Joe Reda. Working with you on the GO project has been an incredible growing and learning experience for me. My PhD training would be incomplete without the experience. I hope for many more years of intellectual collaboration!

I want to thank my Family, Dave, Deb, Robben, Diandrea, and Trent Beckman. I feel so fortunate to have been led by example. Any diligence, work ethic, or resilience I have developed would not have happened without you. Thank you for supporting me and

encouraging me to live my dreams!

I want to thank my boyfriend, Henderson Heussner. You make me feel like i'm right here on my two feet without a need in the world! I love hearing about what you think and what you want to do today, tomorrow, and in 50 years. You have taken wonderful care of me over this fun, at times all consuming, challenge. I love you so much, everyday is lighter with you!

I want to thank my friends; Hallie Moore, Rankin Hobbs, Abby Garrett, Sissy Davis, Dylan Haugenes, Haily Macdonald, and Sarah Cella. Your acceptance and support of me at my worst makes you my closest confidants at my best. My identity is in our friendship and our memories. Failure doesn't feel so scary when I know that no matter what a single martini with you all would make it unimportant. I find so much fulfillment and purpose in being your friend!

I want to thank the women that helped me and befriended me during my PhD; Abigail Laughterbach and Anna Slezak. When I met you both I knew I wanted to be just like you, and I still aspire to that goal! There are few people like us, and it makes our sisterhood feel rare and impossible to replicate. I owe so much of my success to both of you, and the entirety of my happiness for the first 2 years of graduate school at the very least.

CHAPTER 1

A BRIEF EXPLINATION OF IMMUNOMETABOLIC INFLUENCE ON CHRONIC DISEASE

1.1 Physiology and Relevant Biochemistry

1.1.1 The Gut

Amino Acid Absorption and Transport in the Gastrointestinal Tract

Unlike some other food molecules, most amino acids are immediately released into circulation and distributed to peripheral tissues. Postprandial metabolism refers to metabolism after a meal. Postprandial absorption and metabolism of amino acids can be highly dependent on varying biological and experimental conditions including the assessment window. Daily absorption of protein, as amino acids or peptides, in the intestine exceeds the amount of protein consumed throughout the day due to recycling of endogenous proteins. This can be up to 170 g in humans, 1.7X more than average protein consumed in developed countries. Proteins are broken down in both the gastric fluid and at the brush border of the intestine by peptidases(1). Specific transporters for amino acids and peptides are found in the enterocytes of the small intestine, absorbing mainly in the proximal jejunum(2) (Figure 1.1). Although significant transport capacity can be found in other parts of the intestine, only about 5% of protein absorption occurs in the colon including those amino acids generated by the microbiome and endogenous recycling. Absorbed amino acids are taken up by specific apical transporters, further digested in the case of peptides, and released into circulation via the basolateral membrane(1, 3)(Figure 1.1).

Thus, the small intestine is an important contributor to plasma amino acid homeostasis and amino acid transport in the large intestine is more relevant for bacterial metabolites or fluid secretion. The distinct roles are due to the basolateral membrane expression of amino acid transporters, which only transport amino acids into circulation in the small intestine. This can be seen in apical versus basolateral amino acid transporter expression along the intestine. In the murine intestine, although expression of apical amino acid transporter $ATB^{+,0}$ increases in expression in the distal gut, basolateral amino acid transporter LAT2

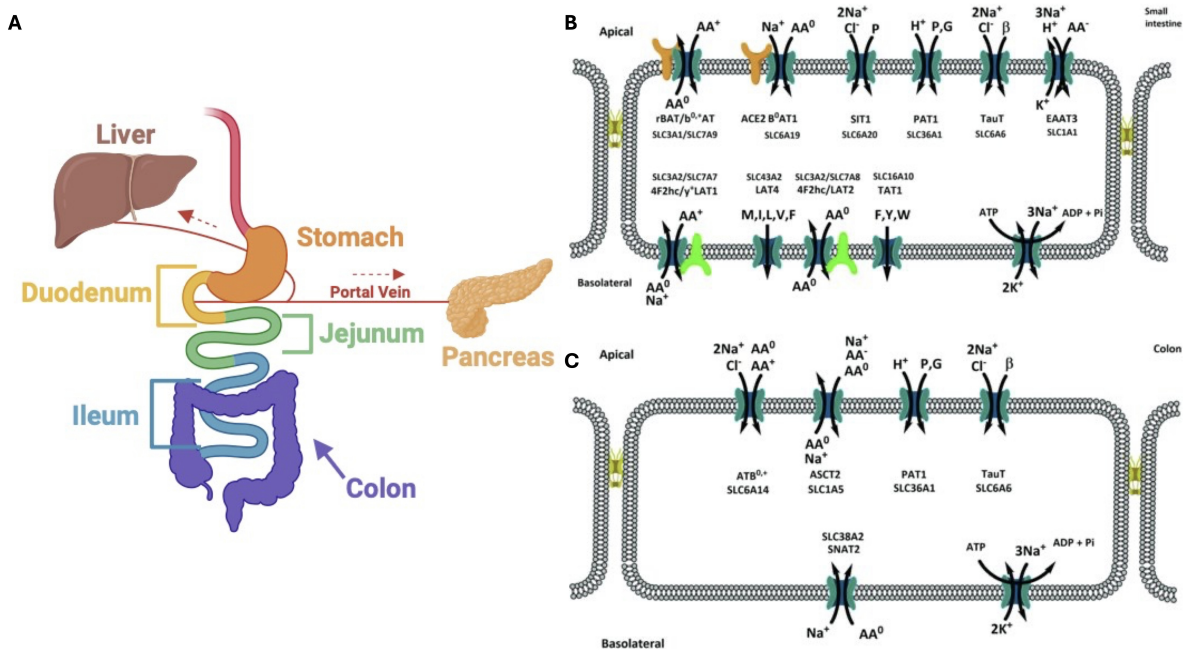

Figure 1.1: **Amino Acid Transport in the Human IntestineA.** Schema of the human intestinal system. Made with Biorender.com **B.** Small Intestine.**C.** Colon. The apical membrane is shown at the top, the basolateral membrane at the bottom. Arrows indicate preferential direction of transport. For explanations, see text. Transporter acronyms are shown. AA^0, neutral amino acids, AA^+, cationic amino acids, AA^-, anionic amino acids. Tau, taurine; β, beta-amino acids, P, proline; G, glycine. B and C are figures from Broer et al. 2019. Comprehensive Physiology.

reduces inhibiting amino acid entry into circulation (Figure 1.2). Thus, the expression of basolateral amino acid transporters restricts the sections of the gut that either contribute to systemic amino acid homeostasis or stimulate gut specific effects. Recent work from Bhatia et al exemplifies the alternative role of apical membrane amino acid transport in the distal gut and establishes a cause-and-effect relationship between increased food intake/obesity and SLC6A14 in knock-out mice (Figure 1.2). This work found the ATB textsuperscript+,0 transporter to regulate appetite by stimulating secretion of GLP-1 when amino acids in the distal small intestine are sensed(3)

Amino acid transporters are organized as solute carrier (SLC) families (Table 1). Amino acid transporters can also be organized by "systems", an older nomenclature still used, where system A (alanine) carriers small and polar neutral amino acids and system ASC carries alanine, serine, and cysteine. Amino acid transporters are promiscuous, accepting amino acids with a range of similar biophysical properties. In this introduction we will focus on the transport of neutral amino acids due to this dissertation's emphasis on small polar amino acid, L-Serine.

System	**SLC**	**AA substrates**	**Affinity**	**Mech.**	**Ions**	**Expression**
A	38A2	G,P,A,Q,C,N,M*	Med	Symp	Na	Ubiquitous
	38A4	G,A,S,C,Q,N,NH_3,AA_+	Med	Symp	Na	Kidney
ASC	1A5	A,S,C,T	High	Anti	Na	Kidney/Intestine (AM)
	1A5	A,S,C,T,Q,N	High	Anti	Na	Kidney/Intestine(AM)
$b^{0,+}$	3A1	G,A,S,C,T	High	Anti	-	Kidney/Intestine(BM)
B	6A19	$AA^{0,+}$, $B^{0,+}$, bAla	High	Symp	Na,Cl^-	Intestine(MA)
y^+L	3A2	AA^+, AA^0	Med	Anti	Na	Kidney/Intestine(AM)
L	7A8	AA except P	Med	Anti	-	–
N	38A5	Q,N,H,S,G	Low	Symp	Na	Kidney/Intestine(BM)

Table 1.1: Amino Acid Transport Systems that can Transport Serine

Neutral amino acid transport is dependent on sodium ion coupled transport, with substrate affinity increasing with the length of the hydrophobic side chains and hyperpolarization. Km (the Michaelis constant) values ranged from 1-16 mmol/L. SLC6A19 (B^0AT1)

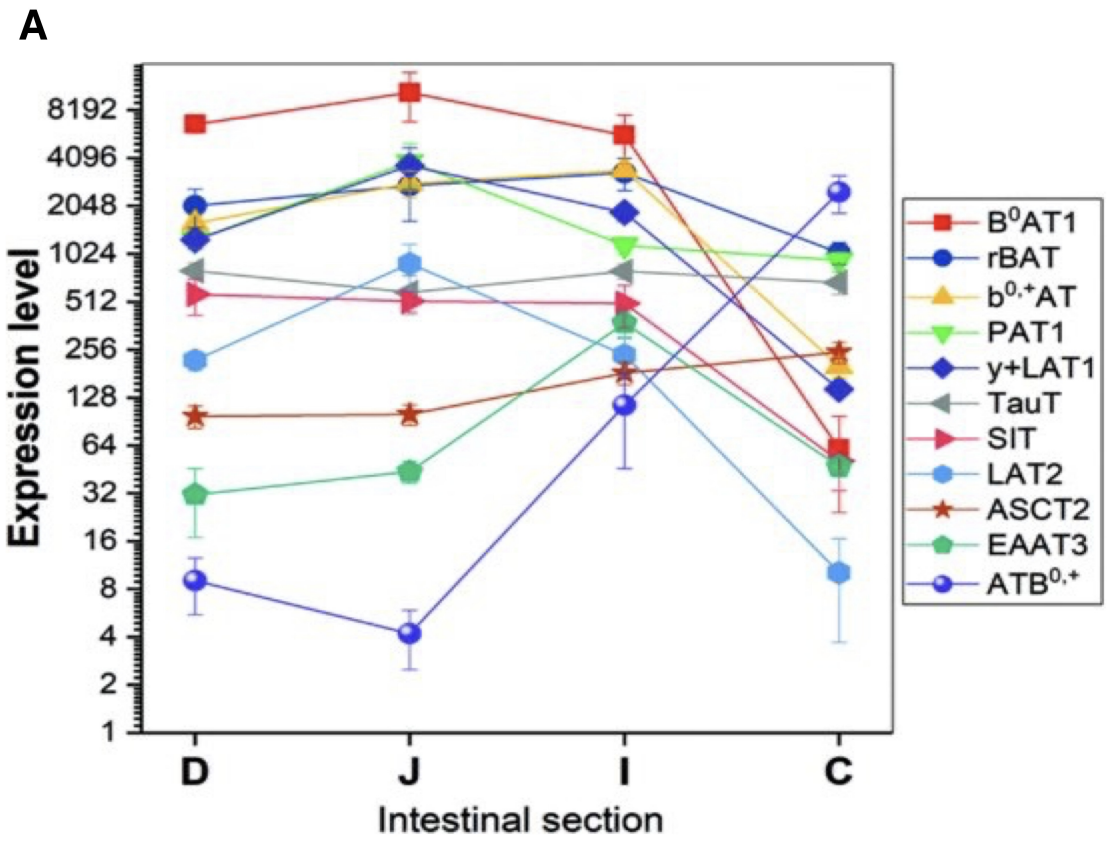

Figure 1.2: **Amino Acid Transporter Expression in the Murine Intestine A.** Expression of amino acid transporters along the mouse intestine. Expression data were extracted from microarray data deposited in GEO datasets GDS 521, 522, and 524. A log2 scale is used for transporter expression due to large differences in mRNA abundance. B^0AT1, $b^{0,+}AT$, y+LAT1, LAT2, rBAT, SIT1, and PAT1 show the typical signature for transporters primarily involved in amino acid absorption (high in the small intestine, low in colon). $ATB^{0,+}$ and ASCT2 show the opposite distribution. EAAT3 and TauT1 show a more even distribution along the intestine. Figure from Broer et al. 2019. Comprehensive Physiology

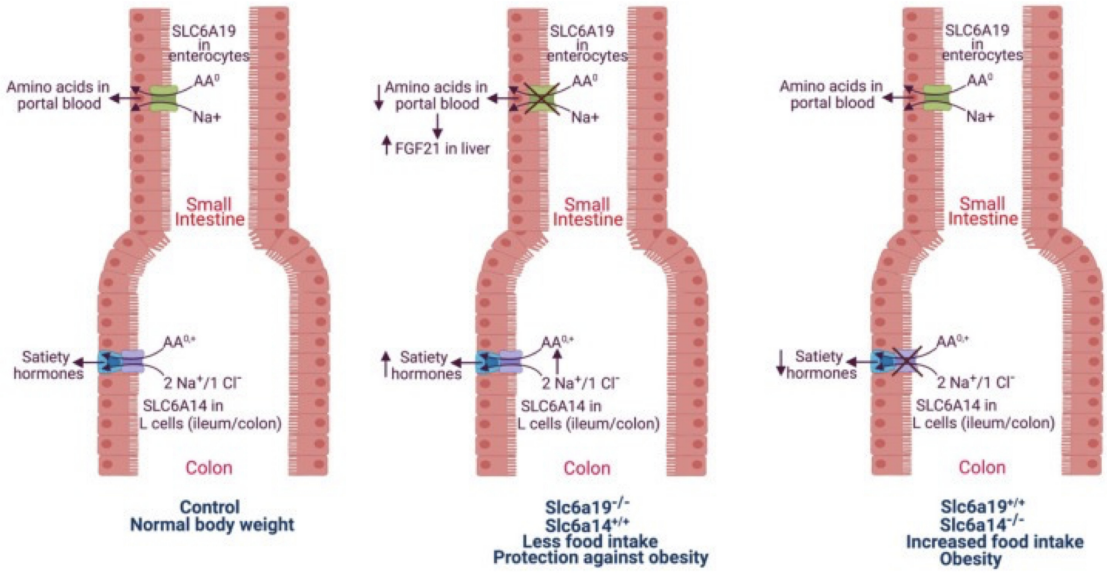

Figure 1.3: **Differing Roles of Apical Amino Acid Transport in The Small Intestine and the Colon A.** Functional crosstalk between SLC6A19 in the proximal small intestine and SLC6A14 in ileum and colon in the control of food intake and body weight. AA0, neutral amino acids; AA0,+, neutral and cationic amino acids; FGF21, fibroblast growth factor 21. Data from Bhutia Y.D. et al, Biomolecules, 2022. 235.

transports all neutral amino acids with varying efficacy due to affinity differences in substrates. The maximal rate (Vmax) values are similar, but affinities are reduced as amino acids get shorter or bulkier. Substrate affinity is highest for methionine and branched-chain amino acids followed by glutamine, asparagine, phenylalanine, cysteine, serine, glycine, tyrosine, threonine, histidine, proline, and finally tryptophan with the lowest affinity. Postprandial absorption of methionine and the other branched amino acids (Isoleucine, leucine, and valine) have the most rapid absorption rates after intestinal perfusion. Lower affinities are seen for compounds without an α-amino group, compounds with the α-hydrogen substituted by a methyl group, D-compounds, compounds with tertiary branching in the sidechain, compounds with either a positive or negative charge in the side chain, and in the majority of cases, compounds with a hydrophilic moiety in the side chain(4)

Beneficial Molecules from Bacteria in the Distal Gut

Complex carbohydrates are a network of monosaccharides linked together; they are in foods ranging from ultra-processed cosmic brownies to fibrous vegetables like broccoli. Cells cannot access the energy in these carbohydrates until they hydrolyze the bonds that hold the sugar units together. Many complex carbohydrates that are unsubstituted at their reducing ends are referred to as polysaccharides. Polysaccharides include the oligosaccharides of milk, the cellulose of plant cell walls, and storage forms such as starch and glycogen. Other complex carbohydrates are covalently connected to other molecules, such as proteins or lipids, by glycosidic linkages of the sugar residues at their reducing ends to form glycoconjugates.

There are two types of glycosidic linkages, alpha and beta. Alpha(1-4) bonds are the bonds found in glycogen and starch. They are characterized by a hydroxyl group (OH) on the anomeric carbon below the plane of the ring. In cellulose, the glycosidic bond found is called a Beta bond because the hydroxyl group on the anomeric carbon is in the beta position above the plane of the ring. Hydrolysis of glycosidic bonds is catalyzed by enzymes that are

highly specific in the type of linkage they can cleave. Humans mostly have enzymes that cleave alpha glycosidic linkages, with one exception. Lactase hydrolyzed the beta glycosidic bond between glucose and galactose in lactose (a sugar found in milk). Lactose intolerance is cause by a lack of this enzyme, or the disruption of the feed forward loop that stimulates its transcription. Thus, some complex carbohydrates bound by beta linkages cannot be broken down my endogenous enzymes due to the glycosidic linkages holding them together. Humans can derive nutrition from fibrous plants due to breakdown of the beta glycosidic bonds in plant walls by bacteria in the microbiome.

In this way,the microbiome influences the quality of the diet. Intestinal microbiome communities also have massive impacts on sustaining immune homeostasis and protecting against pathogens. Beta-glucans, complex carbs bound by beta glycosidic linkages, can bind to receptors on immune cells and initiate an immune response. Pathogen associated molecular pattern (PAMP) receptors on dendritic and macrophage cells recognize beta-glucans and can alert the immune system of, for example, a fungal infection or a pathologic bacterial infection. However, the relationship is two-sided. Diet can also structure the microbiome.

The bacteria in the microbiome produce substances during their own metabolism that are fundamental to human health. Dietary supplementation of indigestible polysaccharides from plants, fungi, and probiotics benefits health by promoting microbial community growth and producing metabolites of bacterial fermentation in the colon. Bacterial fermentation is confined to the colon, or distal gut, because it requires an anerobic environment. Bacterial fermentation produces short chain fatty acids (butyrate, acetate, and propionate), biogenic amines (ex. serotonin, histamine, and dopamine), indole and tryptophan derivatives, and secondary bile acids. These bacterial byproducts have complex and intensely studied benefits on human health. Short chain fatty acids have been found to play roles in immune cell proliferation and differentiation, chemotaxis, apoptosis, and gene expression. This dissertation will focus on the immunomodulatory and metabolic effects of butyrate, a short chain fatty

acid.

1.1.2 The Liver

The liver is made of hepatocytes, hepatic stellate cells, Kupffer cells, and liver sinusoidal endothelial cells (LSECs). These cell types are highly organized and spatiotemporally regulate liver function. There are many channels carrying blood and bile throughout the liver. Blood from the digestive tract enters the liver through the portal vein into the liver where its contents can be processed by hepatocytes. After processing, nutrients or processed drugs can be passed back into circulation or excreted. Many drugs are known to be metabolized by the liver, mainly by cytochrome p450 enzymes or carboxylesterases. The main cell type of the liver, hepatocytes, makes up approximately 70% of the mass of the liver. Hepatocytes perform lipid metabolism, drug metabolism, and secrete coagulation and immune complement factors. Kupffer cells are the resident macrophage cells in the liver. Hepatic stellate cells, although a very infrequent cell type, play a central role in vitamin A and lipid storage. Hepatocytes are highly regulated by neighboring Kupffer cells and, in an inflamed state, other infiltrating immune cells.

The liver can break down fat for energy, take up blood glucose via GLUT2 transporters, and produce bile. After a meal, the liver switches very quickly from burning fat as energy (Beta oxidation) to taking in glucose and storing excess as glycogen via glycogenesis. Bile is released into the stomach and allows for the breakdown and absorption of fats. The GLUT2 transport allows the liver to regulate blood sugar after a meal. This transporter, as opposed to GLUT4, has a low affinity for glucose. Thus, the liver absorbs sugar proportional to the concentration in the blood, only allowing it to uptake excess or high concentration glucose. This glucose can then be stored as glycogen for future use. Inversely, when hypoglycemia occurs, the liver stimulates break down of glycogen and releases the resulting glucose into the blood stream. The liver is the primary organ that converts excess glucose into lipids.

The liver can then store this extra energy as a lipid droplets or form lipoproteins to allow the circulation of the lipids for consumption by peripheral tissues.

Kuffner cells respond to inflammatory stimuli by secreting inflammatory cytokines (IL-6, IL-1β,TNFα, IL-10, IL-4), growth factors, and reactive oxygen species (ROS) that induce hepatic liver injury. Hepatic liver injury can be diagnosed with circulating enzymes Alanine transaminase (ALT) and Aspartate transaminase (AST). ALT and AST are normally contained within hepatocytes, but when they are damaged these enzymes can be released. Acute liver damage activates differentiation of hepatic stellate cells to myofibroblast-like cells that play a role in the development of liver fibrosis. LSECs assist in regeneration post injury.

An Brief Explanation Lipoproteins and Lipoprotein Packaging

Cholesterol and lipids are insoluble in water; thus, they must travel through the body protected from the surrounding soluble blood(5). This is done through association with proteins. Lipoproteins are heterogeneous particles containing cholesterol esters and triglycerides surrounded by free cholesterol, phospholipids, and apolipoproteins. They circulate hydrophobic lipids throughout the body, allowing muscle and adipose tissue to cleave lipids off as needed by lipoprotein lipase enzyme. Apolipoproteins facilitate lipoprotein formation and function. Plasma lipoproteins can be divided into seven classes based on size, lipid composition, and apolipoproteins (chylomicrons, chylomicron remnants, VLDL, VLDL remnants (IDL), LDL, HDL, and Lp (a)) (Figure 1.4). Chylomicron remnants, VLDL, IDL, LDL, and Lp (a) are all proatherogenic while HDL is not atherogenic. HDL is sometimes considered anti-atherogenic, however this claim has not been substantiated by clinical trials where HDL was increased, but cardiovascular events were not reduced(6-8). Apolipoproteins have four major functions including 1) serving a structural role, 2) acting as ligands for lipoprotein receptors, 3) guiding the formation of lipoproteins, and 4) serving as activators or inhibitors of enzymes involved in the metabolism of lipoproteins(9).

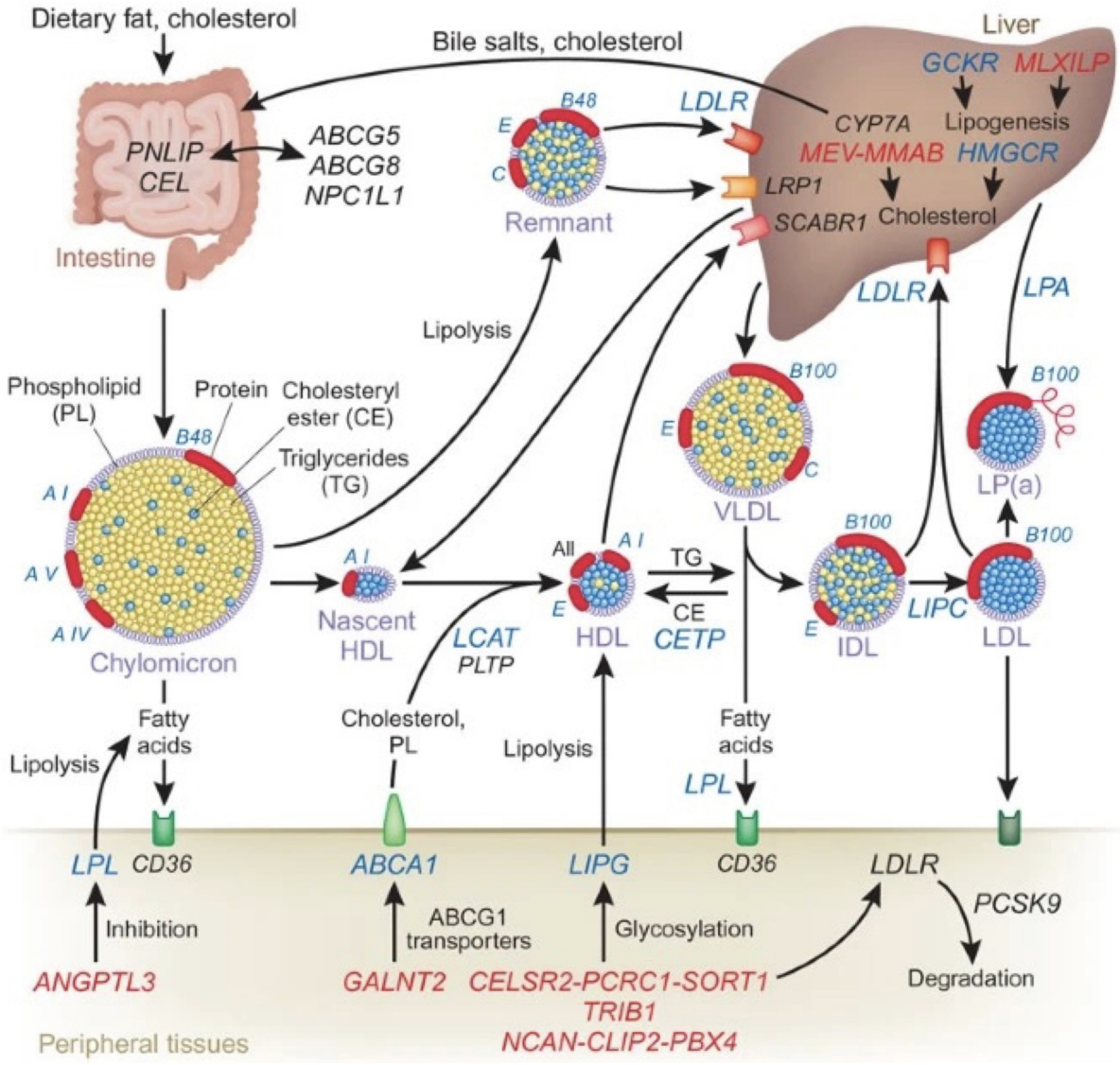

Figure 1.4: **Triglyceride (TG)-rich lipoproteins are secreted by intestine (chylomicrons) and liver (VLDL).** lipoproteins deliver fatty acids to tissues via lipolysis in circulation. Chylomicron remnants and a portion of the VLDL remnants are then taken up by the liver. The remainder of the VLDL remnants is further metabolized to cholesterol-rich LDL, which constitutes the main cholesterol carrying particles in humans. HDL is formed in the circulation from lipid-poor apolipoproteins secreted by liver and intestine and from surface components sloughed during lipolysis of TG-rich lipoproteins. Shown in blue are genes confirmed to contribute to common variations in the concentrations of the major lipoproteins. Shown in red are the loci or genes newly identified in genome-wide association studies. Figure from Lusis & Pajukata et al. 2008. Nature Genetics.

Chylomicrons are the first lipoprotein to form from exogenous lipids when dietary lipids are absorbed in the intestine. Chylomicrons travel through lymph fluid and circulate. The liver creates VLDL, or very low-density lipoprotein, from endogenous lipids created by de novo lipogenesis. When a lipoprotein has been emptied by tissues, it is called a chylomicron remnant. Chylomicron remnants circulate until they are returned to the liver, where the endogenous production of lipoproteins and de novo lipids begins. Lipoproteins can return to the liver by association with lipoprotein receptors. These receptors can mediate cell to lipoprotein lipid transfer (reverse cholesterol transport) (ex. ABCA1), or mediate uptake of lipoprotein to utilize the lipids inside (ex. LDL-R). Receptors also exist to mediate the transfer of lipids lipoprotein to lipoprotein (ex. CEPT) (Figure 1.4). The IDL are further metabolized to LDL, which are taken up by the LDL receptor in numerous tissues including the liver, the predominant site of uptake. Reverse cholesterol transport begins with the formation of nascent HDL by the liver and intestine. These small HDL particles can then acquire cholesterol and phospholipids that are effluxed from cells, a process mediated by ABCA1 resulting in the formation of mature HDL(10, 11). Mature HDL can acquire addition cholesterol from cells via ABCG1, SR-B1, or passive diffusion. The HDL then transports the cholesterol to the liver either directly by interacting with hepatic SR-B1 or indirectly by transferring the cholesterol to VLDL or LDL, a process facilitated by CETP. Cholesterol efflux from macrophages to HDL plays an important role in protecting from the development of atherosclerosis.

low density lipoprotein receptor (LDL-R) is the most common receptor mediating endocytic uptake of lipoproteins. LDL-R is expressed in the liver and most other tissues. LDL-R recognizes apolipoproteins Apo B-100 and ApoE, allowing it to mediate endocytosis of lipoproteins containing these apolipoproteins (LDL, chylomicron remnants and IDL). Endocytosis of lipoprotein leads to release of the contained cholesterol into the cell after lysosomal degradation. This inhibits de novo lipogenesis by downregulating HMG CoA re-

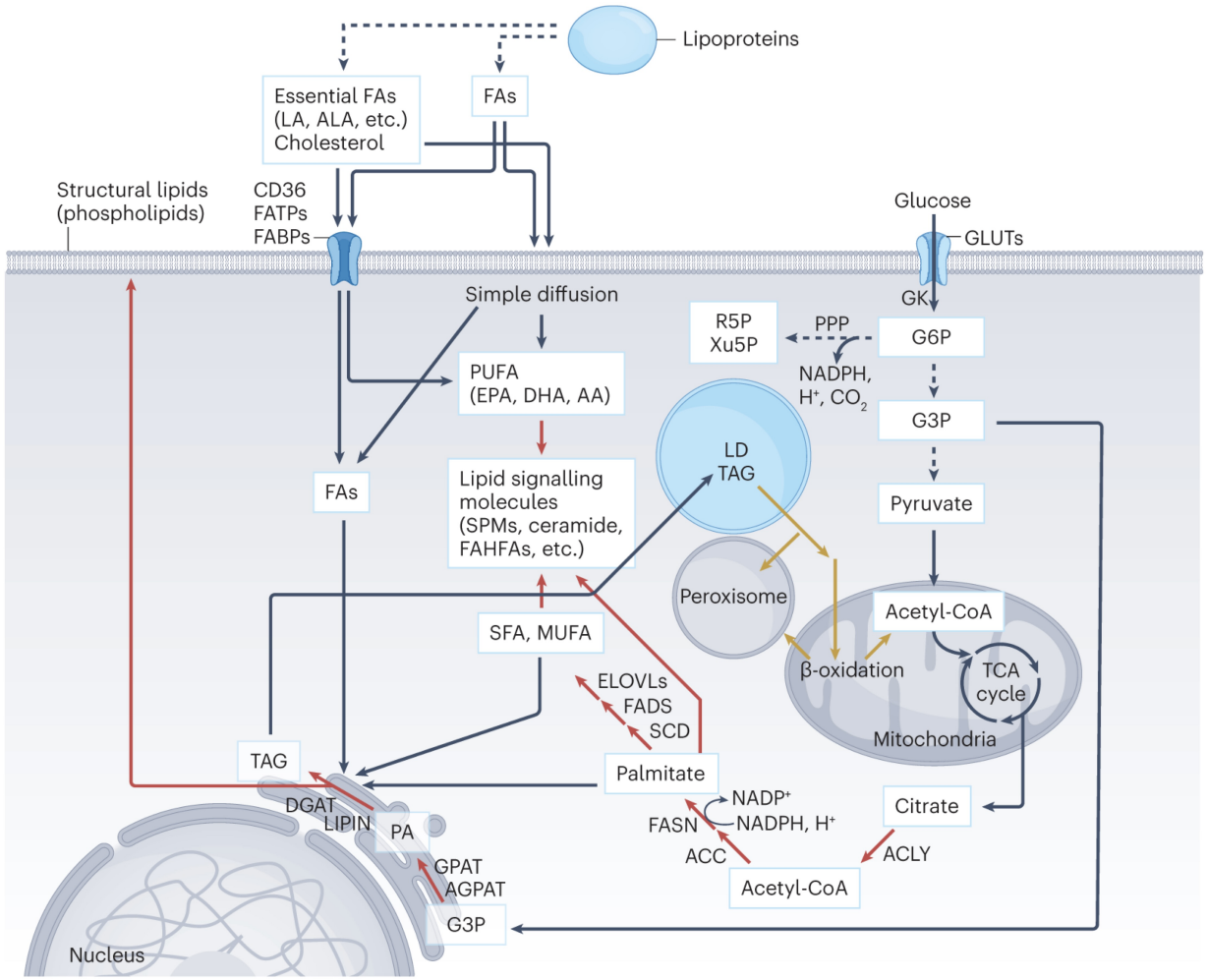

Figure 1.5: **Overview of the major lipid metabolism pathways involved in lipid uptake, lipogenesis and lipid degradation via fatty acid oxidation.** Fatty acids are converted from carbohydrates through glycolysis and the TCA cycle in mitochondria, and are taken up by various pathways, such as passive diffusion and transport by lipoproteins and fatty-acid-binding proteins. Cellular fatty acids are stored as TAGs in LDs, and certain fatty acids function as signalling mediators and structural lipids. The lipids stored in LDs are catabolized to meet energy demands by interacting with mitochondria and peroxisomes. Orange arrows represent the anabolic pathways of lipids, whereas grey arrows indicate the catabolic pathways. AA, arachidonic acid; ACC, ACC1; ACLY, ATP citrate synthase; AGPAT, 1-acylglycerol-3-phosphate-O-acyltransferase; ALA, α-linolenic acid; CD36, cluster of differentiation 36; DHA, docosahexaenoic acid; EPA, eicosatetraenoic acid; ELOVLs, elongation of very-long-chain fatty acid proteins; FAs, fatty acids; FABPs, fatty-acid-binding proteins; FAHFA, fatty acid esters of hydroxy fatty acid; FATPs, fatty-acid-transport proteins; G3P, glyceraldehyde-3-phosphate; LA, linoleic acid; MUFA, monounsaturated fatty acid; PA, phosphatidic acid; PPP, pentose phosphate pathway; R5P, ribose-5-phosphate; SPM, specialized pro-resolving mediator. Figure and figure caption from Jeon et al. 2023. Nature Metabolism.

ductase (the rate limiting enzyme of de novo lipogenesis), other pathway related enzymes, and the expression of LDL receptors on the surface. Thus, the number of LDL receptors is regulated by the amount of cholesterol in the cells. In this way, cholesterol in the cell regulates the amount of LDL-R on the surface, and the amount of circulating LDL is influenced by the expression of LDL-R. Logically, increased expression of LDL-R is associated with reduced circulating LDL. Statins, or HMG-CoA reductase inhibitors, not only halt endogenous lipid production, but also increase the expression of LDL-R on the liver's surface. Statins competitively bind to the active site of HMG-CoA reductase with higher affinity than its substrate, thus reducing its activity. This results in reduced intracellular cholesterol in the hepatocyte, stimulating an upregulation of LDL-R on the surface. Most circulating cholesterol is hepatically produced rather than taken up through diet, so this mechanism also reduces circulating LDL.

De Novo Lipogenesis: Fatty Acid Synthesis, Cholesterol Synthesis, & Lipid Storage

De novo lipogenesis is the process by which a cell makes their own lipid, either fatty acid or cholesterol. This process occurs after a meal in a well-fed state in order to start the storage of excess energy as triglycerides. The TCA cycle intermediate, Citrate, is the starting molecule for all de novo lipogenesis. Citrate is converted to acetyl-CoA by the enzyme ACLY (ATP-citrate lyase). Fatty acid synthesis produces fatty acids form cytoplasmic acetyl-Coa. Cytoplasmid Acetyl-CoA can be derived from glucose (glycolysis), glutamine (glutaminolysis to TCA cycle), or acetate. Next, seven acetyl-CoAs are converted to malonyl CoA via ACACA. Fatty Acid synthase (FASN) then produces one palmitic acid (C16:0) per one acetyl-CoA and seven malonyl-CoAs. Palmitic acid is saturated with hydrogens but can be desaturated and converted to monounsaturated fatty acids (MUFAs).

In many cells, these lipids are then catabolized by a multistep process called fatty acid

oxidation in the mitochondria for energy. This process is rate limited by the carnitine shuttle that transports acetyl-CoA across the double mitochondrial membrane. Carnitine palmitoyltransferase 1(CPT1a) is the rate limiting enzyme of this shuttle and is located on the outer mitochondrial membrane. Thus, fatty acids must be activated prior to shuttling by being attached to an Acyl-Coa, forming fatty acyl-CoA by the enzyme fatty acyl-CoA synthase (ACSL). CPT1a is inhibited by malonyl-CoA, the second step in fatty acid synthesis. This makes physiological sense because most cells prefer to use glycolysis for energy, so in a fed state the cell turns off beta oxidation. In the liver and adipose tissue however, MUFAs can be stored as a lipid droplet thanks to their expression of the enzyme glycerol phosphate acyl transferase (GPAT). GPAT catalyzes the formation of triglycerides (12). Continual excess energy storage can lead to the benign fatty liver, the early stages of non-alcoholic fatty liver disease (NAFLD)(13).

Liver Immunity in Cardiometabolic Disease

Cardiometabolic disease in the liver takes the form of nonalcoholic fatty liver disease (NAFLD). NAFLD is a range of disorders beginning with simple steatosis, a benign form of fatty liver. Further progression can lead to non-alcoholic steatohepatitis (NASH) and cirrhosis. Chronic liver inflammation tips the balance between NAFLD and NASH. Low-grade continual production of proinflammatory cytokines, including tumor necrosis factor (TNF), interleukin-6 (IL-6), and IL-1β perpetuates hepatic regeneration, resulting in fibrosis that compromises immunosurveillance, progressing NASH(14).

Liver macrophages are a heterogeneous mix of myeloid-derived immune cells. Under homeostatic conditions, liver-resident embryonically derived Kupffer cells are the main myeloid derived cell, which are characterized by their high phagocytic activity and sensing capacity for damage- and pathogen-associated molecular patterns (DAMPs and PAMPs). Kupfer cells respond to damage signals and can promote liver inflammation through the release of proin-

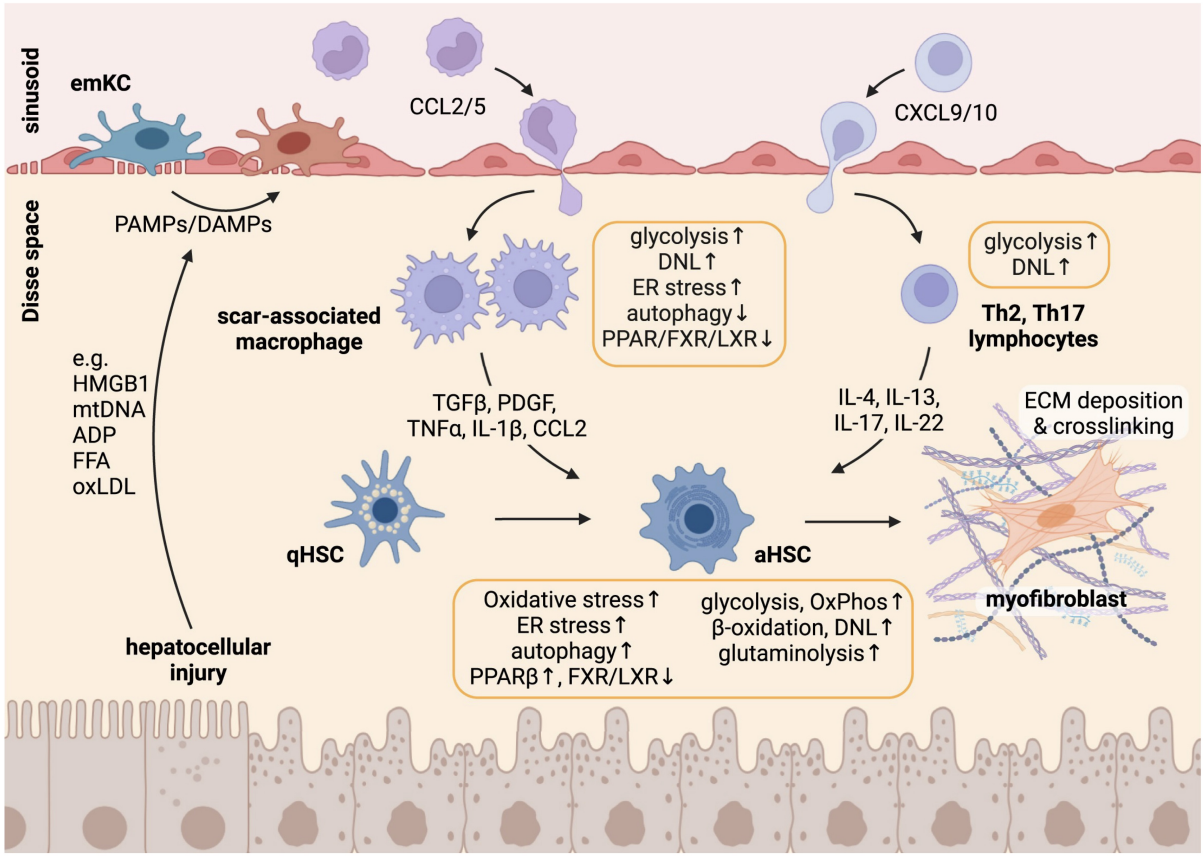

Figure 1.6: **General mechanisms of liver fibrosis and main metabolic adaptations in macrophages, lymphocytes, and activated hepatic stellate cells.** Hepatocellular injury initiates liver inflammation through the release of damage-associated signals. These signals, as well as cytokines and chemokines released by activated embryonic Kupffer cells (emKCs), recruit circulating immune cells to the liver, where they undergo pronounced phenotypical changes. Monocytes differentiate into inflammatory, scar-associated macrophages, and the adaptive immune response shifts toward Th2/17 immunity. Cytokines, growth factors, and damage-associated signals eventually drive the activation of quiescent hepatic stellate cells (qHSCs) toward an activated (aHSC), proliferative, extracellular matrix (ECM)-producing and contractile myofibroblast-like phenotype. Phenotypical changes are accompanied and dependent on pronounced metabolic adaptations, including increased glycolysis, activation of lipogenic pathways, and metabolic stress responses, including oxidative and endoplasmic reticulum stress, as well as autophagy and ferroptosis, and changes in nuclear receptor signaling. ADP, adenosine diphosphate; CCL, C-C motif ligand; CXCL, C-X-C motif ligand; DAMPs, damage-associated molecular patterns; DNL, de novolipogenesis; ER, endoplasmic reticulum; FFA, free fatty acid; FXR, farnesoid X receptor; HMGB1, high mobility group box 1; (q/a)HSC, (quiescent/activated) hepatic stellate cell; IL, interleukin; LXR, liver X receptor; MMP, matrix metalloproteinase; mtDNA, mitochondrial DNA; oxLDL, oxidized low-density lipoprotein; OxPhos, oxidative phosphorylation; PAMPs, pathogen-associated molecular patterns; STAT-3, signal transducer and activator of transcription 3; PPAR, peroxisome proliferator-activated receptor; TGF-β, transforming growth factor beta. Figure and Figure caption from Horn & Tacke et al. 2024. Cell Metabolism.

flammatory cytokines such as IL-1β and TNFα. Other myeloid-derived populations come from inflammatory circulating monocytes (Ly6C^{high}) that differentiate into macrophages once recruited to the liver. This population is highly plastic and can take on a range of phenotypes and functions.

During fibrosis, which can occur even after acute liver injury, or after repeated injury due to toxins, insulin-resistance associated metabolic dysfunction, autoimmune conditions, or chronic infections, CD9textsuperscript+TREM2(triggering receptors expressed on myeloid cells 2)$^{+}$ scar-associated macrophages (CAM) have been identified as the main drivers in human chronic liver injury(15). SAMs can then secret pro-inflammatory factors such as IL-1β, TNFα, Platelet growth factor (PDGF). These factors then activate hepatic stellate cells (HSCs) to produce collagen, thus promoting liver fibrosis. Infiltrating macrophages can take on a pro-resolving phenotype, secreting matrix metalloproteinases and growth factors. Furthermore, these resolving infiltrating macrophages have a high efferocytosis capacity to clear debris and dead cells, promoting fibrosis regression. High levels of efferocytosis on infiltrating TREM2^{+} macrophages allow for the clearing of apoptotic lipid laden hepatocytes(16).

It is generally established that inflammatory macrophages are characterized by increased glycolysis and tricarboxylic acid cycle (TCA) due to their needs to quick energy (Figure 1.7). In contrast anti-inflammatory pro-regenerative macrophages utilize beta oxidation and activation of arginase 1 pathway to meet their energy needs(17). High glycolytic activity can also be required for efferocytosis in regenerative macrophages. Importantly, in inflammatory macrophages, the TCA is broken after citrate and succinate and decoupled from OxPhos. Due to this uncoupling, succinate accumulates and promotes the production of IL-1β by HIF1α signaling(18). As previously mentioned, under starvation states hepatocytes use lipids as energy via the beta oxidation pathway in the mitochondria. The byproducts of this process are ketone bodies via ketogenesis, which links beta-oxidation pathways with ketogenic amino acids (ex. Acetoacetate, Beta-hydroxybutyrate). These ketone bodies can

be an energy source to hepatic macrophages under conditions of glucose starvation, to feed the TCA cycle. There is potentially a role for ketone body production by hepatocytes and consumption by macrophages in liver fibrosis. Studies have shown that injection of acetoacetate can inhibit extracellular matrix deposition (ECM) in murine NASH models(19). Macrophages can signal back to hepatocytes; resident liver macrophages were shown to stimulate ketogenesis in hepatocytes during fasting via glucocorticoid receptor (GR) activation mediated suppression of TNFα secretion allowing GR/peroxisome proliferator-activated receptor α (PPARα) target gene activation in hepatocytes(20).

Similar to atherosclerosis progression, lipid accumulation and lipotoxic stress strongly influence inflammatory macrophage differentiation and activation. The inflammatory macrophage phenotypes of macrophages associated with multiple cardiometabolic diseases, including atherosclerosis, NASH, and obesity-related adipose tissue dysfunction, are similar when analyzed by proteomics. There is high transcriptional similarity between lipid-associated macrophages (LAMs) in human steatohepatitis(21). In steatohepatitis, efferocytic LAMs can limit inflammation by containing DAMPs and other inflammatory signals by organizing in a "crown like structure" around apoptotic hepatocytes. In prolonged injury, macrophages lose their efferocytotic functions due to toxic lipid signaling, ultimately fueling the progression to fibrosis rather than containing inflammation(16). These macrophages then secrete TNF-α and IL-1β, inhibiting beta-oxidation in hepatocytes and perpetuating liver toxicity(22).

1.1.3 The Heart

Atherosclerosis and Cardiovascular Disease:

Cardiovascular disease kills more than 17 million people a year and is the leading cause of death in the US(23). Atherosclerosis is a chronic immunometabolic disease that is the leading cause of cardiovascular disease. In its earliest phase, the disease is driven by retention of

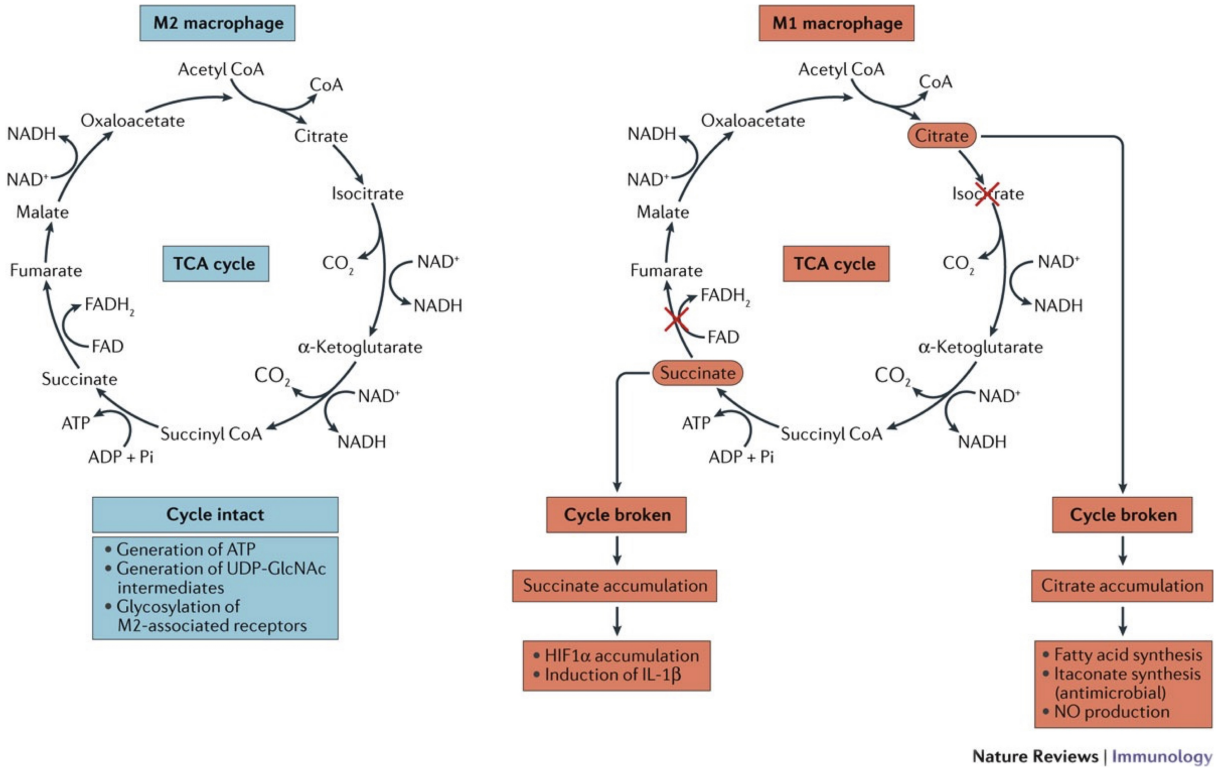

Figure 1.7: **Immunometabolism Influence on Macrophage Polarization** In M2-like macrophages (that is, interleukin-4 (IL-4)-activated macrophages) the tricarboxylic acid (TCA) cycle is intact and participates in oxidative phosphorylation, providing ATP for energy. In M1-like macrophages (that is, cells that have been activated by lipopolysaccharide (LPS) and interferon-γ), the TCA cycle is broken in two places — after citrate and after succinate. Citrate is used to generate fatty acids for membrane biogenesis and also for prostaglandin production. It also generates itaconic acid via the enzyme immune-responsive gene 1 (IRG1). Itaconic acid has direct antimicrobial activity against Mycobacterium tuberculosis and Salmonella sp. HIF1α, hypoxia-inducible factor 1α. Figure and Figure caption from O'Neill et al. 2016. Nature reviews Immunology.

cholesterol-rich, apolipoprotein B (ApoB)-containing lipoproteins at sites of disturbed blood flow, such as bifurcations in arteries (24). High levels of plasma low density lipoprotein (LDL)-cholesterol is considered the most significant risk factor for promoting development and progression of atherosclerosis. Lipoproteins accumulate in the arterial wall and undergo oxidation and carbamylation. Vascular endothelial cells are then activated both physically, by the disturbed flow at the branched region, and chemically, by these modified lipoproteins. Activated vascular endothelial cells express adhesion molecules that bind and recruit circulating innate and adaptive immune cells such as monocytes and T cells(25). Following initial lipoprotein deposition and oxidation in the subendothelial space, tissue-resident immune cells become activated, and monocytes are recruited to the early lesions(26).

Thus, monocytes are rare in a healthy artery(24). During atherosclerosis progression, once inside the intima, monocytes differentiate into macrophages and uptake modified lipoproteins(26). This transforms macrophages into cholesterol-laden foam cells. Macrophages in the plaque express scavenger receptors that take up modified lipoprotein antigens, such as oxidized LDL (oxLDL). Oxidized LDL can activate the NFB pathway in recruited monocytes, resulting in the upregulation of pro-inflammatory genes, such as adhesion molecules, chemokines, and cytokines (e.g., IL-1α/β, IL-6, and IL-12)(27). For example, monocyte-chemoattractant protein-1 (MCP-1), also known as C-motif chemokine ligand 2 (CCL2), regulates inflammatory monocyte trafficking between the bone marrow, circulation, and atherosclerotic plaques by binding to its cognate receptor CCR2 on immune cells and endothelial cells. Upon uptake of excess oxidized LDL, monocytes differentiate into lipid-laden foam cells, which become dysfunctional and contribute to the formation of necrotic core in later stages of plaque development(26). Foam cells secrete enzymes that degrade the extracellular matrix (ECM), leading to less plaque stability and higher likelihood of plaque rupture. When plaque ruptures, platelets aggregate, blood coagulates, and thrombus formation occurs(28). Plaque stability can also be modulated by inflammatory cytokines released

by immune cells. Inflammatory cytokines signal an immune response inside the plaque that kills vascular smooth muscle cells, destabilizing plaque. Many other cells and organs contribute to the immunometabolic dysregulation during atherosclerosis development, creating a complex and interdependent disease.

1.2 Current Approaches to Treating Cardiovascular Disease.

1.2.1 Cholesterol Lowering Medications.

Cholesterol lowering medications aim to lower levels of low-density lipoprotein (LDL) and triglycerides and increase high density lipoprotein (HDL)(29). The most frequently used are statins, or HMG CoA reductase inhibitors, followed by cholesterol absorption inhibitors (CAIs). Statins reduce the amount of cholesterol circulating in the blood. However, statins can elevate liver enzymes and thus cannot be taken by patients with active liver disease such as fatty liver disease, a common comorbidity of metabolic syndrome and CVD. Alternatively, CAIs prevent cholesterol from being absorbed in the intestine and are the most used non-statin agent. CAIs are associated with an increased rate of neurocognitive adverse events when compared to the placebo control(30). In a comparative safety and efficacy analysis of lipid lowering agents including over 200,000 patients, PCSK9 (proprotein convertase subtilisin/kexin type 9) inhibitors were the most effective lipid lowering agents, achieved similar CV benefits to statins, and circumvented any increased risk of statin-related side-effects. Statins ranked first in incidences of statin-intolerance related symptoms, new-onset diabetes, elevated ALT, and creatine kinase (CK) (30). Statin intolerance, a spectrum of symptoms usually in large muscles, exists in 30% of patients based on observational studies and 60% of patients that stop taking statins state statin intolerance as their primary reason(31). Despite the success of these therapies in reducing LDL-C, major adverse cardiovascular events are reduced by less than 50% on these drugs, in addition to their many uncomfortable side

effects(29).

1.2.2 Targeting the innate immune system in CVD.

Disappointing reductions in major adverse cardiovascular events in the clinic with lipid lowering medication treatment is thought to be due to residual inflammatory risk(32). Multiple subsets of innate immune cells play a role in cardiovascular disease including monocytes, innate lymphoid cells, neutrophils, and dendritic cells (24). Several studies have reported a predictive relationship between biomarkers of inflammation (e.g., C-reactive protein) and cardiovascular events, as well as a direct benefit of anti-inflammatory interventions in humans. The innate immune system is a fast-acting, nonspecific, defense against foreign substances(24). The value in treating the innate immune paradigm of atherosclerosis was proven in concept by clinical studies in 2017(33). For example, colchicine, which inhibits the NFκB-regulated NLR family pyrin domain containing 3 (NLRP3) inflammasome, provided proof-of-concept of the benefits of broad immunosuppression (34, 35). Colchicine treatment reduced cardiovascular events but was associated with increased lethal infections at high doses, although it received FDA approval at low doses. At the clinical stage, macrophages and neutrophils, producers of key inflammatory cytokines, are targeted through IL-1 and IL-6 inhibition while at the preclinical stage there are many approaches. These approaches can be broadly categorized into three strategies. The first is inhibition of recruitment and reduction of inflammation in monocytes. The second aims to modulate macrophages in the atherosclerotic lesion by increasing pro-resolving mediators and decreasing pro-inflammatory cytokines. The final approach is restoration of efferocytosis through anti-CD47 antibodies.

IL-1 is a pro-inflammatory cytokine that drives inflammation in atherosclerosis and cardiovascular disease. IL-1 does this through expression of inflammatory cytokines and C-reactive protein (CRP)(36). IL-1 has two isoforms; IL-1α is involved in remodeling arteries in early atherosclerosis development while IL-1β drives vascular inflammation in later dis-

ease(25). The CANTOS study was the first example of successful modulation of IL-1β in atherosclerosis, using an anti-IL-1β antibody(33). The study showed successful reduction in major adverse cardiovascular events, but led to higher incidence of infection in the treatment arm compared to placebo while there was no improvement of overall survival (33). This therapy was not approved and did not meet it's primary endpoint; however, other IL-1 inhibitors have undergone clinical trials for CVD that may be promising in the future (Xilonix, Anakinra)(37, 38).

IL-6, a classically inflammatory cytokine, is involved in the innate immune response and acts as a downstream mediator of cytokine cascades. IL-6 contributes to atherosclerosis plaque destabilization, as well as being correlated with increased risk of myocardial infarction(25). Tocilizumab, a monoclonal antibody against IL- 6, reduced CRP (c-reactive protein) in phase 2 trials(39). Unfortunately, the difference between Tocilizumab and placebo was small enough that clinical relevance may be extremely limited. Current follow-up studies are underway to provide more information on the clinical relevance of IL-6 blockade(25).

With regards to the second preclinical strategy, the challenge of targeting monocytes recruitment is that circulating monocytes traffic into tissues during homeostasis, inflammation, and inflammation resolution. Thus, targeting monocyte recruitment may not be viable or will require frequent monitoring(40). Though there is an example of reduced atherosclerosis in LDLr$^{-/-}$ mice using an already FDA-approved CCR5 antagonist, which disallows monocyte recruitment through the inhibition of chemokine recruitment signaling (41, 42). Additionally, anti-CCR2, an inhibitor of monocyte recruitment, like CCR5, is being investigated(43, 44). Significant to this proposal, histone deacetylase (HDAC) and glucose transporter 1 (GLUT1) inhibitors are currently being investigated as innate immune system modulators at the preclinical stage(45, 46). SerBut, the proposed drug of aim 1, falls under this category(47). Briefly, HDAC inhibitors are epigenetic modulators(48). HDAC3 has physiological implications in energy metabolism while HDAC9 modifies cardiac gene expression and vas-

cular calcification(49). GLUT1 inhibitors are hypothesized to have anti-inflammatory action because leukocytes prefers glucose metabolism in an inflamed state, but have not shown efficacy in preclinical models despite large reduction in circulating monocytes(50). Reprogramming inflammatory macrophages, pushing monocytes towards a pro-resolution phenotype rather than a pro-inflammatory phenotype, has also been relatively successful(51, 52). Macrophage polarization is orchestrated by NFκB, STAT family, PPARγ, and IRF master regulators(51, 53, 54). Pioglitazone is an FDA approved PPARγ agonist that induces pro-resolving macrophage phenotype by reducing proinflammatory cytokine production and promoting monocyte differentiation. IRF5 inhibition with nanoparticles, which also induces a pro-resolving phenotype, has reportedly decreased myocardial infarction size in murine models of CVD(55).

The NLRP3 inflammasome, a cytosolic multiprotein expressed predominantly in innate immune cells, has been shown to be a driver of lipid-driven vascular inflammation and atherosclerosis when activated in monocytes and macrophages(29). Cholesterol loading in macrophages causes inflammasome activation due to cholesterol microcrystals building up inside the cell when the influx of cholesterol overloads the phagocytes' metabolic ability(56). Upon activation, the inflammasome is responsible for the production of IL-1β and IL-18, plaque formation, and increased likelihood of rupture. Colchicine, of the afore mentioned trial, inhibits the NLRP3 inflammasome as well as being a broad immunosuppressive. However, many attempts to target the inflammasome have failed due to liver toxicity.

Oxidized LDL can bind Toll-like receptors (TLRs), a group of pattern recognition receptors that cause proinflammatory signaling. Extracellular TLR2 (Toll-like receptor 2) regulates IL-1β production and is upregulated in human atherosclerotic tissue(57). Deletion of TLR2 consistently reduces lipid deposition and macrophage content in atherosclerotic lesions in mice(58). However, deleterious effects of suppression of the innate immune system have been identified across many chronic inflammatory disease contexts, and cardiovascular

disease is no exception. Innate immune suppression, or broad immunosuppression, leads to reduced protection against infection.

1.2.3 Targeting the adaptive immune system in CVD.

Adaptive immunity has a humoral arm of specific antibodies against an antigen secreted by B cells and a cellular arm of T cells that can activate B cells during co-stimulation or differentiate into effector T cells that make pro or anti-inflammatory cytokines. Adaptive immunity is associated with CVD due to sustained and chronic inflammation(24, 59). Myeloid response over long periods of time is accompanied by the infiltration of many T and B cells into the atherosclerotic plaque, suggesting an autoimmune component of the disease(60). $CD3^+$ T cells recruited by CCR5 contribute to fibrous cap stability(61). $CD4^+$ T cells signal to other immune cells and induce B cell antibody production. Furthermore, inflammation and CVD do not only interact through disease progression. Inflammatory processes seen in IBD (irritable bowel disease) and rheumatoid arthritis (RA) can increase the risk of CVD(62). In addition, adaptive immunity, primarily the Treg balance with Th1 and Th17 cells in various organs, has found recent fame as an important modulatory and downstream consequence of metabolic syndrome and an obese state. Targeting the adaptive immune system in CVD has been explored through tolerogenic vaccination aimed at inducing neutralizing antibodies against proteins associated with CVD risk such as epitopes found on oxLDL, ApoB, or inflamed vasculature and conversely, depletion of atherogenic B cell subsets (59, 63-65).

Tolerogenic vaccines work not to lower lipids, but instead to restore immune tolerance by inducing/mobilizing suppressive Tregs, $CD8^+$ effector/memory T cells, or protective B cells. Many of these vaccines aim to vaccinate against an atherogenic epitope derived from the lipoprotein protein core of LDL, ApoB(66). Immunization against ApoB peptides, such as p210, has seen mild success in murine models of atherosclerosis by offering athero-protection mediated by Tregs or effector $CD8^+$ T cells(67). These vaccines may be limited in translation

due to population prevalence of MHC alleles that may influence responses to vaccination(68). It is unknown if ApoB vaccinations are effective in established atherosclerosis, as most studies are prophylactic.

Vaccination induces plasma cells to secrete IgG antibodies against an adjuvant that opsonize or neutralize the peptide the vaccination was against. B cells, specifically B2 cells, need to be activated by T follicular helper cells to differentiate into plasma cells that secrete IgG antibodies. Few B cells are found in atherosclerotic plaque, but B cells in the spleen respond to a high cholesterol diet, suggesting local and systemic responses during atherosclerosis progression(69). Adaptive B cell responses are thought to be pro-atherogenic, while innate (low affinity IgM producing B1 cells) are thought to be anti-atherogenic. B cell depletion significantly improves the burden of several inflammatory diseases(63). Antibodies for B cell depletion targeting CD19, CD22, or B-cell maturation are approved or currently in clinical development for multiple sclerosis (MS) and cancer. Depending on the stage of atherosclerosis, macrophage uptake of oxLDL is atherogenic(70). This lead to the hypothesis that immunoglobulins targeting peptide epitopes in oxLDL would be atheroprotective partly due to antibody responses, which has been shown to be true in recent vaccine advances stimulating stronger antibody responses than predecessors(65). However, depletion of B cells using a monoclonal antibody against CD20 also has been shown to reduce atherosclerosis in mice underlying the complex nature of B cell contributions to atherogenesis (70). B cells are a heterogeneous population with both pro and anti-atherogenic effects likely dependent on disease stage. Taken together, this suggests that further research, including single cell sequencing of human B cell populations, may be required to define the phases of B cell depletion utility in atherosclerosis. Furthermore, because of the potential importance of atherosclerosis stage in B cell depletion therapies for atherosclerosis, this technology may be translationally limited by convoluted dosing schedules.

Tregs are regulators of the immune system with both anti-inflammatory and regenerative

functions(71, 72). Th17 cells, a type of T effector cell characterized by their secretion of pro-inflammatory IL-17, play an important role in protecting from infection and a pathogenic role in inflammatory metabolic diseases. Treg/Th17 balance thus thought to be a risk factor for atherosclerosis as well since metabolic disease is a common morbidity. Take together, Treg/Th17 balance implicates peripheral inflammation in progression of atherosclerosis, but it is unclear how important this role is. Expanded Tregs has been shown to be athero-protective in preclinical models of disease, especially circulating Tregs that can suppress proinflammatory T effector cells. At high doses IL-2 stimulates T effector cells. At low doses, Tregs act as an IL-2 sink keeping the cytokine away from T effector cells. However, IL-2 is also an essential cytokine for the growth and survival of Tregs, whose role in the control of inflammation has long been accepted (73). Low dose IL-2 is seen in multiple Phase I-II trials due to its promotion of regulatory T cell numbers(74). It is likely that peripheral inflammation due to a high fat diet plays a role in the nascent stages of atherosclerosis and thus would need to be prophylactically manipulated to protect against disease pathogenesis.

1.3 Introduction to Butyrate

1.3.1 The Microbiome and CVD.

Bidirectional interaction between the gut microbiota and the innate and adaptive immune system is important for inhibiting inflammation(75, 76). The gut microbiota does this mainly through many metabolic products produced during bacterial metabolism of complex carbohydrates. Bacteria's interactions with both the adaptive and innate immune systems contribute to the development of atherosclerosis (77, 78). High fat diet feeding, or the western diet, causes gut dysbiosis, which is negative alterations in the composition of the microbiome through reduction of diversity of bacterial species, number of bacterial species, or eradication of beneficial bacterial species (79). High-fiber diets lead to increased production of short-

chain fatty acids (SCFAs), microbiome diversity, and atheroprotection(76). Dysbiosis causes immune responses resulting in the production of inflammatory cytokines, oxidative stress, and insulin resistance(80, 81). Chronic dysbiosis and dysregulation of the mucosal barrier separating the intestine and bacteria can increase risk of cardiovascular disease, sepsis, and other inflammatory conditions(82). Short chain fatty acids, mainly butyrate, acetate, and propionate, are well known products of the microbiota that have tissue- and cell type-dependent pleiotropic functions(72, 83, 84).

Partially due to its role in regulating inflammation, the gut-heart axis has been repeatedly implicated in CVD(75). Butyrate, an anti-inflammatory SCFA and fermentation product of the gut microbiome, has received widespread attention for its immunomodulatory applications in immunometabolic diseases such as obesity, atherosclerosis, and nonalcoholic fatty liver disease (NAFLD)(54, 85).

1.3.2 Butyrate

Butyrate's Effects on Atherosclerosis in Preclinical Literature.

Butyrate, an anti-inflammatory SCFA and fermentation product of the gut microbiome, is synthesized in the gut and performs most of its functions there(86, 87). Most butyrate producers are gram-positive and come under Clostridium clusters IV and XIVa of the phylum Firmicutes(88). Butyrate is the primary energy source for colonocytes in the gut through beta-oxidation, and thus, is taken up quickly in these cells by SLC5A8 and SLC16A1. Butyrate is important in maintaining the tight junctions of the gut epithelium and regulating the immune phenotype of the barrier, providing an anti-inflammatory function indirectly by preventing the translocation of inflammatory molecules such as LPS. Orally administered sodium butyrate has also been shown to restore the microbiome diversity depleted by high-fat diet feeding(89). Butyrate transporters in the distal intestine (Apical: MCT1, SMCT1 and Basolateral: MCT3-5) have reportedly resulted in circulating concentration of 1-10 μM

butyrate(90). Increased oxygen consumption by these cells maintains the anaerobic environment in the colon, preventing expansion of potentially harmful bacteria and molecules(91). Butyrate that escapes metabolism by colonocytes (about 5% of all butyrate produced in the gut) can enter circulation and act on multiple cell types and organs or be used as energy in the TCA cycle. Butyrate's receptors are widespread past the gut, including liver, heart, and adipose tissue(92).

Butyrate can exert pleiotropic effects on various cell types first, through its action as an HDAC inhibitor, and secondly, through signaling through GPR's(including GPR43, GPR41, and GPR109a). GPR41, 43, and 109A are present on colonic epithelial cells, adipocytes, and immune cells(93). Butyrate-producing bacteria abundance, down-regulation of genes involved in butyrate synthesis, and low butyrate levels are all associated with vulnerability to CVD development. Butyrate, delivered through oral gavage, dramatically reduced atherosclerotic lesions, and reversed deteriorated routine parameters of atherosclerosis like LDL-C and total cholesterol in an ApoE$^{-/-}$ model of atherosclerosis(45). Butyrate is atheroprotective through regulating the expression of genes related to lipid and glucose metabolism, improving gut microbiota diversity, and suppressing a wide range of inflammatory and oxidative processes(94). Butyrate exerts anti-inflammatory effects in immune cells through inhibition of histone deacetylases (HDACs), resulting in suppression of NFB activation and reduced pro-inflammatory cytokine secretion. In macrophages, butyrate signaling suppressed HDACs resulting in suppression of IL-12 and IL-6 inflammatory cytokines and induced AMPK. Ma et al. (2023) found that butyrate suppressed atherosclerotic inflammation by regulating macrophage polarization via GPR43/HDAC-miRNA axis in ApoE$^{-/-}$ mice(45). The wide range of possible mechanisms through which butyrate positively affects inflammation and metabolism make it a difficult therapeutic to improve upon, as targeting could allegedly be to many disparate organs and cell types.

Inhibition of HDAC is also one of the mechanisms by which butyrate reduces plasma

lipids, a key contributor to atherosclerosis development in addition to other chronic metabolic diseases. Butyrate reportedly modifies cholesterol packaging such that circulating HDL-C is increased. HDAC inhibition via butyrate and other HDAC inhibitors in liver cells down-regulates the LDL receptor and upregulates ATP-binding cassette transporter sub-family A member 1 (ABCA1), and (scavenger receptor class B type 1) SRB1(11). Du et al. reported that butyrate supplementation up-regulated hepatic reverse cholesterol transport proteins such as ATP-binding cassette sub-family A member 1 (ABCA1) and mediating cholesterol efflux in macrophages(11). This could be the possible mechanism by which butyrate reportedly prevents hepatic steatosis in HFD fed mice.

1.3.3 Butyrate's Effects on Liver Injury and Nonalcoholic Fatty Liver Disease in Preclinical Literature

Nonalcoholic fatty liver disease (NAFLD) is a clinical diagnosis of steatosis in the liver. Steatosis in the liver is an adaptive manifestation of high-fat diet. NAFLD, and its characteristic steatosis, only become pathogenic when coupled with inflammation and fibrosis, which is then diagnosed as nonalcoholic steatohepatitis (NASH). Simple steatosis can become NASH via a variety of mechanisms. Multiple signaling pathways related to inflammation can be stimulated at the same time resulting in pathogenesis. The liver can become vulnerable to a shift from simple steatosis to pathogenic NASH due to multiple stressors, non-exhaustively including: increased lipid import, enhanced de novo lipogenesis (DNL) or impaired beta oxidation. Once there is an opportunity for the hepatocyte to be overwhelmed, inflammatory instigating events such as gut-derived inflammation leading to TLR signaling or ER stress can initiate disease.

Hepatic DNL has shown to be an important regulator of hepatic steatosis content because hepatic lipids are not derived from dietary fat or plasma FFA but instead have been shown to be more frequently derived from DNL. Hepatic de novo lipogenesis (DNL) is in-

creased in individuals with NAFLD, and in hepatocytes stimulated with glucose or insulin. Increased hepatic DNL results in uptake of sugars from portal circulation and conversion to triglycerides for storage in the liver or packaging. This process depends on acetyl-Coa carboxylase (ACC) and FA synthase (FAS), encoded by acaca and fasn respectively. Weight loss decreased steatosis in part by decreasing hepatic DNL. Thus, in the fasted state, DNL is at its lowest. Inhibiting lipogenesis has been shown to reduce hepatic insulin resistance and reverse NAFLD. Although the mechanisms for increased DNL in NAFLD are not fully elucidated, it is the leading hypothesis that because insulin and glucose activate sterol regulatory element–binding protein 1c (SREBP-1c) and carbohydrate response element–binding protein (ChREBP) respectively, which transcriptionally activate genes involved in DNL, there are differential effects of insulin action on the liver versus whole body insulin resistance(95). It is thought that insulin resistance manifests in the liver via suppression of hepatic glucose production, or gluconeogenesis, but that insulin sensitivity it preserved in the SREBP-1c pathway that stimulates fatty acid synthesis(16).

There are multiple reports of butyrate's prophylactic benefit in NASH and NAFLD models of disease. Many of them propose differing mechanisms of butyrate's action. One example focuses on butyrate's downregulation of DNL. For example, in a murine model of high-fat diet feeding, and sodium butyrate intervention sodium butyrate was sufficient to enhance the interaction between insulin-induced gene (Insig) activity and its upstream kinase AMP-activated protein kinase (AMPK), leading to inhibition of lipogenic genes (96). Furthermore, AMPK activation is known to reduce hepatic steatosis by decreasing DNL and increasing oxidative phosphorylation. Another proposed mechanism proposes butyrate's effects are mediated through increasing the health of the microbiome and the intestinal lining. Endo et al found that a butyrate producing probiotic reduced hepatic lipid deposition and significantly improved the triglyceride content, insulin resistance, serum endotoxin levels, hepatic inflammatory indexes, and increased phosphorylation of AMPK in a rat model of choline-

deficient/L-amino acid-defined (CDAA)-diet-induced NAFLD(97). This model is thought to induce NAFLD progression through increased circulating endotoxin resulting from weakened intestinal barrier.

1.3.4 Limitations to the Translation of Butyrate

Despite this potential, pharmacological aspects of butyrate, whether administered orally or generated by fermentation in the gut, present substantial limitations. Butyrate's translational potential is limited by low absorption into circulation, foul odor and taste, and lack of specific targeting. Oral administration of exogenous butyrate is limited by its fast metabolism in the gut resulting in low absorption into circulation (3-10 μM in plasma), its foul odor and taste, and its large doses required. Previous publications on sodium butyrate have been limited in dose to less than 20 milligrams per day and administer through gavage, which can be stressful on animals and thus lead to unreliable results for outcomes like weight and energy intake due to throat trauma. The high concentrations of systemic, circulating butyrate required for its anti-inflammatory activity (e.g., HDAC inhibition) are not found at physiological levels due to its consumption by colonocytes. In addition, ourselves and others have shown sodium butyrate to be cytotoxic in vitro to RAW macrophages and BMDCs (Bone marrow derived dendritic cells). There is a need for innovation that allows for higher doses of butyrate that are not cytotoxic to target immune cells and higher absorption of butyrate into circulation and peripheral tissues involved in metabolic disease and CVD. In addition, improved odor and taste are necessary for greater translatable potential of butyrate.

CHAPTER 2

A PRO-METABOLITE STRATEGY INHIBITS CARDIOMETABOLIC DISEASE IN AN APOE$^{-/-}$ MURINE MODEL OF ATHEROSCLEROSIS.

2.1 SerBut

We have previously engineered a small molecule pro-metabolite comprising of butyrate esterified to L-serine, O-butyryl-l-serine (SerBut), to address the challenges of butyrate translation. We hypothesize that amino acid transporters in the small intestine allow SerBut to exit the lumen in the small bowel and thus bypass metabolism in the large bowel, increasing systemic bioavailability. Moreover, SerBut should cross the plasma membrane via amino acid transporters to gain better access to HDACs for inhibition. This esterification favorably masks the odor and taste, increases half-life, and maintains the pleiotropic benefits of native butyrate upon hydrolysis.

Our group has shown that once- to twice-daily oral gavage of SerBut suppresses disease progression in murine models of autoimmune disease such as rheumatoid arthritis and multiple sclerosis(1). Here, we aimed to investigate the efficacy of SerBut dosed through drinking water in a murine apolipoprotein E knockout ($ApoE^{-/-}$) model of atherosclerosis, examining effects on vascular inflammation, plaque formation and composition, systemic metabolic regulation, and HFD-induced liver injury. We show that this systemically bioavailable form of butyrate reduces plaque in the aortic root via inhibition of progression, accumulation of immune cells in the aorta, and liver steatosis. Furthermore, plasma analysis shows SerBut reduces the fraction of LDL-C, systemic inflammatory cytokines, circulating neutrophils, and liver damage markers elevated by HFD-feeding. Under these experimental conditions, equidosed treatment with sodium butyrate (NaBut) failed to produce these favorable effects on cardiovascular or hepatic(immuno)pathology.

2.1.1 SerBut Absorption

Previously, it has been shown that SerBut is capable of intracellular transport by $ATB^{+,0}$(SLC6A14), a broad substrate-specific transporter expressed in the distal gut (ileum & colon) that recognizes neutral and cationic amino acids, as well as modified amino acids (ex. Additional

OH- group)(2). Amino acid transport in the large intestine is more relevant for bacterial metabolites and fluid secretion and would not result in high levels of circulating butyrate because they intracellularly transport amino acids. A patent by Ganapathy et al. focuses on SLC6A14 as the main transporter of SerBut, implicating SerBut in appetite regulation by stimulation of enteroendocrine secretion(3).

We propose that there are multiple amino acid transporters that can facilitate the transport of SerBut, including small intestine amino acid receptors distributing protein to the body. Absorption by SerBut here would result in high levels of circulating butyrate. Furthermore, if SerBut was absorbed by butyrate transporters, then both NaBut and SerBut would result in high levels of circulating butyrate due to the equimolar dosing of butyrate. Thus, we have hypothesized that the SerBut is transported by small intestine amino acid transporters.

We have not made any claims on a single amino acid transporter because they are known to be very promiscuous. Knocking out a specific amino acid receptor would have widespread effects on the organism and likely still allow some transport of L-Serine by other amino acid transporters. For example, in SLC6A19-knockout mice when inverted intestinal sections were analyzed for transport activity, Na^+-dependent uptake of glutamine, leucine, histidine, and tryptophan was completely abolished, but significant nonspecific uptake was retained. The mechanism of this significant uptake is not understood(4). This reasoning also has precluded the use of inhibitors for this sort of experiment.

2.2 Results

2.2.1 SerBut is a cytocompatible and stable carrier of anti-inflammatory free butyrate.

Previously, our laboratory has shown that SerBut suppressed inflammatory marker expression in bone marrow derived dendritic cells (BMDCs)(1, 5). Importantly, we additionally observed that SerBut maintained attenuated HDAC inhibition activity in a macrophage-like cell line (RAW 264.7)(1). We hypothesized that SerBut could be dosed much higher than 0.2 mM, the previously administered dose, without inducing cytotoxicity. Thus, we evaluated the cytocompatibility of SerBut compared to NaBut in RAW 264.7 macrophages (Figure 1A, Extended Figure 1). While NaBut significantly reduced cell viability at 4 mM and above, SerBut exhibited no cytotoxicity even at a concentration of 12 mM. We hypothesized this reduction of cytotoxicity, and the previously noted attenuation of HDAC inhibition activity, was due to inactivation of the butyrate upon conjugation to serine. Using liquid chromatography with tandem mass spectrometry (LC-MS/MS), we determined that approximately 10% of the SerBut sample was free butyrate at the time of measurement (Figure. 1B). To investigate stability, we repeated the experiment with SerBut in FBS-supplemented complete media stored for 1 month at 37C (Figure. 1B). The relative concentration of free butyrate did not change, indicating that esterases in FBS did not hydrolyze SerBut overtime but some free butyrate was available in the solution.

Exogenous NaBut supplementation is known to exert anti-inflammatory effects through NFκB suppression in macrophages in vitro and in vivo(6-8). We next investigated whether SerBut maintained NaBut's anti-inflammatory effects in macrophage-like RAW 264.7 cells. 12 mM SerBut significantly suppressed LPS-induced NFκB activation comparable to 1.3 mM NaBut (Figure. 1C), aligning with our finding that 10% of the SerBut sample was free butyrate (Figure. 1B). NFκB activation regulates the inflammatory macrophage phenotype,

inducing pro-inflammatory cytokine secretion and reactive oxygen species production. Therefore, we next investigated expression of activation and inflammation markers downstream of NFκB inhibition. Interestingly, only 12 mM SerBut significantly reduced both induced nitric oxide synthase (iNOS) and CD80 expression after LPS stimulation (Figure. 1D,E). Furthermore, 12 mM SerBut suppressed NFκB-regulated production of pro-inflammatory cytokines that are known to orchestrate inflammatory immune cell activation and recruitment, IL-6, MCP-1, and GM-CSF, as effectively as 1.3 mM NaBut (Figure. 1F-J). The anti-inflammatory cytokine IL-10 was significantly increased by NaBut treatment, while SerBut treatment produced a trending increase compared to LPS-stimulated controls (Figure. 1J). The iNOS suppressing capacity of high doses of SerBut was maintained even during longer LPS stimulations (Extended Figure. 1C) and had beneficial effect on activation markers CD80 and CD86 compared to NaBut but not LPS alone (Extended Figure. 1A,B). However, this effect was not observed when butyrate was dosed post-LPS stimulation (Extended Figure. 1D-F).

2.2.2 Seryl modification of butyrate significantly enhances its bioavailability and therapeutic efficacy in atherosclerotic mice.

To determine the bioavailability of SerBut in cardiovascular organs of hyperlipidemic mice, we gavaged equimolar amounts of SerBut and NaBut to ApoE$^{-/-}$ mice on a HFD (42% calories from fat) to ensure comparable consumption of butyrate by all mice at the given timepoint. Three hours post-administration, we analyzed the biodistribution of free butyrate via LC-MS/MS. (Figure. 2A). SerBut dosing significantly increased free butyrate in the heart and aorta compared to both NaBut-treated and PBS-treated mice (Figure. 2B,C). Corroborating our previous work(1), we also observed significant increases in the liver, inguinal lymph nodes (ILN), kidney, spleen, lung, and plasma (Figure. 2D-H,J). We also saw trending increases of free butyrate in the mesenteric lymph nodes (MLN) of SerBut treated mice (Figure. 2I).

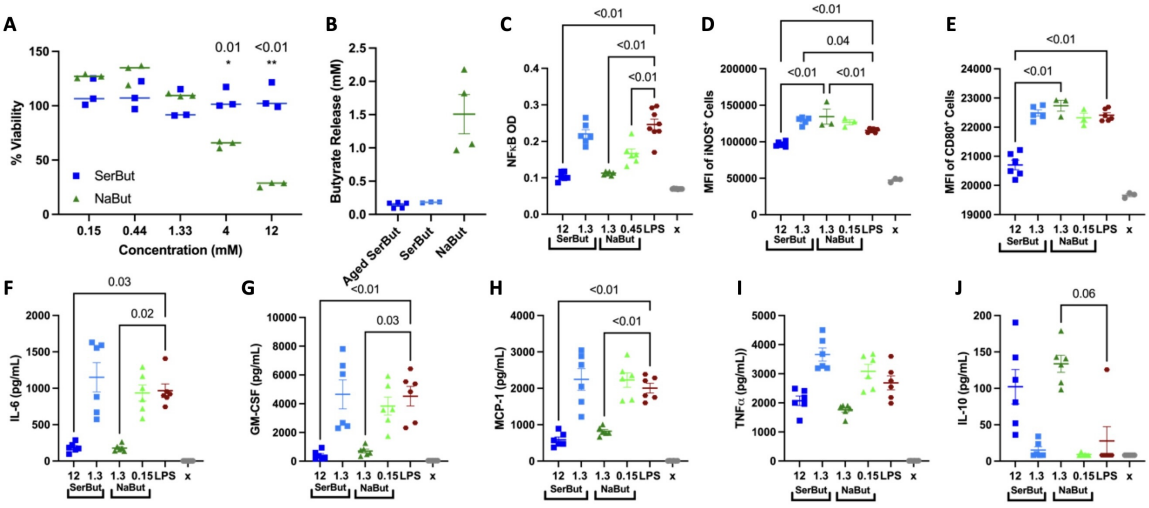

Figure 2.1: **SerBut reduces cytotoxicity and suppresses the inflammatory NFκB pathway in vitro. A.** Viability of RAW 264.7 cells treated with concentrations ranging from 0.15 mM to 12 mM SerBut or NaBut for 24 hr. The concentrations are: 0.15, 0.44, 1.33, 4, and 12 mM. **B.** LCMS/MS analysis of free butyrate in solution of aged SerBut (incubated at 37 °C in FBS-supplemented media for one month) and freshly dissolved SerBut and NaBut. **C.** NFκB activity of RAW Blue 264.7 reporter cells upon treatment with the indicated mM concentrations of SerBut or NaBut for 24 hr followed by 200 ng/mL LPS for 6 hr. **D-J.** RAW 264.7 cells treated for 24 hr with the indicated concentrations of SerBut or NaBut followed by 200 ng/mL LPS for 6 hr. **D-E.** Mean fluorescence intensity (MFI) of iNOS$^+$ or CD80$^+$ RAW 264.7 cells analyzed by flow cytometry. **F-J.** Cytokine concentrations in the cell culture supernatant of RAW 264.7 cells. "x" indicates untreated group. In Figure 1A, N=3 each group representing technical replicates. In Figure 1B, N=3 freshly made samples per two distinct experiments pooled for aged SerBut and NaBut groups, while fresh SerBut group represents a single experiment. One sample in the aged SerBut group and two samples in the NaBut group were lost due to filtering malfunctions or LCMS/MS autosampling malfunctions. In Figure 1C, n=6 technical replicates. Data represent mean $^+$ s.e.m. Experiments were performed two or more times with similar results. In Figure 1A, two-way ANOVA was performed. Statistical analyses were performed using a one-way ANOVA with a Dunnett's , Welch's (if standard deviations were significantly different by Bartlett and Brown-Forsyth tests), or Kruskal Wallis's (if data were not normally distributed determined by Shapiro-Wilk test) post-test in Figure 1C-J. P-values less than 0.10 are shown.

NaBut is limited in its translation by butyrate's rapid consumption by colonocytes as a primary energy source in the distal gut. We propose that the enhanced biodistribution of free, active butyrate (following cleavage from serine) in SerBut-treated mice is due to small intestine escape from the gut via amino acid transporters. To probe this hypothesis, we repeated the experiment and analyzed the biodistribution of free active butyrate in distinct sections of the intestinal tissue and the intestinal contents (Figure. 2K,L, Extended Figure. 2). Because neither ApoE$^{-/-}$ nor HFD feeding would be expected to change amino acid receptor expression or function in the intestine, this was performed in C57BL/6 mice on a normal diet. There were no significant changes in free butyrate in the intestinal contents for SerBut-treated mice (Extended Figure. 2). Conversely, in the upper and lower small intestine and ileum tissue(9), we observed significantly more free, active butyrate in SerBut-treated mice compared to both PBS- and NaBut-treated mice, indicating enhanced SerBut transport out of the gut in the small intestine (Figure. 2M-O). We saw no increase in butyrate in the colon tissue (Figure. 2P).

To investigate SerBut's effect on cardiovascular disease, ApoE$^{-/-}$ mice were given 150 mM SerBut or NaBut dissolved in water ad libitum over 6 weeks in concert with a HFD (Figure. 3A). This study furthermore allowed us to investigate a more translatable method of administration by adding SerBut to the drinking water, in contrast to administering by oral gavage. Treatment with serine showed no significant differences from controls in murine models of auto-immune disease(1) and thus was not included in this study. After 6 weeks, we observed significantly less Oil Red O-stained plaque area in the aortic root of SerBut-treated mice compared to both control and NaBut-treated groups (Figure. 3B,E). We then asked if plaque complexity and stage were changed between treatment groups, potentially indicating suppression of disease progression. Utilizing Stary histological grading(10) and quantification of plaque components, we found a significant reduction of plaque severity score, CD68^{+} stained area, and necrotic core area in SerBut-treated mice compared to water-treated mice (Figure.

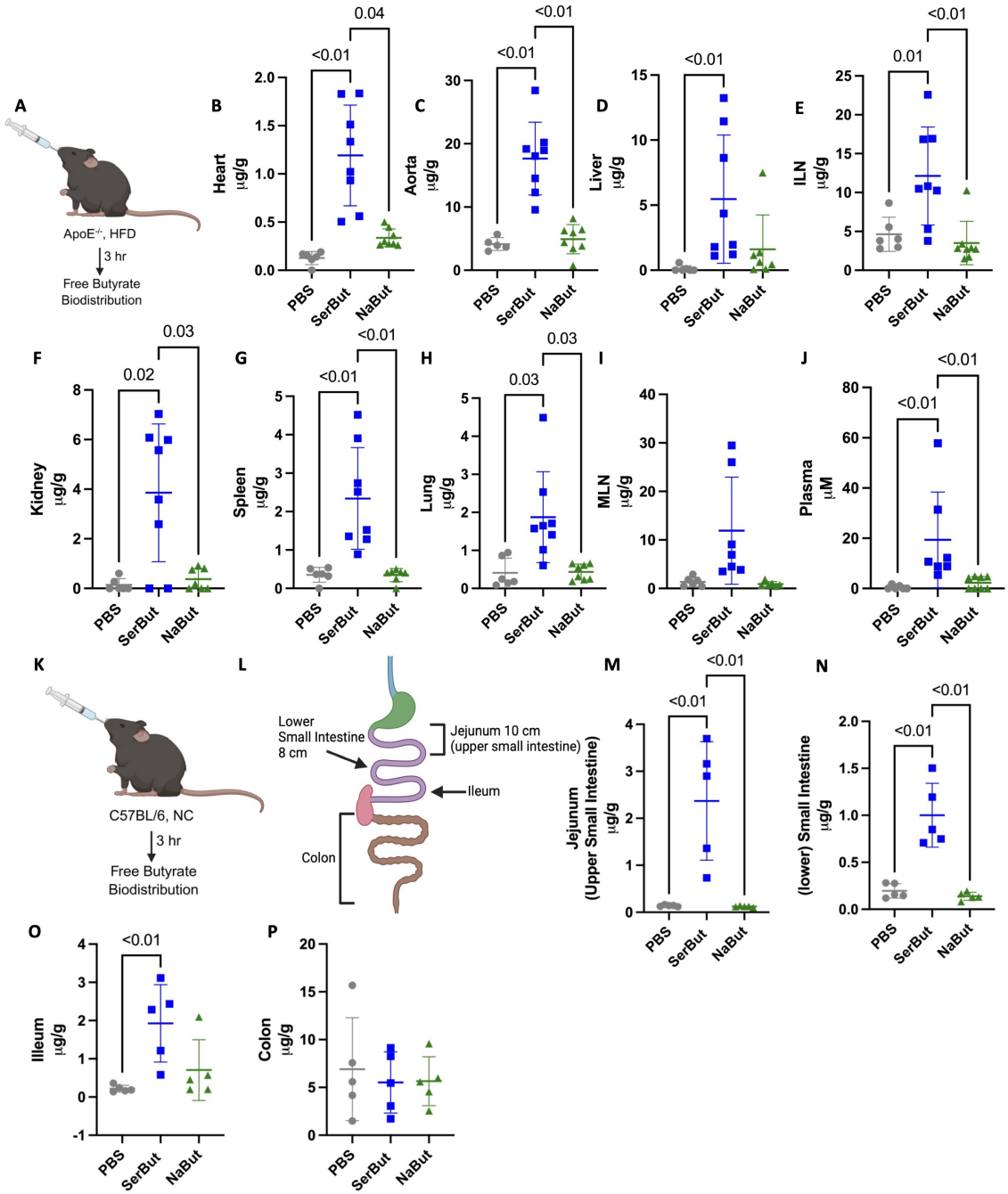

Figure 2.2: **Seryl modification increases oral bioavailability of butyrate in atherosclerotic organs. A.** Experimental schema of ApoE$^{-/-}$ mice fed a HFD for 8 weeks, after which they received a single equimolar gavage of 272 µM butyrate as SerBut or NaBut. After 3 hr, mice were perfused, and the amount of butyrate was measured in the **B.** heart, **C.** aorta, **D.** liver, **E.** inguinal lymph nodes (ILN), **F.** kidney, **G.** spleen, **H.** lung, **I.** mesenteric lymph nodes (MLN), and **J.** plasma (µM). N=8 mice in SerBut and NaBut groups.

(Continued)**K.** Experimental schema of C57BL/6 mice on a NC diet who received a single equimolar gavage of 272 µM Butyrate as SerBut or NaBut.**L.** Diagram of gut dissection. **M.** Duodenum and Jejunum (upper small intestine) **N.** lower small intestine **O.** Ileum **P.** colon. Free butyrate (µg) was normalized to tissue weight (g). Data points represent individual mice displayed with median $^{+}$ s.e.m. Statistical analyses were performed using a one-way ANOVA with a Dunnett's, Welch's (if standard deviations were significantly different by Bartlett and Brown-Forsyth tests), or Kruskal Wallis's (if data were not normally distributed determined by Shapiro-Wilk test) post-test. P-values less than 0.10 are shown.

3F-H, Extended Figure 3A-D) and trended lower compared to NaBut-treated mice. We then investigated the plaque immune phenotype by immunofluorescence staining of CD68, iNOS, and DAPI. Although the total numbers of $CD68^{+}$ macrophages were reduced compared to NaBut-treated groups, the macrophages per unit area was not (Extended Figure. 3F). However, both $CD68^{+}$ cells and $iNOS^{+}$ cells per unit area atherosclerotic lesion were increased in NaBut-treated groups, indicating a more inflamed plaque phenotype in NaBut treated groups compared to both water and SerBut-treated groups (Figure. 3I-L).

Since immune cell infiltration into the aorta has been shown to accelerate disease pathogenesis, we next asked if SerBut reduced vascular inflammation(11). Through flow cytometry of the aorta, we found that only SerBut significantly reduced $CD45^{+}$ total leukocytes, $CD11b^{+}$ monocytes, and $CCR2^{+}CD11b^{+}$ monocytes in the aorta compared to control groups, while NaBut did not (Figure. 3M-O). $CD11c^{+}MHCII^{hi}$ dendritic cells, $CD11b^{+}F480^{+}$ macrophages, and $CD19^{+}$ B cells were significantly reduced by both NaBut and SerBut compared to water controls (Extended Figure. 4). Additionally, $CD11b^{+}Ly6C^{hi}$ monocytes and $CD4^{+}$ T cells were significantly reduced only in SerBut-treated mice compared to water-treated controls (Extended Figure. 4).

We next evaluated the effect of SerBut on systemic markers of inflammation. SerBut reduced the inflammatory cytokines IL-6 and IFN in plasma significantly compared to control groups, while NaBut treatment did not (Figure 3 M,N). Both NaBut and SerBut showed a trend toward reduction of plasma IL-1 (Extended Figure. 4). SerBut significantly reduced the frequency of circulating $Ly6G^{+}CD11b^{+}$ neutrophils compared to both NaBut and water-

treated controls (Figure. 3S). Additionally, SerBut expanded regulatory T cells (Treg) in the MLN but not the skin draining lymph nodes or spleen (Extended Figure. 5). However, in both the MLN and spleen SerBut reduced the Th17/Treg cell ratio, indicating a more tolerogenic phenotype. In the spleen, NaBut treated mice also showed a lower Th17/Treg cell ratio (Extended Figure. 5). In the MLN, but not the ILN, $CD11b^{+}F480^{+}$ macrophages exhibited significantly decreased inflammatory marker $iNOS^{+}$ compared to controls, but not NaBut treated mice (Extended Figure. 6). Importantly, all cages consumed comparable amounts of water (Figure. 3P), suggesting that the effect of SerBut is due to its immunological effects and not to the administration of a higher dose. Overall, SerBut exerted more efficacious anti-atherogenic and anti-inflammatory effects in vivo than NaBut systemically and at the site of disease compared to water-treated control groups.

Butyrate dosing has been shown to significantly affect the gut microbiome and its metabolic products(12, 13). Thus, we wanted to understand how the two types of exogenous butyrate (SerBut and NaBut) affected the microbiome, particularly the colonic microbiota. Based on our biodistribution data, we expected that SerBut is predominantly absorbed in the small bowel and transited to systemic circulation, thus avoiding the microbial communities found in the colon and their interaction with the host there. To understand the potential association between the microbiome and the anti-atherosclerotic effects of SerBut and NaBut, we performed sequential multiple linear regressions on 16S rRNA sequencing of the colonic contents after treatment on HFD for 6 weeks (Extended Figure. 7,8,9). We asked if pathology readouts were associated with butyrate treatment (combining SerBut and NaBut together), seryl modification of butyrate, or the relative abundance of individual bacterial genera to identify specific taxa implicated in disease pathology. We found that seryl modification of butyrate, i.e., SerBut treatment, could alone explain the reduction of plaque after controlling for most bacterial genuses. We asked if the bacterial genuses that were required to explain the reduction in the plaque were expanded by SerBut treatment, potentially indicating their

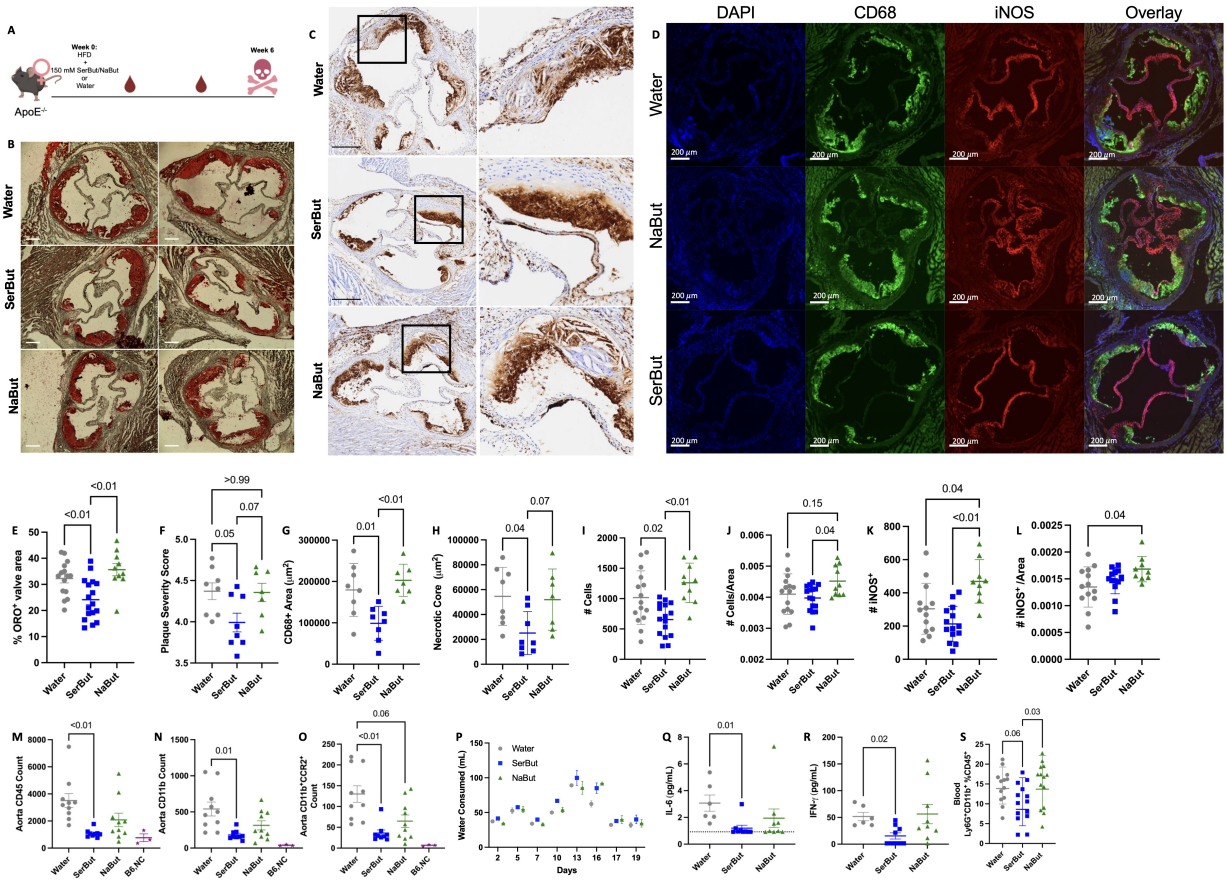

Figure 2.3: **SerBut suppresses the progression of atherosclerotic plaque, immune cells in the aorta, and systemic inflammation. A.** Experimental schema of female ApoE$^{-/-}$ mice on a HFD in concert with 150 mM SerBut, NaBut, or water ad libitum for 6 weeks. **B.** Oil-Red-O (ORO) staining of plaque in the aortic root taken at week 6 of HFD and treatment. Scale bar represents 200 μm. **C.** CD68^{+} IHC staining of plaque in the aortic root taken at week 6 of HFD and treatment. Scale bar represents 200 m. **D.** Representative images of immunofluorescence staining of aortic root taken at week 6 of HFD treatment. Scales at 200 m. **E.** Quantification of ORO^{+} valve area in aortic root. **F.** Histological STARY scoring of plaque severity. G. Quantified CD68^{+} area of CD68^{+} IHC staining. H. Quantified necrotic core of CD68^{+} IHC staining. **I.** Quantified DAPI positive cells in plaque of immunofluorescence-stained aortic root. **J.** DAPI positive cells per plaque area. **K.** Quantified iNOS^{+} cells in plaque of immunofluorescence-stained aortic root. **L.** iNOS^{+} cells per area of plaque. **M-O.** Flow cytometry of immune cells infiltrating the aorta after 6 weeks of HFD and treatment: **M.** CD45^{+} total leukocyte cells, **N.** CD11b^{+} monocytes, and **O.** CCR2^{+}CD11b^{+} monocytes. **P.** Water consumed by each cage of mice in mL for the first 19 days of the experiment. **Q-R.** Inflammatory cytokines in plasma:

(Continued) **Q.** IL-6, and **R** IFNy **S** Blood flow cytometry of $Ly6G^{+}CD11b^{+}$ circulating neutrophils. **T.** Blood flow cytometry of $F480^{+}CD11b^{+}$ circulating macrophages. Data represents mean water drank between two cages (replicates) calculated as weight change of bottle converted to mLs of water. Bars represent standard deviation. n=5/cage and n=10 mice per group. In Figure 3D-N, data points represent individual mice displayed with median $^{+}$ s.e.m. Statistical analyses were performed using a one-way ANOVA with a Dunnett's, Welch's (if standard deviations were significantly different by Bartlett and Brown-Forsyth tests), or Kruskal Wallis's (if data were not normally distributed determined by Shapiro-Wilk test) post-test in Figure 3D-H and Figure 3M-N. In Figure 3I-L, statistical analyses were performed using an unpaired Students t-test. Welch's t-test was used if standard deviations were significantly different. If data was not normally distributed, determined by Shapiro-Wilk normality test, a Mann-Whitney test was used. P values less than 0.10 are shown. Outliers were removed by ROUT testing at Q=1 in figures I-L. Scoring in Figure 3E was done blinded. Data in Figure 3C represents two independent pooled experiments where n=10 per group per experiment for water and SerBut treated groups and n=10 for NaBut treated groups in a single experiment.

mediation of SerBut's beneficial effects (Extended Figure. 7B-G) None of these bacteria were expanded by SerBut treatment, indicating that they likely do not mediate SerBut's beneficial effects on atherogenesis. The genus Lactobacillus was the only bacterial variable that alone could explain the reduction of plaque in the aortic root after controlling for the aforementioned variables (Extended Figure. 8).

By contrast, unmodified butyrate treatment could not explain the observed reduced disease pathology and required the abundance of multiple bacterial taxa (Extended Figure. 9) to explain correlations with disease pathology. We then asked if SerBut's efficacy can be explained by expanding the abundance of Lactobacillus and found that both water control and NaBut groups had significantly more Lactobacillus than SerBut groups (Extended Figure. 8B). Next, we asked if the treatment group significantly modulated the relationship of lactobacillus abundance with plaque (Extended Figure. 8C). SerBut treated groups showed no relationship between lactobacillus and plaque, while both NaBut and Water treated groups showed a negative correlation between lactobacillus and plaque. Together, these data demonstrate the differences between the microbiome effects of these two forms of exogenous butyrate, suggesting differing mechanisms of action. We hypothesize that the majority of

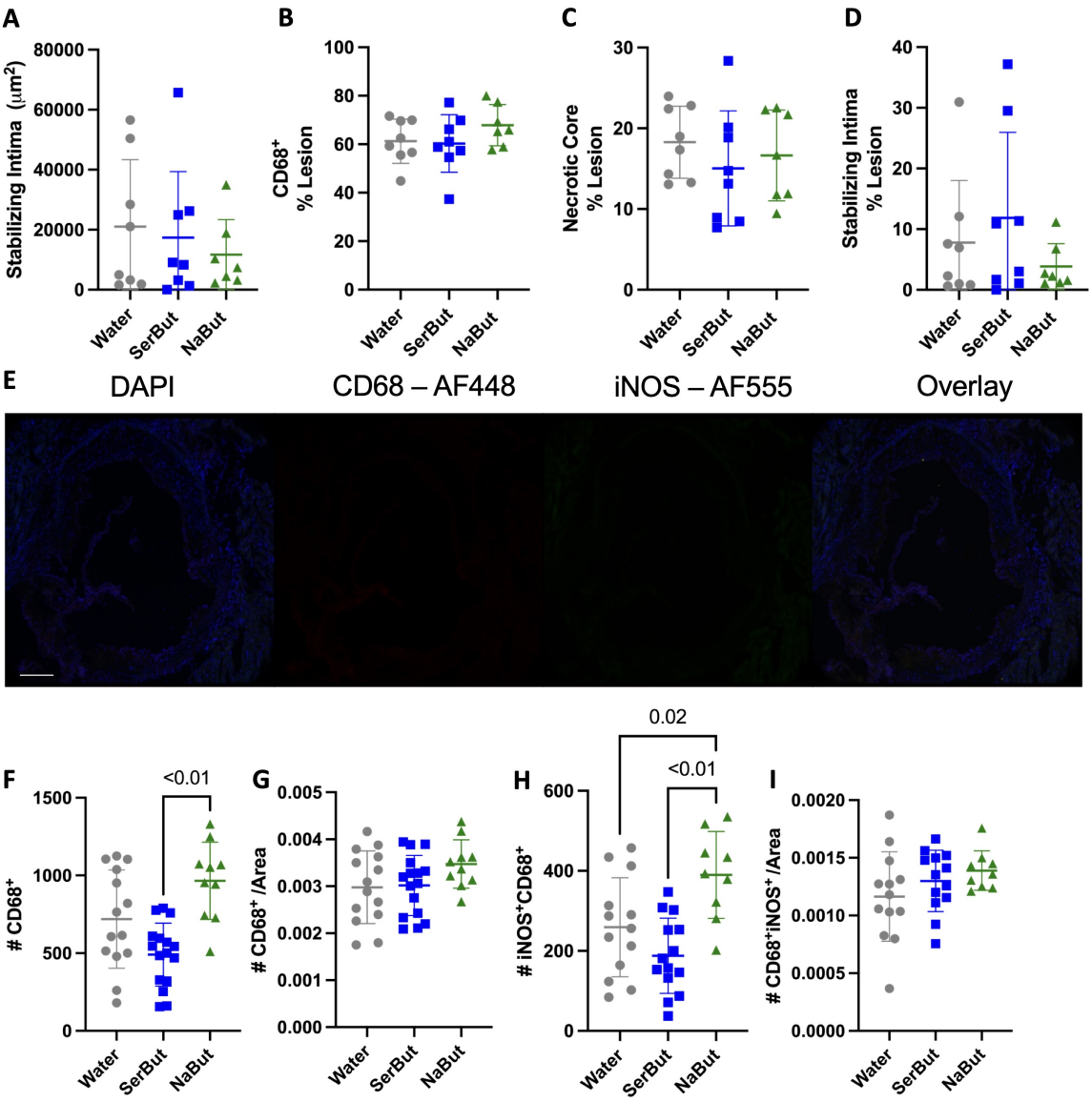

Figure 2.4: **Extended Figure 3. Immunofluorescence and CD68+ IHC analysis of macrophages in the aortic root.A-D** Analysis of CD68$^+$ Immunohistochemistry-stained aortic roots collected at 6 weeks of HFD and treatment. **A.** Quantified stabilizing intima of CD68$^+$ IHC stained plaque. Stabilizing intima describes intima that has layered over CD68$^+$ plaque. **B.** CD68$^+$ area normalized to total atherosclerotic lesion. **C.** Necrotic Core area normalized to total atherosclerotic lesion. **D.** Stabilizing Intima normalized to total atherosclerotic lesion. **E.** Immunofluorescence staining Isotype Controls (from left to right): DAPI Isotype control ranging from 101.9-4497, CD68 Isotype control ranging from 102.6-15648.4, iNOS Isotype control ranging from 72.6-28494 and Overlay. Positive cells were identified based on mean fluorescent intensity thresholding. **F.** Quantification of CD68+ macrophages, G. CD68$^+$ macrophages normalized to plaque area, **H.** iNOS$^+$ CD68$^+$ inflammatory macrophages, and

(Continued) **I.** iNOS^{+}CD68^{+} inflammatory macrophages normalized to plaque area. Statistical analyses were performed using a one-way ANOVA with a Dunnett's, Welch's (if standard deviations were significantly different by Bartlett and Brown-Forsyth tests), or Kruskal Wallis's (if data were not normally distributed determined by Shapiro-Wilk test) post-test.

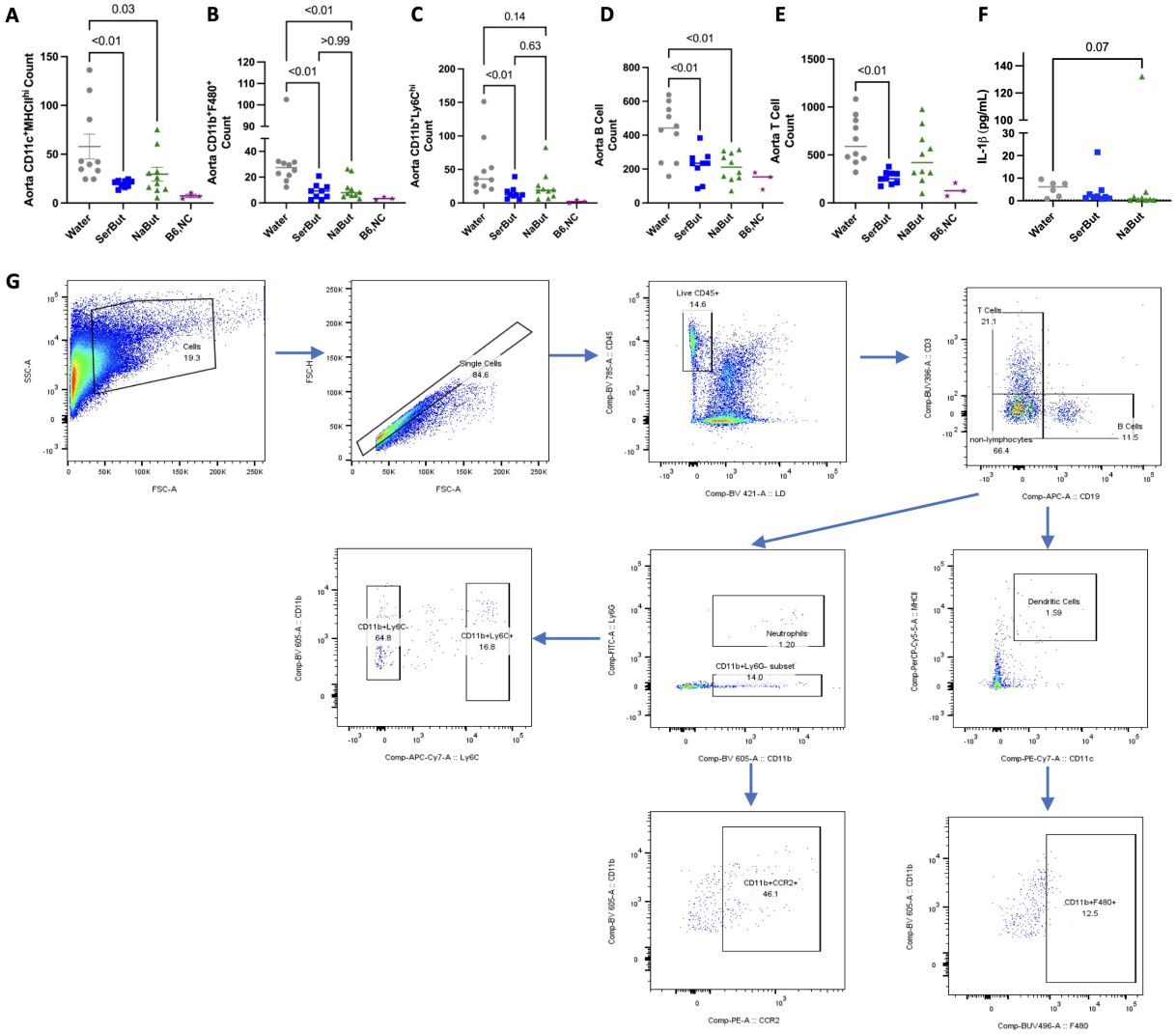

Figure 2.5: **Extended Figure 4. A-E.** Aorta flow cytometry: **A.** CD11c^{+}MHCII^{hi} dendritic cells, **B.** Macrophages, **C.** CD11b^{+} Ly6C^{hi} myeloid cells, **D.** CD19^{+} B cell count, and **E.** CD3^{+} T cell count. **F-H.** Blood flow cytometry: **F.** Neutrophils (Ly6G^{+}CD11b^{+}) % CD45^{+}, G. CD11b^{+} monocytes %CD45^{+}, H. CCR2^{+} %CD11b^{+} monocytes. **I.** Plasma IL-1β. **GJ.** Aorta flow cytometry Gating strategy.

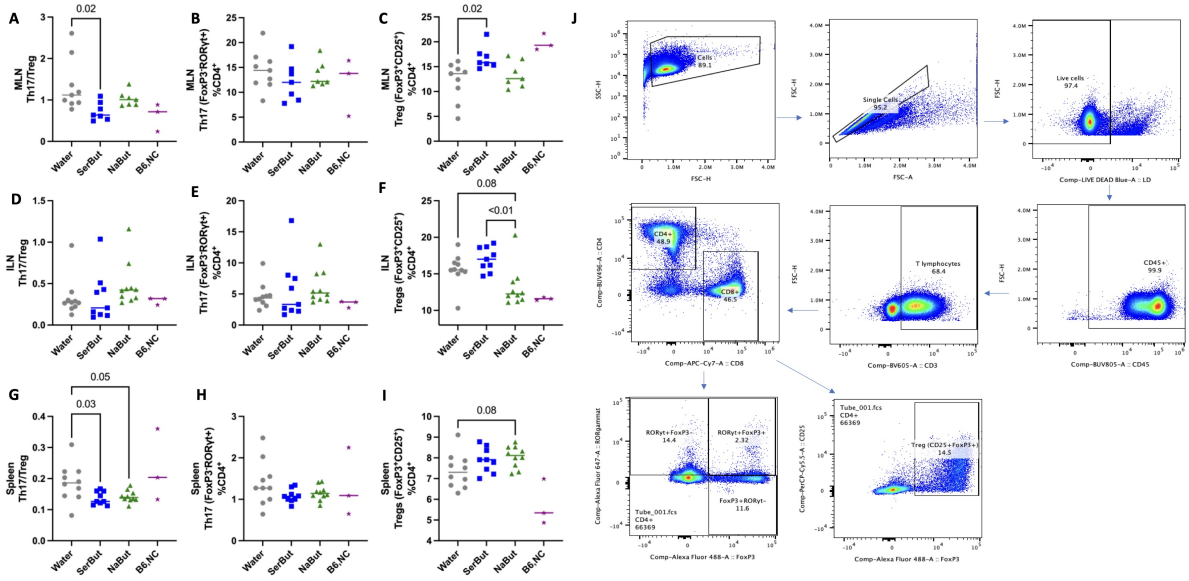

Figure 2.6: **A-C.** Mesenteric lymph node flow cytometry. **D-F** Inguinal Lymph node flow cytometry. **G-I.** Spleen flow cytometry. **J.** Gating strategy. Statistical analyses were performed using a one-way ANOVA with a Dunnett's, Welch's (if standard deviations were significantly different by Bartlett and Brown-Forsyth tests), or Kruskal Wallis's (if data were not normally distributed determined by Shapiro-Wilk test) post-test.

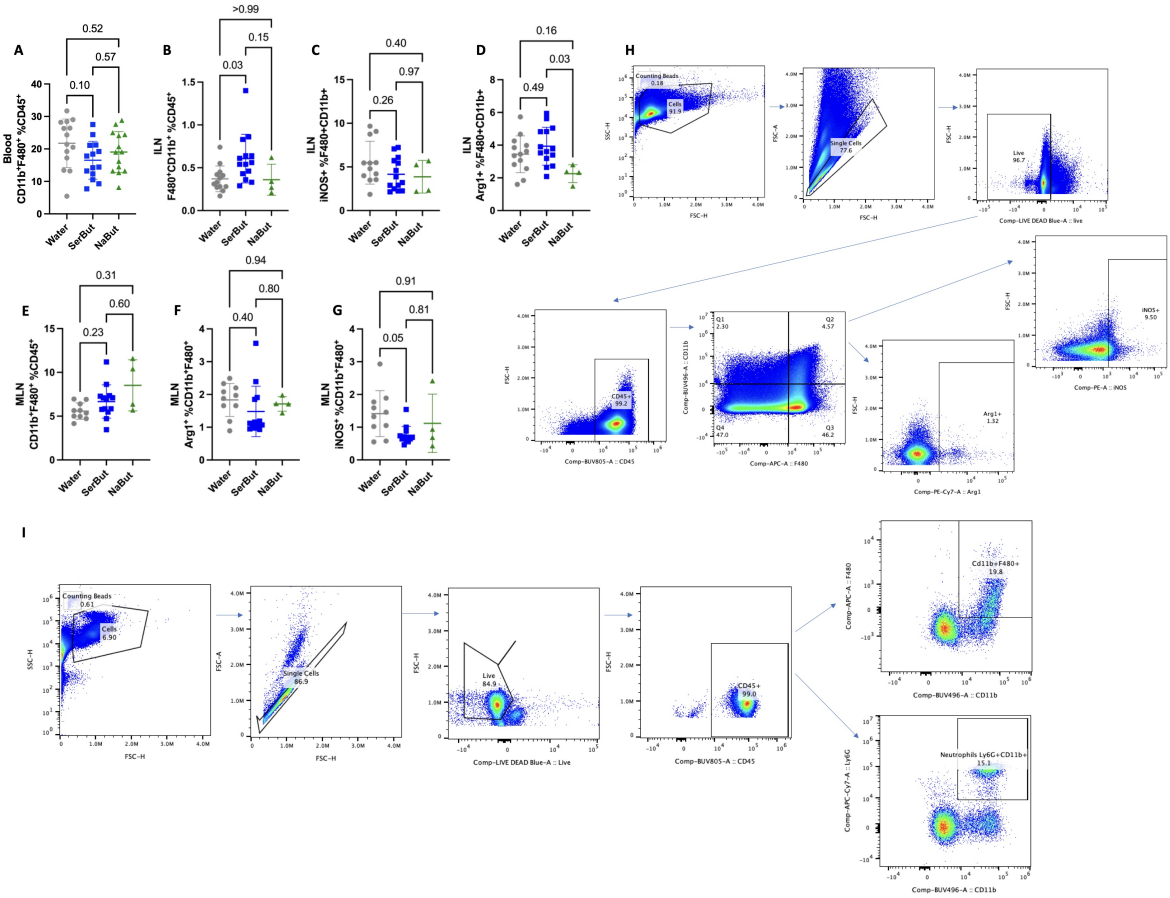

Figure 2.7: **Flow cytometry of Macrophage populations in the blood and lymph nodes. A.** Blood flow cytometry of $CD11b^{+}F480^{+}$ macrophages $\%CD45^{+}$. **B-D.** Inguinal lymph node flow cytometry. **B.** $CD11b^{+}F480^{+}$ macrophages $\%CD45^{+}$. **C.** $iNOS^{+}$ inflammatory macrophages. **D.** Anti-inflammatory $Arg1^{+}$ macrophages. **E-G.** mesenteric lymph node flow cytometry. **E.** $CD11b^{+}F480^{+}$ macrophages $\%CD45^{+}$. **F.** $iNOS^{+}$ inflammatory macrophages. **G.** Anti-inflammatory $Arg1^{+}$ macrophages. **H.** Lymph node flow gating strategy. **I.** Blood flow gating strategy. Statistical analyses were performed using a one-way ANOVA with a Dunnett's, Welch's (if standard deviations were significantly different by Bartlett and Brown-Forsyth tests), or Kruskal Wallis's (if data were not normally distributed determined by Shapiro-Wilk test) post-test.

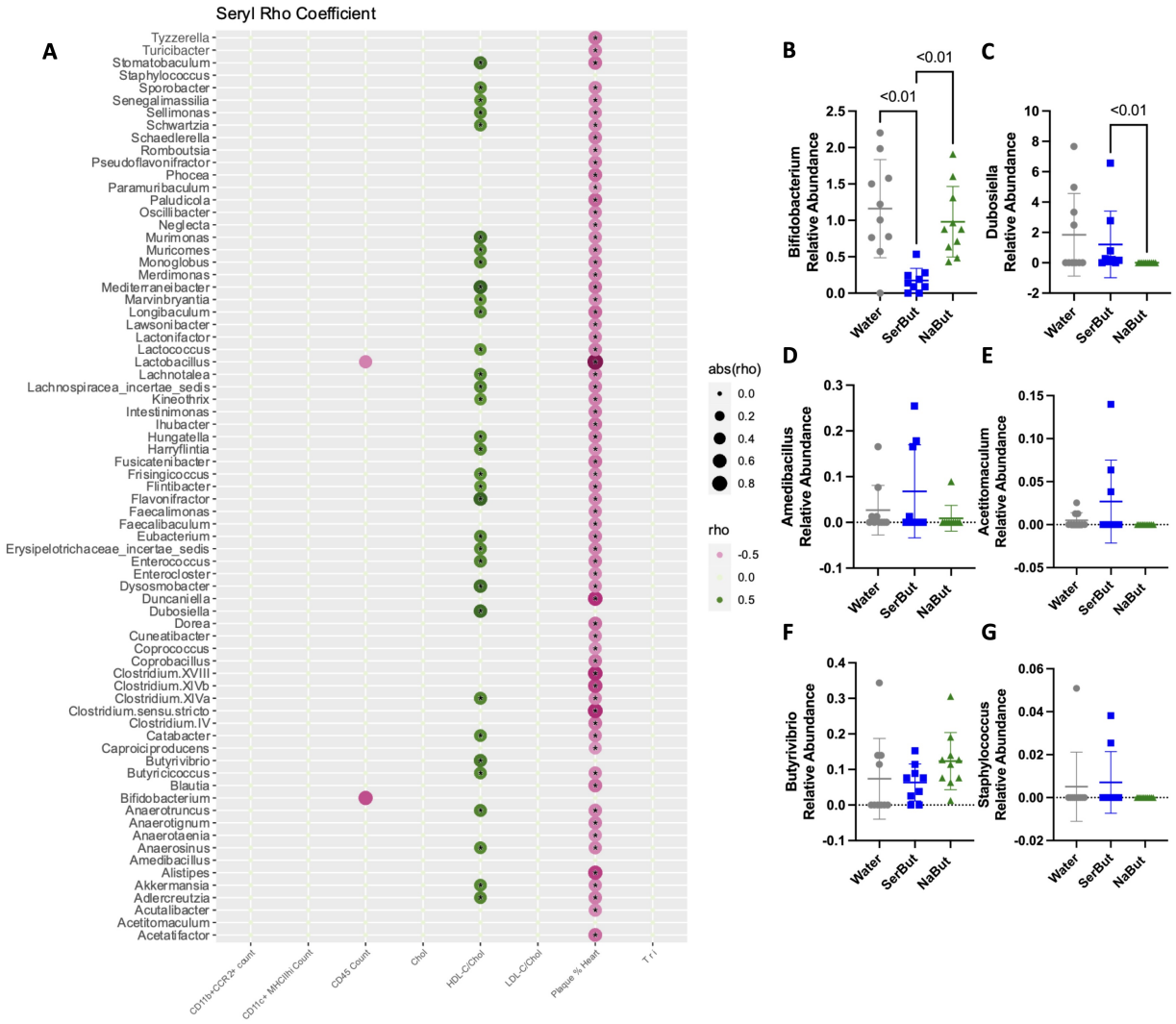

Figure 2.8: **Ecosystem-wide and genus-level large-bowel microbiome variation, SerBut, or general butyrate effects on plaque in the heart. A.** Multiple linear regression displaying all pathology readouts. Associations between plaque in the heart and Seryl modification of butyrate after partialing out the effect of butyrate and genus level relative abundance as covariates. **B-G.** Relative abundance of bacterial genus that returned rho of zero. **B.** Bifidobacterium **C.** Dubosiella **D.** Amedibacillus **E.** Acetitomaculum **F.** Butyrivibrio **G.** Staphylococcus. Positive correlations (between treatment/microbiome factor and pathology factor) are displayed in green as the rho correlation coefficient. Negative correlations are displayed in pink as the rho correlation coefficient. Color intensity is proportional to transformed rho coefficient. Astrix denote significance after multiple testing correction (FRD) on every row value in a specific column (pathologies) using an FDR of 0.05.

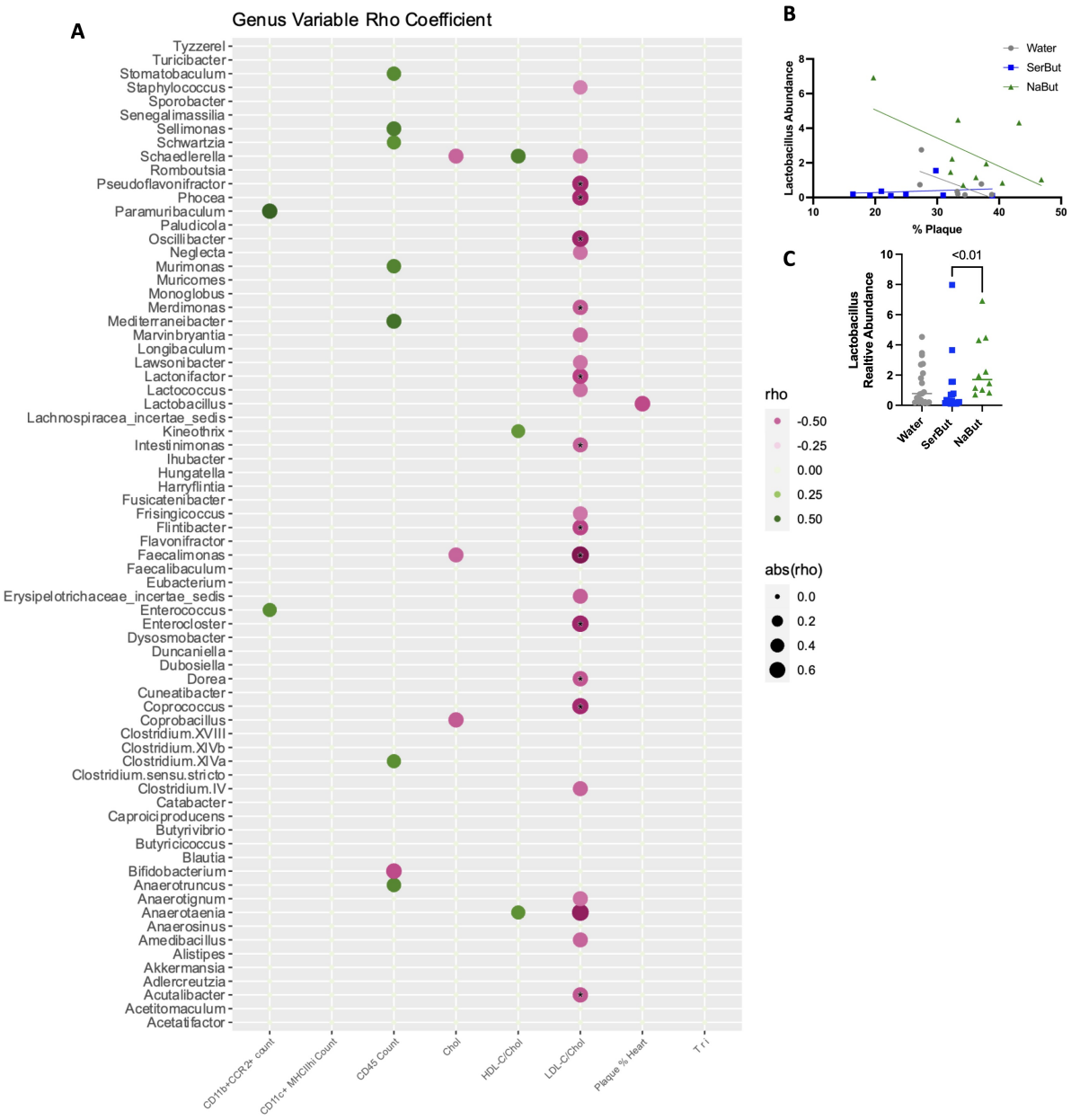

Figure 2.9: **Ecosystem-wide and genus-level large-bowel microbiome variation, SerBut, or general butyrate effects on plaque in the heart. A.** Multiple linear regression displaying all pathology readouts. Associations between plaque in the heart and Genus relative abundance after partialing out the effect of butyrate and seryl modification of butyrate as covariates. **B.** Correlation between Lactobacillus relative abundance and the percent plaque in the aortic root per group. **C.** The relative abundance of Lactobacillus. Positive correlations (between treatment/microbiome factor and pathology factor) are displayed in green as the rho correlation coefficient. Negative correlations are displayed in pink as the rho correlation coefficient. Color intensity is proportional to transformed rho coefficient. Astrix denote significance after multiple testing correction (FRD) on every row value in a specific column (pathologies) using an FDR of 0.05.

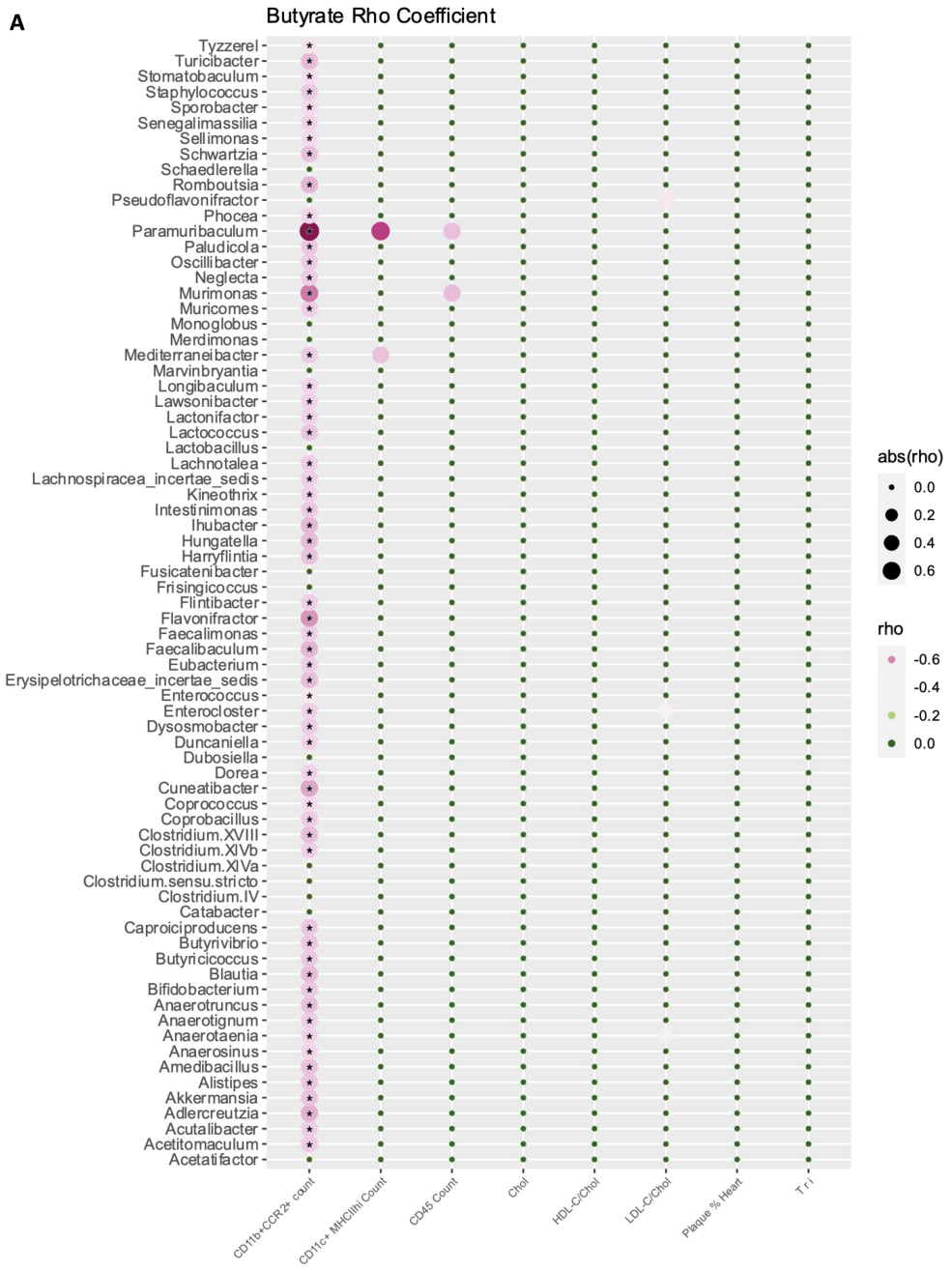

Figure 2.10: **Ecosystem-wide and genus-level large-bowel microbiome variation, SerBut, or general butyrate effects on plaque in the heart. A.** Multiple linear regression displaying all pathology readouts. Associations between plaque in the heart and any form of butyrate after partialing out the effect of genus relative abundance and seryl modification of butyrate as covariates. Positive correlations (between treatment/microbiome factor and pathology factor) are displayed in green as the rho correlation coefficient. Negative correlations are displayed in pink as the rho correlation coefficient. Color intensity is proportional to transformed rho coefficient. Astrix denote significance after multiple testing correction (FRD) on every row value in a specific column (pathologies) using an FDR of 0.05.

SerBut's effect on plaque formation and inflammation may not be mediated though modulation of relative abundance of bacterial genuses in the microbiome, although NaBut treatment may mediate some efficacy through bacterial expansion. Further sequencing may be able to provide species level characterization could identify single bacteria with differentially abundant growth or function due to treatment groups.

2.2.3 SerBut suppresses HFD-induced liver injury.

Since NaBut has been shown to reduce plasma lipids in murine models of atherosclerosis(14), we asked if SerBut was also able to influence plasma lipids. LDL-C as a fraction of total cholesterol was significantly reduced by both SerBut and NaBut treatment (Figure. 4A, Extended Figure. 10). Additionally, the ratio of high-density lipoprotein (HDL) to total cholesterol was significantly increased in SerBut treated mice compared to NaBut treatment (Figure. 4B, Extended Figure. 10). Neither SerBut nor NaBut influenced total cholesterol or triglycerides in the plasma (Figure. 4C,D). Interestingly, SerBut significantly reduced plasma alanine transaminase (ALT) and aspartate aminotransferase (AST) compared to both water control and NaBut groups (Figure. 4E,F), showing reduction of liver damage induced by HFD for SerBut but not NaBut treatment. NaBut-treated mice experienced a significant increase in lipase — a common marker of pancreatitis — in the plasma, while SerBut showed no effect (Figure. 4G), suggesting that SerBut may have an enhanced safety profile compared to NaBut. The positive effects of SerBut were independent of body weight, as SerBut-treated mice had similar weights to water controls throughout the study (Figure. 4H). Overall, seryl esterification significantly enhances the anti-atherosclerotic hepatoprotective activity and safety profile of butyrate.

It has previously been reported that butyrate can reduce fatty deposits, fibrosis, and inflammation in the liver(15, 16). Many CVD patients have liver disease due to metabolic dysregulation, increased innate immune cell activation, and unresolved inflammation due

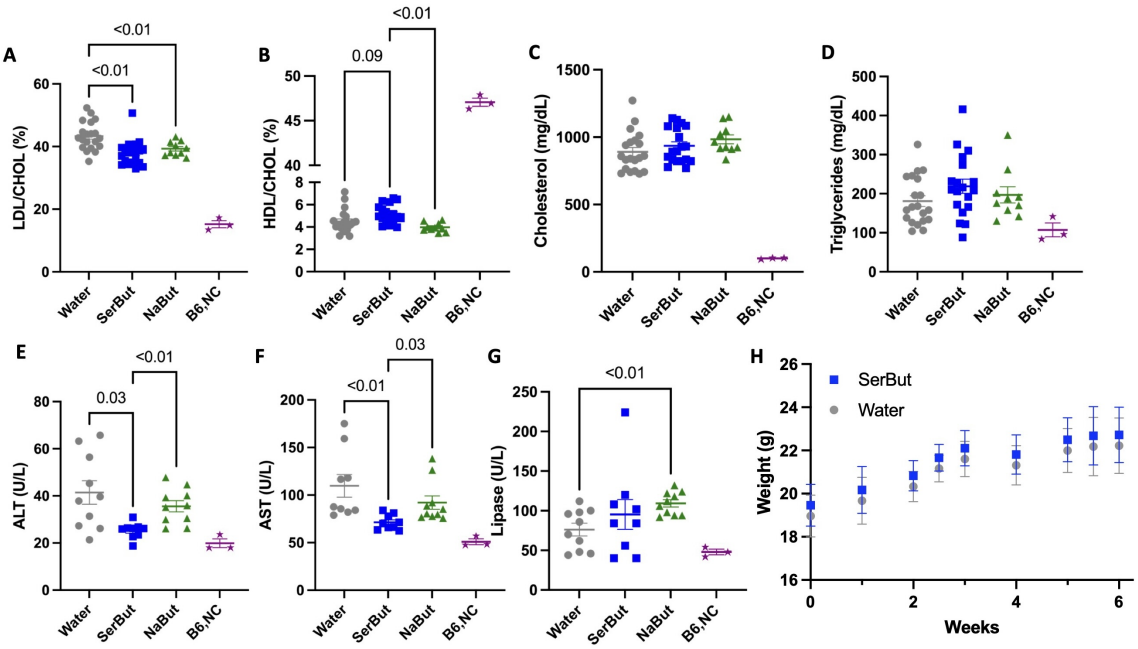

Figure 2.11: **SerBut suppresses liver toxicity, plasma LDL-C, and systemic inflammation.** Plasma taken at 6 weeks of treatment in the regimen described in Figure. 3A. **A-D.** Blood chemistry analysis pooled between two duplicate studies: **A.** % LDL/total cholesterol, **B.** % HDL/total cholesterol, **C.** Total cholesterol, and **D.** Triglycerides. **E-G.** Blood chemistry analysis: **E.** ALT (alanine transaminase), **F.** AST (aspartate aminotransferase), and **G.** Lipase. P-values less than 0.10 are shown. **H.** Average weight of mice in water and SerBut treated groups. "B6,NC" denotes three age matched C57BL/6 mice on a normal diet as a non-statistical comparison to visualize healthy examples. Data points represent individual mice displayed with median + s.e.m. Data in Figure 4A-D represents two independent pooled experiments, n=10 per group per experiment for water and SerBut treated groups. n=10 in a single experiment for NaBut treated group. Statistical analyses were performed using a one-way ANOVA with a Dunnett's, Welch's (if standard deviations were significantly different by Bartlett and Brown-Forsyth tests), or Kruskal Wallis's (if data were not normally distributed determined by Shapiro-Wilk test) post-test.

to sustained NFκB activation(17). Furthermore, many lipid-lowering drugs such as statins increase lipid uptake by the liver by increasing LDL-R expression, potentially inducing liver toxicity that prevents patients with liver disease from taking these medications(18). In the ApoE$^{-/-}$ atherosclerotic model, HFD feeding induces hepatic lipid accumulation and inflammation in addition to plaque accumulation in the aorta(19). Thus, motivated by our finding of significantly reduced plasma ALT and AST in SerBut-treated groups (Figure. 4E,F), we further investigated SerBut's potential beneficial effect on liver health under HFD feeding. Using a previously described liver histology scoring system, we investigated key features of nonalcoholic fatty liver disease (NAFLD) and liver injury in mice: steatosis (macrovesicular fat), nuclear hypertrophy, and lobular inflammation of the liver (CD3^{+} immune cells)(20). Steatosis was significantly suppressed by SerBut treatment, but not by treatment with NaBut (Figure. 5A). Neither SerBut nor NaBut significantly reduced CD3^{+} immune cell infiltration into the livers, indicating no change in lobular inflammation, which may be expected at such early timepoints in murine liver disease models (Figure. 5B). Hepatocellular nuclear hypertrophy was suppressed by both SerBut and NaBut treatment (Figure. 5C). Interestingly, both SerBut and NaBut treatment significantly suppressed LDL-R protein levels as shown by Western blot (Extended Figure. 10). This data suggests that the reduction of circulating LDL-C levels via NaBut and SerBut treatment is not due to increased uptake of lipids via increased LDL-R expression. Thus, the overall summed histological score indicated reduced liver pathology in the ApoE$^{-/-}$ HFD model due to SerBut, but not NaBut, treatment (Figure 5D). Representative images are shown (Figure 5E-L).

We then asked if SerBut's effects on disease pathology and inflammation may be partially mediated by changes in lipid metabolism by measuring lipogenic and lipid oxidation gene expression by qPCR after treatment for 6 weeks (Extended Figure. 10F-L). SerBut treated mice have significantly reduced expression of acly compared to NaBut treated mice but nor compared to water treated groups. No significant changes were seen in de novo lipogen-

esis, namely fatty acid synthase (fasn), and acetyl CoA carboxylase 1 (acaca). Carnitine palmitoyltransferase 1a (cpt1a), the rate limiting enzyme of beta oxidation, also was not significantly changed but showed a strong trend toward reduction compared to water treated groups (p= 0.06). Taken together, this data suggests that reduction in liver lipogenesis nor increase in beta oxidation had measurable impact on phenotypic changes.

2.3 Discussion

Butyrate, a key link between gut microbiota and metabolic health, has long been investigated for its beneficial effects in many metabolic and immune dysregulated states. The vast majority of either physiological (via microbial fermentation in the distal gut) or orally-administered butyrate is metabolized by intestinal colonocytes as a primary energy source, limiting its anti-inflammatory efficacy that might otherwise occur with systemic exposure. Since very little enters circulation, the primary effect of orally-dosed free butyrate is hypothesized to be on the intestinal lining and microbiome rather than distant organs and immune cells(21, 22). In the gut, butyrate promotes differentiation of colonic Treg cells via HDAC inhibition, allowing increased peripheral Treg cells by emigration(23, 24). Our lab previously engineered butyrate to escape the gut, utilizing esterification to a hydroxyl-containing amino acid, serine, hypothesized to allow butyrate transport into the portal blood through small intestinal amino acid transporters(1). This modification may additionally allow transit across the plasma membrane via transporters, dependent on the cell type. In this study, we assayed free, active butyrate in the gut contents and tissues separated by gut segment (Figure 2, Extended Figure. 2). We found that only in small intestine tissue did SerBut-dosed mice show a significant increase in free, active butyrate by LC-MS/MS. This data, which we believe to be novel, supports our hypothesis that SerBut escapes in the small intestine, evading consumption in the distal gut. Due to the promiscuous nature of amino acid transporters in the intestine and the failure of previous knockout experiments to inhibit amino

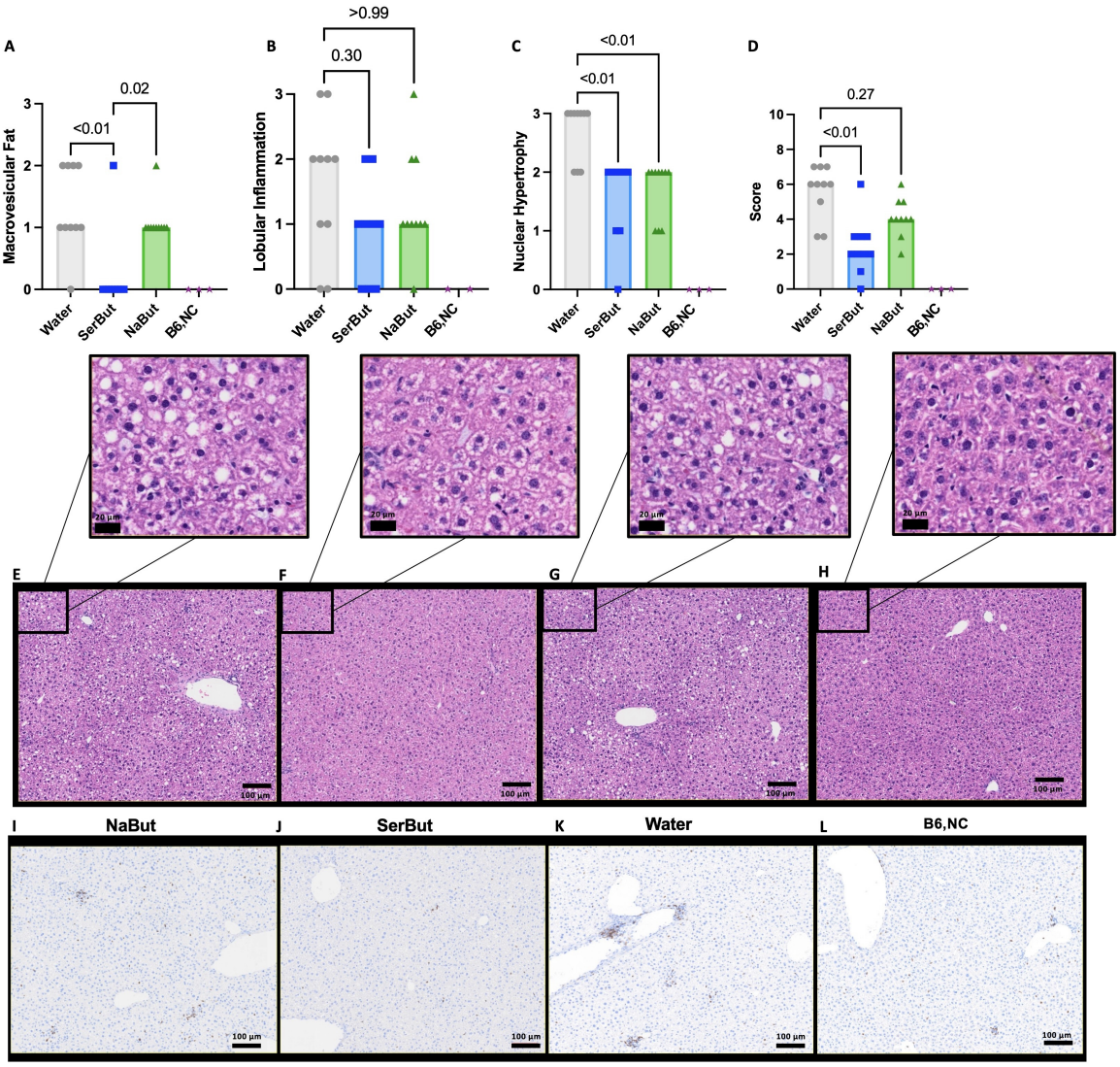

Figure 2.12: **SerBut suppresses liver injury induced by high-fat diet feeding.A-E.** Histology of livers taken after 6 weeks of treatment. Histological scoring of livers: **A.** Macrovesicular fat, **B.** Lobular inflammation, **C** Nuclear hypertrophy, **D.** Overall score, and **E-H.** Representative images of H&E staining in **E.** NaBut, **F.** Serbut, **G.** Water, or **H.** B6,NC. "B6,NC" denotes three age matched C57BL/6 mice on a normal diet as a non-statistical comparison. **I-L.** Representative images of immunohistochemistry stained $CD3^+$ immune cells in **I.** NaBut, **J.** SerBut, **K.** Water, **L.** or age-matched wild-type controls. "B6,NC" denotes three age matched C57BL/6 mice on a normal diet as a non-statistical comparison to visualize healthy examples. n=10 per group in a single experiment for all groups. Kruskal-Wallis test for multiple comparisons was used. Score is calculated as the sum of scores displayed in A-D graded by a pathologist. Figure 5A,C. were graded using H&E-stained slides. Figure 5B was graded using IHC stained slides for $CD3^+$ immune cells. Representative imaged were chosen based on average score for a particular treatment group.

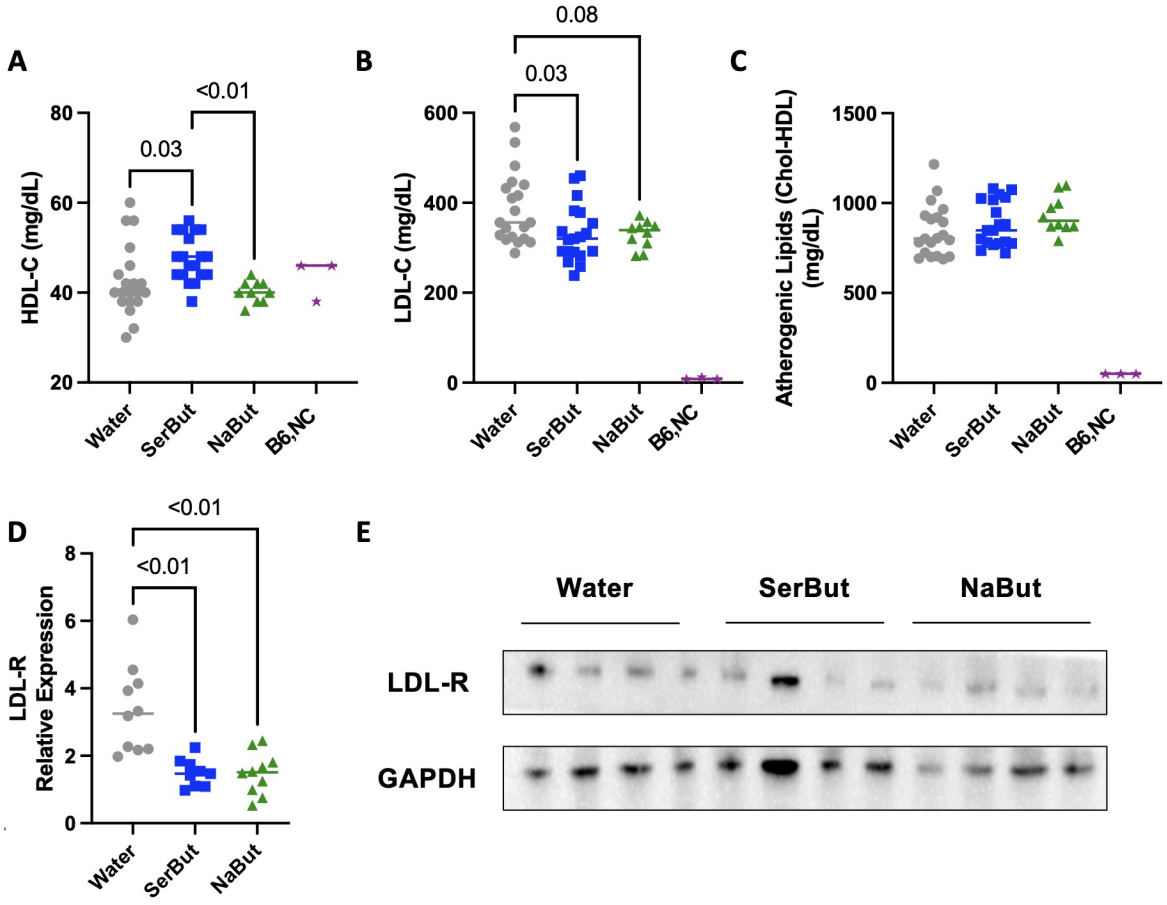

Figure 2.13: **A.** HDL-C in plasma. **B.** LDL-C in plasma. **C.** Atherogenic Lipids in plasma. Livers of female ApoE$^{-/-}$ mice on a HFD in concert with 150 mM SerBut, NaBut, or water ad libitum for 6 weeks were taken and homogenized for analysis. **D.** Western blot quantification of LDL-R. **E.** Representative Western blot of LDL-R and GAPDH on livers. Quantification of mean optical density of each Western Blot band was normalized over the mean optical density of the same samples GAPDH band. Statistical analyses were performed using a one-way ANOVA with a Dunnett's, Welch's (if standard deviations were significantly different by Bartlett and Brown-Forsyth tests), or Kruskal Wallis's (if data were not normally distributed determined by Shapiro-Wilk test) post-test.

acid transport, we did not investigate the specific amino acid transporter responsible for SerBut's uptake(9), hypothesizing that SerBut transport is mediated by multiple amino acid transporters.

In this study, we investigated the progression of cardiometabolic disease in ApoE$^{-/-}$ mice fed a HFD for 6 weeks in concurrence with SerBut or NaBut administered in drinking water ad libitum (Figure. 3A). SerBut significantly suppressed atherosclerosis development, reducing plaque and necrotic core area in the aortic root and plasma LDL-C levels without affecting body weight (Figure. 3H, Figure. 4A,H). SerBut did not induce liver injury or elevate LDL-R as is common in some current standard-of-care therapeutics, but in fact inhibited liver injury induced by HFD feeding (Figure. 4E-F, Figure. 5, Extended Figure. 10). These results support previous work showing butyrate's protection against LPS-induced inflammatory liver injury through NFκB suppression(25) and liver injury in an HFD-fed model(16) without suffering from dosing and translational limitations.

The in vivo studies performed in this manuscript contain important limitations that may influence human translation. The ApoE$^{-/-}$ murine model of atherosclerosis is advantageous due to its representation of inflammation yet has several limitations in recapitulation of human lipid metabolism. For example, since the lipid lowering effect of statins is partially dependent on the presence of ApoE(26, 27), direct comparisons to the standard-of-care are precluded in this model. Furthermore, analysis of long-term suppression of liver injury would require longer periods of HFD feeding, as HFD-fed murine models of liver injury do not recapitulate human disease until 8-16 weeks of HFD(28). The murine ApoE$^{-/-}$ model lacks human lipoprotein genes cholesteryl ester transfer protein (CEPT) expression, human cardiovascular disease contributor lipoprotein(a), and differential bile acid composition. Thus, the lipid lowering and immunometabolic modulatory properties of SerBut, especially those potentially due to modulation of liver metabolism, require further investigation to understand how these differences could impact translation.

Therapeutically targeting inflammation to reduce cardiovascular disease has shown promise in recent trials such as the CANTOS (Cardiovascular Risk Reduction Study [Reduction in Recurrent Major CV Disease Events])(29) and COLCOT (Colchicine Cardiovascular Outcomes Trial)(30) trials. In these trials, patients with relatively low levels of serum LDL-C or previous myocardial infarction events, respectively, saw reduced adverse cardiovascular events with immunotherapy. These results strongly suggest that inflammatory pathways play an important role in disease promotion. However, these trials used broad anti-inflammatory medications: the IL-1-neutralizing antibody canakinumab and the NLRP3 inflammasome inhibitor colchicine, respectively. A significant increase in lethal infections led to concerns about the safety of these drugs, although low-doses of colchicine have been FDA approved. Despite these challenges, research on anti-inflammatory approaches toward treating and suppressing cardiovascular disease became an important step toward better therapeutics(31).

Butyrate demonstrates anti-inflammatory NFκB -suppressing effects in myeloid cells by acting as an HDAC inhibitor(32), preventing NFκBp65 from binding inflammatory gene promoters(33). Downstream of NFκBactivation, the NLRP3 inflammasome, in concert with caspase-1, cleaves pro-IL-1β to its active form. Active IL-1β stimulates enhanced secretion of IL-6 and IFNγ along with other pro-inflammatory cytokines. We previously showed that SerBut maintains the HDAC inhibition activity of free butyrate(1). Here we further demonstrate SerBut's anti-inflammatory effect, showing that SerBut suppresses NFκB , downregulates iNOS expression, and reduces secretion of pro-inflammatory cytokines in macrophage-like cells in vitro (Figure. 1C-I).

We note that esterases that can cleave SerBut to yield bioactive butyrate are both extracellular and intracellular. Different relevant cell types may have many different import capabilities for both SerBut and hydrolyzed butyrate. SerBut presumably enables entry to the cytoplasm and liberation of free butyrate therein via intracellular esterases in vivo in various cell types. In addition to acting as a delivery vehicle for free butyrate, there are

possible disparate molecular mechanisms of SerBut as a full construct that are not investigated in this manuscript. There are a variety of tissue-specific esterases that could cleave SerBut, many of which are different between humans and mice(34). Increased bioavailability of free, active butyrate (Figure. 2, Extended Figure. 2) shows that SerBut is indeed cleaved in assayed tissue types and leads to improvements in cardiometabolic health in each tissue of interest (aorta, heart, and liver). However, esterase expression differences between human and mice could lead to differing results in humans. It is yet to be seen if these differences will prove beneficial or detrimental to the translation.

In murine atherosclerosis, SerBut reduced total immune cells, monocytes, and $CCR2^{+}$ monocytes in the aorta compared to water-treated controls (Figure. 3M-O). This indicates suppression of myeloid activation, potentially resolving atherogenic inflammation and reducing recruitment(35). Systemically, SerBut reduced the pro-inflammatory cytokines IL-6 and IFN in the plasma (Figure. 3Q,R) and circulating neutrophils (Figure. 3S). A reduction in circulating monocytes, neutrophils, and platelets has previously been seen as a side effect in clinical trials investigating HDAC inhibitors(36). This side effect has inhibited the use of small molecule HDAC inhibitors for use in chronic diseases. It is an open question whether use of SerBut in humans would produce these complications, however reduced inflammatory cells in circulation reduce the number of cells that can contribute to plaque formation, providing more benefit than complication. Importantly, we previously showed that although SerBut reduces innate immune activation, and that it does not dampen responses to vaccination in the presence of an adjuvant consisting of alum admixed with the TLR4 agonist monophosphoryl lipid A(1). Questions remain on the effect of SerBut treatment on innate immune responses to infection; however, previous reports suggest that the anti-inflammatory effects of butyrate are context dependent(1).

In summation, we have demonstrated that systemically bioavailable butyrate dosed through SerBut is able to modulate immunity, thus suppressing atherosclerosis progression and liver

pathology in the ApoE$^{-/-}$ HFD murine model of atherosclerosis. Butyrate has long been of interest in cardiometabolic disease, but its exploration has been limited by its low bioavailability and aversive sensory experience. Our results show that addressing these challenges significantly accentuates the benefit of butyrate dosing in the ApoE$^{-/-}$ model of atherosclerosis compared to treatment with NaBut. SerBut's liver protective effect was also accentuated compared to NaBut, likely attributed to enhanced exposure of the liver as indicated in our biodistribution study. These learnings may be useful in considering simple, low toxicity combinations to reduced progression of cardiometabolic disease, including in patients with previous liver disease, liver injury, or mutations in the ApoE gene diminishing their response to statins(26, 27, 37).

2.4 Materials and Methods

2.4.1 Sex as a Biological Variable

This study was conducted using female ApoE$^{-/-}$ mice. Sex differences are known to influence the development of atherosclerosis and metabolic disease (67). For example, female mice typically develop larger aortic root lesions earlier than male mice. Female mice also exhibit a stronger adaptive immune response to oxidized LDL and a more robust innate immune response to TLR stimulation (68, 69). In contrast, pharmacological interventions such as PPARγ agonists and IFNγ deficiency have shown therapeutic benefits primarily in male mice (70,71). These observations suggest that sex may influence the magnitude of therapeutic response in ApoE$^{-/-}$ mice. However, because inflammation is a central feature of atherosclerosis in both sexes, and because of the complex immunological mechanisms involved in our study, it is difficult to predict whether sex-specific differences would enhance or attenuate the observed effects. To reduce biological variability and maintain clarity in data interpretation, we conducted all experiments in a single sex.

2.4.2 Synthesis of SerBut

SerBut was synthesized as described previously(1). Briefly, L-Serine (20 g, 0.19 mol) was added to trifluoroacetic acid (200 mL), and the suspension was stirred for 30 min until everything dissolved. Butyryl chloride (25.7 mL, 0.23 mol) was then added to the solution, and the mixture was stirred for 2 hr at room temperature. The reaction was then transferred to an ice bath, and diethyl ether (500 mL) was added, which resulted in a precipitation of a white solid. The resulting fine white precipitate was collected by filtration, washed with cold diethyl ether, and dried under vacuum to afford 26.3 g of O-butyryl-L-serine (0.15 mol, 79%). The final product was confirmed by 1H NMR (500MHz, DMSO-d6) [ppm]: 0.88 (3H, t), 1.55 (2H, m), 2.32 (2H, t), 4.30 (1H, t), 4.43 (2H, d), 8.66 (2H, s), 14.06 (1H, s).

2.4.3 NFkB activation in RAW 264.7 Blue Macrophages

NFκB inhibition was assayed using the NFκB-SEAP reporter cell line, RAW-Blue(Cat: raw-sp, InvivoGen). Cells were plated in round-bottom 96 well plates at 100,000 cells per well and co-cultured with different concentrations of either NaBut or SerBut (from 0.15 mM to 12 mM) for 24 hr. After the addition of butyrate, cells were rinsed with phosphate buffered saline (PBS) and then stimulated with 200 ng/mL LPS in media for 6 hr.

2.4.4 Activation study on RAW 264.7 Macrophages

RAW 264.7 macrophages were cultured at 37°C and 5% CO2 in the DMEM media supplemented with 1 mM HEPES, 1 mM sodium pyruvate, 10% FBS with penicillin/streptomycin. Cells were plated in round-bottom 96 well plates at 100,000 cells per well and incubated with different concentrations of either NaBut or SerBut (from 0.15 mM to 12 mM) for 24 hr. Cells were then rinsed with PBS and then stimulated with 200 ng/mL LPS in media for 6 hr. The supernatant of cell culture was collected and analyzed by LEGENDPlex to analyze the concentrations of cytokines (BioLegend). Cell phenotype was analyzed using flow cytometry

(Cytek Aurora).

2.4.5 Cell Viability & Cytotoxicity Assay

CellTiter 96 AQueous one Solution Cell Proliferation Assay (MTS) (Cat# G3582, Promega) was used to analyze cytotoxicity of SerBut and NaBut at various concentrations (0.15 mM - 12 mM) in RAW 264.7 macrophages. The CellTiter 96® AQueous One Solution Reagent contains a tetrazolium compound [3-(4,5-dimethylthiazol-2-yl)-5-(3-carboxymethoxyphenyl)-2-(4-sulfophenyl)-2H-tetrazolium, inner salt; MTS] and an electron coupling reagent (phenazine ethosulfate; PES). Assays are performed by adding a small amount of the CellTiter 96® AQueous One Solution Reagent directly to culture wells, incubating for 1–4 hours and then recording absorbance at 490nm with a 96-well plate reader. The quantity of formazan product as measured by the amount of 490nm absorbance is directly proportional to the number of living cells in culture. The forzaman product can only be formed when cleaved by the mitochondria of living cells. The reading of the dye is normalized to untreated cells (100%) and triton-X treated cells (0%).

2.4.6 Mice

Female ApoE$^{-/-}$ mice, aged 6-8 weeks, were purchased from JAX (strain code: 002052 - B6.129P2-Apoetm1Unc/J). Female C57BL/6 mice aged 6-8 weeks were purchased from Charles River (strain code: 027, Charles River). C57BL/6 and ApoE$^{-/-}$ mice were maintained in a specific pathogen-free (SPF) facility at the University of Chicago. Mice were maintained on a 12 hr light/dark cycle at a room temperature of 20-24°C. All protocols used in this study were approved by the Institutional Animal Care and Use Committee of the University of Chicago.

2.4.7 Biodistribution of SerBut

ApoE$^{-/-}$ mice on 6 weeks of HFD were orally gavaged with equimolar 272 μM butyrate, equal to 24 mg butyrate (52 mg SerBut or 30 mg NaBut (equimolar butyrate). At 3 hr post-administration, mice were anesthetized under isoflurane and blood was collected via cheek bleeding, and mice were then transcardially perfused with a minimum of 30 mL PBS containing 1 mM EDTA. Organs, including liver, mesenteric lymph nodes (mLNs), inguinal lymph nodes, spleen, lung, heart, aorta, small intestine and large intestine were collected and then transferred to -80°C until further processing.

Blood was spun down to remove clotting agents and plasma was frozen. To extract butyrate from plasma or organs, a 1:1 v/v acetonitrile (ACN) to water solution was used. Plasma was mixed 1:1 with the ACN/water solution and centrifuged to remove denatured proteins. Organs were weighed, transferred to Lysing Matrix D tubes, and combined with the 1:1 v/v ACN/water solution. Samples were then lysed using a FastPrep-24 5G homogenizer (MP Biomedicals) and centrifuged. The supernatants were collected for butyrate measurement.

Samples were prepared and derivatized as described previously(1). A 3-nitrophenylhydrazine (NPH) stock solution was prepared at 0.02 M in water:ACN 1:1 v/v. A 1-ethyl-3-(3-dimethylaminopropyl)carbodiimide (EDC) stock solution (with 1% pyridine added) was prepared at 0.25 M in water:ACN 1:1 v/v. The internal standard, 4-methylvaleric acid, was added. Samples were mixed with NPH and EDC stocks at a 1:1:1 volume ratio. The mixture was heated in a heating block at 60°C for 30 min. Samples were then filtered through 0.22 μm filters and transferred into HPLC vials, which were stored at 4°C before analysis.

An Agilent 6460 Triple Quad MS-MS was used to detect the derivatized butyrate. Both derivatized butyrate-NPH and 4-methylvaleric-NPH were detected in negative mode. Column: ThermoScientific C18 4.6 $\times$ 50 mm, 1.8 μm particle size, at room temperature. Mobile phase A: water with 0.1% v/v formic acid. Mobile phase B: acetonitrile with 0.1% v/v formic

acid. Injection volume: 5.0 μL. Flow rate: 0.5 mL/min. Gradient of solvent: 15% mobile phase B at 0.0 min; 100% mobile phase B at 3.5 min; 100% mobile phase B at 6.0 min; 15% mobile phase B at 6.5 min. The MS conditions were optimized using pure butyrate-NPH or 4-methylvaleric-NPH at 1 mM. The fragment voltage was set to 135 V, and the collision energy was 18 V. Multiple reaction monitoring (MRM) of 222 $\rightarrow$ 137 was assigned to butyrate, and MRM of 250 $\rightarrow$ 137 was assigned to 4-methylvaleric acid as the internal standard. The ratio between MRM of butyrate and 4-methylvaleric acid was used to quantify butyrate concentration. The final butyrate content in each organ was normalized by organ weight.

2.4.8 SerBut Administration in ApoE$^{-/-}$ model

For 6 weeks, mice were freely administered water with filtered 150 mM SerBut, NaBut or DI Water. SerBut water was pH adjusted using 10 M NaOH to a final pH of 7.4. NaBut water was not pH adjusted and had a pH of approximately 8. In concert, high fat diet with 42% from fat and 0.2% total cholesterol (Envigo, Cat TD-88137) was freely accessed by mice. After 6 weeks, mice were euthanized. The lymph nodes (mesenteric and inguinal), spleen, heart, and aorta were harvested and processed for flow cytometry analysis62. Liver was harvested and part was homogenized in TPER (tissue protein extraction reagent) buffer (Invitrogen, Cat: 78510) supplemented with protease inhibitor mini tablets (Thermo Scientific, Cat: PIA32955) for western blot. The remaining liver was fixed with 4% paraformaldehyde and embedded in paraffin for histological analysis.

2.4.9 Flow cytometry and Antibodies

Flow cytometry was performed using BD LSRFortessa or a Cytek Aurora full spectrum cytometer. Data were analyzed using FlowJo version 10.8.0. Antibodies against the following markers were used in the RAW 264.7 Macrophage in vitro studies: CD86 (BV421, Cat: 564198, BD Horizon), CD80 (BC650, Clone: 16-10A1, Cat: 104732, Biolegend), iNOS (APC,

Clone: CXNFT, Cat: 17-5920-9, Invitrogen), eFluor 780 Viability Dye (Cat: 65-0865-14, Invitrogen). Antibodies against the following markers were used in the atherosclerosis mouse models: F4/80 (FITC, Clone: BM8, Cat: 123108 ,BioLegend), CD3e (BV605, Clone: 145-2C11, Cat: 563565, BD Biosciences), CD4 (BUV496, Clone:GK 1.5, Cat: 612952), RORγt (AF647, Clone: Q31-378, Cat: 562682, BD Biosciences), FoxP3 (AF488, Clone: MF23, Cat: 560403, BD Biosciences), CCR2 (PE, Cat: FAB5538P, R&D Systems), Ly6C (APC-Cy7, Cat: 128026, Clone: HK1.4, BioLegend), Ly6G (AF488, Cat: 127626, BioLegend), Live Dead Blue (Cat: 123105A, Invitrogen), CD8 (APC-Cy7, Clone: 53-6.7, Cat: 100714, BioLegend), CD45 (BUV805, Clone: 30-F11, Cat: 368-0451-82, Invitrogen), CD25 (PerCP-Cy5.5, Clone: PC61, Cat: 102030, BioLegend).

2.4.10 Flow Cytometry of the Aorta

As previously described (38), mice were pressure perfused with 30 mL of PBS via the left ventricle after severing the inferior vena cava. The heart with the ascending and descending aorta to the diaphragm was harvested. The perivascular adipose tissue was carefully removed by microdissection while keeping the adventitia intact. The aorta was then cut at the base of the heart and placed in digestion media then cut pieces. To create a single cell suspension, digestion media consisted of DMEM (Gibco) supplemented with 0.5 mM CaCl2 and 2.5 mM MgCl2, 125 U/ mL collagenase XI (Sigma-Aldrich), 450 U/mL collagenase I (Sigma-Aldrich), 60 U/mL hyaluronidase, (Sigma-Aldrich), and 60 U/mL DNase I (Sigma-Aldrich). After 45 min of digestion at 37°C with orbital shaking, aortas were passed through a 70 μm cell strainer, rinsed, pelleted, and plated into a U-bottom 96-well microplate for staining. Cells were washed in PBS and stained for 15 min on ice with 1:500 Live/Dead Fixable Violet Dye (Invitrogen) and 1:200 anti-mouse CD16/32 (clone 93, BioLegend). Cells were washed in PBS supplemented with 2% FBS (FACS buffer) and stained for 30 min on ice with surface antibodies at a 1:200 dilution in a 1:1 mixture of FACS buffer and

Brilliant Stain Buffer (BD Biosciences). Cells were washed with FACS buffer and PBS and fixed with 2% paraformaldehyde on ice for 20 min. Cells were washed twice with PBS and resuspended in FACS buffer. Precision count beads (BioLegend) were used to determine absolute cell counts. In this study, antibodies used included: CD16/32 (Clone: 93, Cat: 101302, Biolegend), CCR2 (PE, Clone, Cat: FAB5538P, R&D Systems), CD11b (BV605, Clone: M1/70, Cat: 101257, Biolegend), CD11c (PE-Cy7, Clone: HL3, Cat: 558079, BD Biosciences), CD19 (APC, Clone: 1D3, Cat: 152412, Biolegend), CD3e (BUV395, Clone: 145-2C11, Cat: 563565), CD45 (BV786, Clone: 30-F11, Cat: 564225, BD Biosciences), F4/80 (BUV496, Clone: T45-2342, Cat: 750644, BD Biosciences), I-A/I-E (PerCP-Cy5.5, Clone: M5/114.15.2, Cat: 107626, Biolegend), Ly-6C (APC-Cy7, Clone: HK1.4, Cat: 128026, Biolegend), and Ly-6G (FITC, Clone: 1AB, Cat: 11-9668-80, eBioscience)

2.4.11 Sectioning and Oil Red O Staining Aortic Root:

Hearts were fixed in 4% paraformaldehyde for 24 hr and cryopreserved with sucrose (15% sucrose for 24 hr, 30% sucrose for 24 hr, 1:1 30% sucrose and OCT) before being embedded in OCT (Fisher Scientific). Frozen embedded samples were sectioned at 8 µm. Aortic root sections were brought to room temperature and rehydrated with PBS. Staining solution was freshly prepared by mixing 3 parts Oil Red O (0.5% in isopropanol, Sigma Aldrich) with 2 parts water. The solution was filtered through a 0.22 µm PES syringe filter (Millipore) and immediately pipetted onto sections. After 15 min in a sealed dark chamber, sections were washed three times with tap water and immediately imaged. Images were analyzed using QuPath (v0.5.0). Each leaflet was circled broadly to include the plaque then subsequently trained on the QuPath pixel classifier using the software's artificial neural network. Training images were then tested and validated to identify the plaques to calculate their area and exclude non-plaque structures in the image. Plaque sizes were subsequently averaged and used to determine %ORO positive plaque area in the leaflet.

2.4.12 Immunohistochemistry and Stary Plaque Severity Grading:

Frozen aortic root sections were fixed in Zamboni fixative for 10 minutes. After TBS wash, slides were loaded on Leica Bond RX automated stainer. Anti-mouse CD68 antibody (Biolegend, catalog 137001, clone FA-11) (1:4000) was applied on tissue sections for 60 minutes incubation at room temperature. Following TBS wash, tissue sections were incubated with rabbit anti-rat IgG (Thermo Fisher, #31219) 30 minutes. The antigen-antibody binding was detected using Polymer -HRP (Leica Biosystems, Bond Polymer Refine Detection kit, DS9800). The slides were coverglassed by autocoverslipper (Tissue-Tek Glas g2). Stary plaque severity grading was done as previously described(10). Briefly, each individual mouse was scored if there were at least two aortic root sections showing all three valves of the heart that could reasonably be scored. Each valve was scored individually per aortic root section and subsequently averaged per section. All sections were averaged per mouse for a final score. Sections were graded blinded.

2.4.13 Blood Chemistry & Inflammatory Cytokines in Plasma

Blood Chemistry was performed on an Alfa Wasserman ACE Axcel Chemistry Analyzer. The following reagent kits from Alfa Wasserman were used in analysis of Plasma: Lipase (Cat#SA1045), HDL-C (Cat#SA2038, LDL-C (Cat#SA1040), Aspartate Aminotransferase (AST) (Cat#SA1053), Alanine Transaminase (ALT) (Cat#SA1052). LEGENDPlex was utilized to analyze the concentrations of inflammatory cytokines (BioLegend).

2.4.14 Histological Grading and Scoring of Livers

Livers were collected and fixed in 4% paraformaldehyde prior to paraffin-embedding. 8 µm thick slides were sectioned and stained by either immunohistochemistry for $CD3^{+}$ immune cells or H&E. Digital image files were created with an Olympus VS200 Research Slide Scanner (Olympus / Evident, Center Valley, PA) with a Hamamatsu ORca-Fusion camera (Hama-

matsu Photonics, Skokie, IL) at 40X magnification. Individual images were created with the OlyVIA Viewer software (Olympus / Evident, Center Valley, PA). Scoring and grading was performed by a pathologist as previously described48. Immunohistochemistry grading was informed by age-matched WT controls. In age-matched WT controls, $CD3^+$ immune cells were seen scattered without distinct aggregate formation nor associated tissue reaction. In a 400x field, we observed up to 25 $CD3^+$ immune cells scattered in an even distribution with rare events of up to 10 periductal $CD3^+$ positive immune cells but with no associated ductal or parenchymal reaction. A score of 1 was given to samples with one focus in which more than 10 periductal $CD3^+$ lymphocytes are found in a 200x field, hinting mild periductal inflammation. Furthermore, a score of 2 corresponds to 2 to 5 instances of more than 10 periductal $CD3^+$ immune cells in a 200x field. Any sample exceeding this threshold was scored a 3.

2.4.15 Statistical Analysis

Statistical analysis and plotting of data were performed using Prism 10.0.2 (GraphPad), as indicated in figure legends. One-way ANOVA with Dunnett's, Brown-Forsythe and Welch's (if standard deviations were significantly different), or Kruskal-Wallis post-test (if data were not normally distributed) were used for multiple comparisons. Bartlett's test and Brown-Forsyth test were performed to determine if assumption of equal standard deviations were appropriate. If $P<0.05$, Brown-Forsythe and Welch ANOVA tests were performed assuming different standard deviations. Normality analysis was done by Shapiro-Wilk test. An unpaired Students t-test was used for pairwise comparisons. Welch's t-test was used if standard deviations were significantly different. If data was not normally distributed, determined by Shapiro-Wilk normality test, a Mann-Whitney test was used.

2.4.16 Immunofluorescence Staining of the Aortic Root:

Aortic root sections were brought to room temperature and rehydrated with PBS and permeabilized with 10% dimethyl sulfoxide (DMSO).Sections were blocked with 0.05% casein in PBS and stained overnight at 4°C with rat monoclonal anti-mouse CD68 at 1:400 (Biolegend, clone FA-11) and rabbit polyclonal anti-mouse iNOS at 1:50 (Proteintech, 18985-1-AP). Sections were then washed with PBS with 0.05% Tween (PBS-T) and incubated for 1 hr at room temperature with secondary antibodies AlexaFluor488 donkey polyclonal anti-rabbit IgG at 1:500 (Invitrogen, A21208) and AlexaFluor555 donkey polyclonal anti-rabbit IgG at 1:500 (Invitrogen, A31572). Sections were washed again in PBS-T (phosphate buffered saline, 0.1% Tween 20) and PBS and mounted with ProLong Gold Antifade Mountant with DAPI (Invitrogen). Slides were imaged with DMI8 inverted fluorescence microscope (Leica Microsystems) and analyzed with QuPath (v0.5.0).

2.4.17 16S rRNA Sequencing

Feces were collected and stored at -80°C. Sequencing was performed as previously described39. Bacterial DNA was extracted using the QIAamp PowerFecal Pro DNA kit (Qiagen). The V4-V5 hypervariable region of the 16S rRNA gene from the purified DNA was amplified. Illumina sequencing-compatible unique dual index adapters were ligated onto pools using the QIAsep 1-step amplicon library kit (Qiagen). Library quality control was performed using Qubit and Tapestation before sequencing on an Illumina MiSeq platform at the Duchossois Family Institute Microbiome Metagenomics Facility at the University of Chicago. This platform generates forward and reverse reads of 250 bp which were analyzed for amplicon sequence variants (ASVs) using the divisive amplicon denoising algorithm dada2 (v1.18.0) as our default pipeline for processing MiSeq 16S rRNA reads with minor modifications in R (v4.0.3). Specifically, reads were first trimmed at 190 bp for both forward and reverse reads to remove low quality nucleotides. Chimeras were detected and removed using the default

consensus method in the dada2 pipeline. Then, ASVs with length between 320 bp and 365 bp were kept and deemed as high quality ASVs. Taxonomy of the resultant ASVs were assigned to the genus level using the RDP classifier (v2.13) with a minimum bootstrap confidence score of 80. The ASV tables, taxonomic classification and sample metadata were compiled using the phyloseq data structure63. Subsequent 16S rRNA relative abundance analyses and visualizations were performed using R version 4.2.2 (R Development Core Team).

2.4.18 Microbiota Community Variation

All statistical analyses and graphical representations were performed in R using the packages Vegan (v2.6-4), Phyloseq (v1.42.0), Caret (v6.0-94), ggplot2 (v3.4.4), Ape (v5.7-1), and Corrplot (v0.92).

Taxa were agglomerated at genus level using the tax_glom function (Phyloseq package) in R. Reads were rarefied to an even depth using the rarefy_even_depth function (Phyloseq package). Finally, abundances were relativized using the transform_sample_counts function (Phyloseq package). To further clean data, null values and predictors with near-zero variances were removed using the nearZeroVar function (Caret package). To minimize the influence of cage effects, taxa that were present only in less than 10% of samples were removed.

Phylogenic trees were created using the rtree function (Ape package), which was subsequently merged onto the phyloseq object. Beta-diversity was calculated via weighted and unweighted Unifrac distances, as well as Bray-Curtis distances. The Ordinate function (Phyloseq package) was used with PCoA method to calculate distances for both weighted and unweighted Unifrac distances. Permutational multivariate analyses of variance using distance matrices were calculated using the adonis2 function (Vegan package). Plotting of Beta-diversity was performed using the plot_ordination function (Phyloseq Package, ggplot2 package).

2.4.19 Association Between Atherosclerosis Pathology and Treatment Variables (Exogenous Butyrate, Seryl Modification of Exogenous Butyrate, and Microbiome Variables)

Linear modelling was performed in a manner similar to Valles-Collomer et al64. Associations between taxa, butyrate, or Seryl modification of butyrate and pathology readouts after partialling out the effects of the other two treatment variables as covariates were assessed by fitting linear models. Pathology readouts (eg. Plaque % in the aortic root, LDL-C/Chol) were used as responsive variables, and treatment variables as explanatory/predictive variables. Multivariate linear models were performed using the lm R function (stats package). Standardization of predictor and response variables was performed using the scale function in base R. Associations were included as significant at $P<0.025$. In extended fig 5, values are shown as Rho correlation coefficients transformed from β coefficients as calculated below.

CHAPTER 3

A BRIEF HISTORY OF EFFEROYTIC MECHANISMS OF IMMUNE MODULATION

3.1 Preamble on Contributions

Gla domain carboxylation of GAS6 bridge protein was not understood prior as a useful immunological tool. Re-analysis and comparison of prior work by Dr. Joe Reda, published in their dissertation entitled, "RECOMBINANT FUSIONS OF ANTIGEN WITH MEDIATORS OF EFFEROCYTOSIS MODULATE ANTIGEN-SPECIFIC IMMUNE RESPONSES", is discussed in light of new analysis and hypothesis in this dissertation. New data collected by Dr. Joe Reda and Taryn Beckman are included in the results section. The Discussion section analyses and summarizes prior reported data from Dr Joe Reda's dissertation and new data published for the first time in this dissertation. Intellectual contribution to experimental design, data interpretation, and writing was performed by Taryn Beckman in collaboration with Joe Reda.

3.2 Efferocytosis

Efferocytosis (from Latin, 'efferre', 'to bring to the grave') is a type of phagocytosis of a dying cell that has proven critical in maintaining immune tolerance.1 Maintenance of homeostasis requires the daily clearance of billions of apoptotic cells in the human body via efferocytosis.(2,3) Defects in efferocytosis can cause or exacerbate numerous human pathologies including lupus, atherosclerosis, cancer, chronic inflammation and infections.4 When efferocytosis is ablated by genetic mutations or pharmaceutical interventions, inflammation quickly ensues, particularly in tissues with rapid cellular turnover.(2,5) Both mice and humans with defects in efferocytic machinery demonstrate higher rates of anti-nuclear antibodies in plasma, which are a hallmark sign of a breakdown of self-tolerance. Immune tolerance depends on central and peripheral mechanisms. Centrally, thymic T cells are screened for autoreactivity before maturing and emigrating from the thymus, with autoreactive clones undergoing elimination or becoming thymus-derived regulatory cells.(6,7) Peripheral toler-

ance occurs after T and B cells mature and leave the thymus or bone marrow, where antigen presentation can create tolerance to antigens via mechanisms such as anergy, clonal deletion, and induction of T regulatory Cells (Tregs). Thus, efferocytosis has been referred to as a key "brake" on immune activation because of its role in inducing and maintaining tolerance to proteins in the periphery, some of which may not be present in thymic central tolerogenic processes. For example, in type I diabetes, immunogenic neoantigens in the periphery arise following aberrant post-translational modifications.

The main pathway of efferocytosis begins with an apoptotic cell, which secretes find-me signals to recruit efferocytes and exposes eat-me signals such as phosphatidylserine (PS), typically confined to the inner leaflet of the plasma membrane. Eat-me signals are recognized by a range of efferocytic receptors and bridging molecules, including growth arrest specific 6 (GAS6). Efferocytic bridging molecules act as soluble opsonins with two functional termini, one of which binds PS, and the other binds receptors on APCs. In the case of GAS6, the N-terminal Gla domain binds PS in a g-carboxylation-dependent manner, whereas the C-terminus interacts with TAM receptor tyrosine kinases (e.g. Axl, MerTK) on innate APCs. Engagement of both termini of GAS6 tethers the APC to the dying cell and stimulates phagocytosis.(8) PS binding is required for TAM receptor crosslinking, internalization, and phagocytosis of the dying cell.(9) However, in the absence of PS binding capacity, GAS6 maintains the ability to signal through MerTK, albeit to a lesser extent and without inducing engulfment of the dying cell.(9)

3.3 Secondary Necrosis, TAM receptor signaling, and Phagocytosis in Efferocytosis

Efferocytosis was first appreciated to play a critical role in the suppression of secondary necrosis, the process by which uncleared dying cells lose membrane integrity and release inflammatory damage-associated molecular patterns (DAMPs). These observations led to

a model of efferocytosis as immunologically silent, dampening inflammatory signals without actively propagating new signals. However, more recent research has contrasted this by demonstrating that efferocytosis plays an active role in shaping APC phenotype and the immune microenvironment. Efferocytic machinery, including the GAS6/TAM axis, suppresses TLR signaling through NFkB, a canonical transcription factor regulating inflammation.10 Notably, TLR signaling in combination with cytokine signaling promotes TAM receptor expression, further underscoring the role of efferocytosis as a natural pivot from inflammation to immunoregulation(11,12). Innate immune cells use receptor signaling and material derived from the phagolysosomal degradation of efferocytosed dying cells to activate metabolic pathways that initiate polarization to a tolerogenic phenotype and promote further efferocytosis. The process of taking up a dying cell demands substantial metabolic adaptation, often requiring efferocytes to adopt an ornithine-based ("M2") metabolism, particularly in the case of serial efferocytosis. Cytokine secretion is also appreciably altered, with IL-10 secretion by efferocytes driving tolerogenic outcomes following the clearance of dying cells.(13) These observations have led to an updated model of efferocytosis, now appreciated to silence inflammatory cues associated with cell death and to skew both the immune microenvironment and innate immune cells towards tolerance. Refining our understanding to a minimal set of sufficient receptors to engage has been elusive, partially due to difficulty in experimentally decoupling secondary necrosis from TAM receptor signaling and cell debris clearance. Prior attempts, such as PS-decorated liposomes, are insufficient to study specific pathways of efferocytosis because they engage several efferocytic pathways. These challenges inhibit discovery of distinctive tolerogenic pathways and deeper understanding of the interplay between efferocytic tolerance mechanisms.

3.4 Immunological Mechanisms of Efferocytosis

Efferocytes have also been demonstrated to engage the adaptive immune system. For example, efferocytes upregulate PD-L1, engaging the PD-1/PD-L1 axis with adaptive immune cells and further tempering immune responses. The immunological consequences of this have been clarified in the context of cancer, in which MerTK signaling drives PD-L1 expression and subsequent tumor immune evasion. Phagocytosis delivers antigenic cellular debris to degradative lysosomes, leading to loading and presentation on MHC for presentation on the cell surface. Importantly, antigen presentation can occur without phagocytosis, as APCs can take up antigen through multiple pathways, such as pinocytosis. Efferocytosis has been repeatedly implicated as an important source of antigen for cross-presentation, the presentation of exogenous antigens on MHC I by APCs. It has long been appreciated that efferocytosis indeed affects antigen-specific immune responses, with delivery of PS liposomes or antigen-loaded apoptotic cells blunting immune responses by adaptive immune cells. Antigen presentation by MHC then crosslinks Ag-specific T cell receptors, enabling T cell proliferation. A variety of adaptive immune programs can result depending on the context of antigen presentation, such as APC expression of costimulatory markers. Although the GAS6 pathway of efferocytosis has been repeatedly implicated in regulation of inflammatory cycles, limiting autoimmune and allergic responses, the mechanism of differential antigen presentation required for modulation of adaptive immunity has not been well established. Multiple hypotheses have been proposed, including reduced presentation of antigen on MHC I due to efferocytic engulfment of antigen serving to limit induction of aberrant immune responses to self. Thus, while efferocytic programs modulate APC phenotype, it is incompletely understood how these phenotypic changes influence antigen presentation and resulting adaptive immunity driving phenotypic outcomes.

Antigen presentation, influenced by costimulation and microenvironment, can lead to multiple tolerance mechanisms by T cells such as anergy, clonal deletion, and suppression

via Tregs. Clonal deletion, for example, is the process by which a T cell clone is selectively killed by the immune system. When antigen is presented in the absence of costimulatory signals, clonal deletion proceeds via abortive proliferation, in which cells rapidly divide before undergoing apoptosis, resulting in the removal of that TCR from the repertoire(14,15). This mechanism can be considered passively tolerizing because it neutralizes present antigen-reactive T cells without preventing the future induction of antigen-specific inflammatory programs. In other cases, tolerogenic antigen presentation can lead to the induction of anergy, a state of functional unresponsiveness(14,16,17). Finally, T cells that have undergone chronic TCR stimulation can undergo exhaustion, a program distinct from anergy which is regulated by transcription factor TOX in $CD8^+$ T cells(18,19). Exhaustion results in persistent T cells lacking the capacity to mount responses to further antigenic stimulation(20). Notably, anergic and exhausted cells compete with other T cells both for presented antigen and for cytokine signals, thereby dampening reactivity to antigen, though with less strength than active mechanisms of tolerance.

In addition to passive mechanisms, T cell tolerance can occur by active mechanisms, defined by $FoxP3^+$ regulatory T cells (Tregs)(21). Regulatory T cells are known to be critical for the maintenance of immunological tolerance, with complete ablation of the Treg compartment leading to fatal inflammation. These cells have proven adept at undercutting inflammation in an antigen-specific manner through a variety of mechanisms, including communication with other cells via display of coinhibitory receptors such as PD-1 and CTLA-4, secretion of anti-inflammatory cytokines such as IL-10, competitive uptake of signals including IL-2, and modulation of the microenvironment with membrane-bound enzymes such as CD73. Furthermore, research has shown that peripheral induction of Tregs is required, as thymic Tregs fail to maintain tolerance to peripheral antigens. The observed modification of innate immune cells by efferocytosis pathways has been shown to modify T cell recruitment resulting in recruited tolerogenic Tregs and inhibited recruitment of $CD4^+$ and $CD8^+$ T cells

to the site of efferocytosis. However, it is unknown if efferocytes direct promote proliferation of the Treg compartment via tolerogenic antigen presentation.

Efferocytosis has been employed clinically to bolster tolerance to transplants and reduce autoimmune pathology via dosing of autologous apoptotic cells. Administration of autologous apoptotic cells can fail to induce tolerance, sometimes leading to inflammatory responses, termed "serum sickness," rather than intended acceptance of transplant. Thus, the efficacy of autologous apoptotic cell administration is unpredictable and the involvement of the adaptive immune response in suppression has long been mysterious. Many factors influence optimal functioning of efferocytosis including the ratio of phagocytes to apoptotic cells, the identity of the phagocytosing cell as a professional phagocyte or a neighboring cell, the size or content of the apoptotic cell, the rate and magnitude of death in a certain location, and the signaling molecules in the microenvironment surrounding the phagocyte(4). Current approaches to studying efferocytosis are limited to knock out studies to investigate the influence and exhaustiveness of these factors but are unable to isolate disparate machinery's influence on phenotype. Because efferocytosis is well known to be co-opted by some cancers to promote immune evasion, many attempts by engineers to modulate efferocytosis take the form of therapeutics nonspecifically blocking efferocytosis, such as small molecules and antibodies against TAM receptors currently in clinical trials for cancer therapy. Thus, there is strong evidence that efferocytosis could be leveraged to alleviate allergic and autoimmune diseases where aberrant inflammation triggers pathogenic presentation of self or harmless environmental components as antigen. While these discoveries are promising, there remain obstacles to therapeutic development leveraging efferocytosis, including unpredictable inflammatory side effects including serum sickness. This suggests that our characterisation and understanding of the immunological pathways by which efferocytosis produces tolerance is incomplete, resulting in an inability to finetune the desired response.One group recently produced a GAS6 recombinant protein, comprising GAS6 with an amyloid plaque antigen to

replace the Gla domain. They found this recombinant protein promoted clearance of amyloid plaque and reduced inflammation in the brain, validating pathway-specific engineering approaches to leverage efferocytosis(22). However, this work did not characterize adaptive immune responses downstream of GAS6 pathway stimulation(22). New experimental tools may enable study of efferocytic machinery and environmental factor influence on phenotypic outcomes, leading to development of improvements in efferocytosis that can in turn dampen tissue inflammation and reduce unwanted responses.

CHAPTER 4

EFFEROCYTOSIS MEDIATED BY BRIDGE MOLECULE GAS6 DRIVES RECIPROCAL TOLEROGENIC INTERACTIONS BETWEEN INNATE AND ADAPTIVE LEUKOCYTES

4.1 GAS6-OVA Fusion Protein Elucidates Influence of Antigen Presentation on Immune Outcomes

To unravel the interplay between an efferocytic antigen, the DC collecting it, and the T cell engaged in that immune synapse, we engineered a fully functional GAS6 bridge protein by fusing it to the model antigen ovalbumin (OVA, to yield GAS6-OVA, abbreviated as GO), providing a highly defined experimental tool to enable contextualization and characterization of efferocytic machinery and myeloid-lymphoid reciprocal signaling. Furthermore, we used a non-PS binding GAS6 model antigen fusion (ΔGO) to probe stages of efferocytosis apart from each other, namely the distinction between TAM receptor signaling and subsequent engulfment of apoptotic cells. Using an OVA-specific transgenic T cell model system, our tools enabled investigation into GAS6-dependent pathways of antigen-specific T cell tolerance in both $CD4^+$ and $CD8^+$ T cell compartments decoupled from secondary necrosis. Exposure to antigen via efferocytic GAS6-related pathways led to both MHC I and MHC II presentation, stimulating passive and active tolerance-inducing phenotypes in $CD4^+$ and $CD8^+$ T cell compartments in a cell-clearance-dependent manner, accompanied by T-cell-dependent tolerogenic biasing of the DC. In a murine adoptive transfer model, GO exposure induced hyporesponsiveness to antigenic challenge, including lessened abundance of antigen-specific T cells, expansion of robust $Helios^+FR4^{hi}$ Treg populations, and induction of the co-inhibitory marker TIGIT. In DCs, collection of GO induced a tolerogenic myeloid bias in a T-cell-dependent manner, including upregulation of PD-L1 and OX40L, and the TAM receptors themselves. Interestingly, this response in DCs depended on PS binding in the context of $CD8^+$ T cell but not $CD4^+$ T cell bridging. In a murine model, pre-exposure to GO led to abrogation of immune pathological response to an inflammatory airway challenge, demonstrating functional potency of this tolerogenic pathway with an endogenous repertoire. Thus, we provide evidence that stimulation of a single efferocytic pathway is sufficient to induce tolerogenic antigen presentation by both MHC I and MHC II, regardless

of homeostatic or inflammatory conditions, and that the tolerogenic context exists in both the myeloid and the lymphoid sides of the immune synapse.

4.2 Re-analyzed and Re-Interpreted Previously Reported Results

4.2.1 GAS6-OVA fusion protein preferentially binds phosphatidylserine and enhances antigen uptake by APCs in vitro.

In order to investigate efferocytosis's role in regulating antigen-specific immunity, we fused GAS6 with a common model antigen, ovalbumin (OVA). Given that the leader sequence of Vitamin-K-dependent proteins determines the extent of γ-carboxylation,(34) we elected to place GAS6 on the N-terminus, proximal to the leader sequence. OVA and GAS6 were linked together with a flexible glycine-serine (G4S) linker to prevent aggregation and steric hindrance of the active domains of GAS6 (Fig. 4.1A, B).(35)

Following expression of the GO fusion protein, we purified the supernatant via histidine affinity chromatography and size exclusion chromatography (Fig. S1A, B) and analyzed protein via SDS-PAGE to confirm expected size, relative purity, and lack of aggregation (Fig. 4.1C). We furthermore utilized anion-exchange chromatography to isolate the active, calcium-interacting form of GO with a γ-carboxylated Gla domain from the purportedly inactive form without γ-carboxylation (ΔGO) (Fig. 4.1D)(36). GAS6 is known to demonstrate higher affinity binding to PS than to other phospholipids, such as phosphatidylcholine (PC). We compared the binding of purified GO to both PS and phosphatidylcholine (PC) with an L1 chip, which captures liposomes.(37) GO exhibited preferential binding for liposomes containing PS compared to PC controls (Fig. 4.1E, Fig. S1C). To validate GO fusion protein specificity of uptake rather than stimulation of general pinocytosis, we asked if the covalent linkage by G4S linker was important for antigen uptake in GO or GAS6 and OVA mixing control treated bone marrow-derived DCs (BMDCs). The covalent binding, i.e. fusion, of

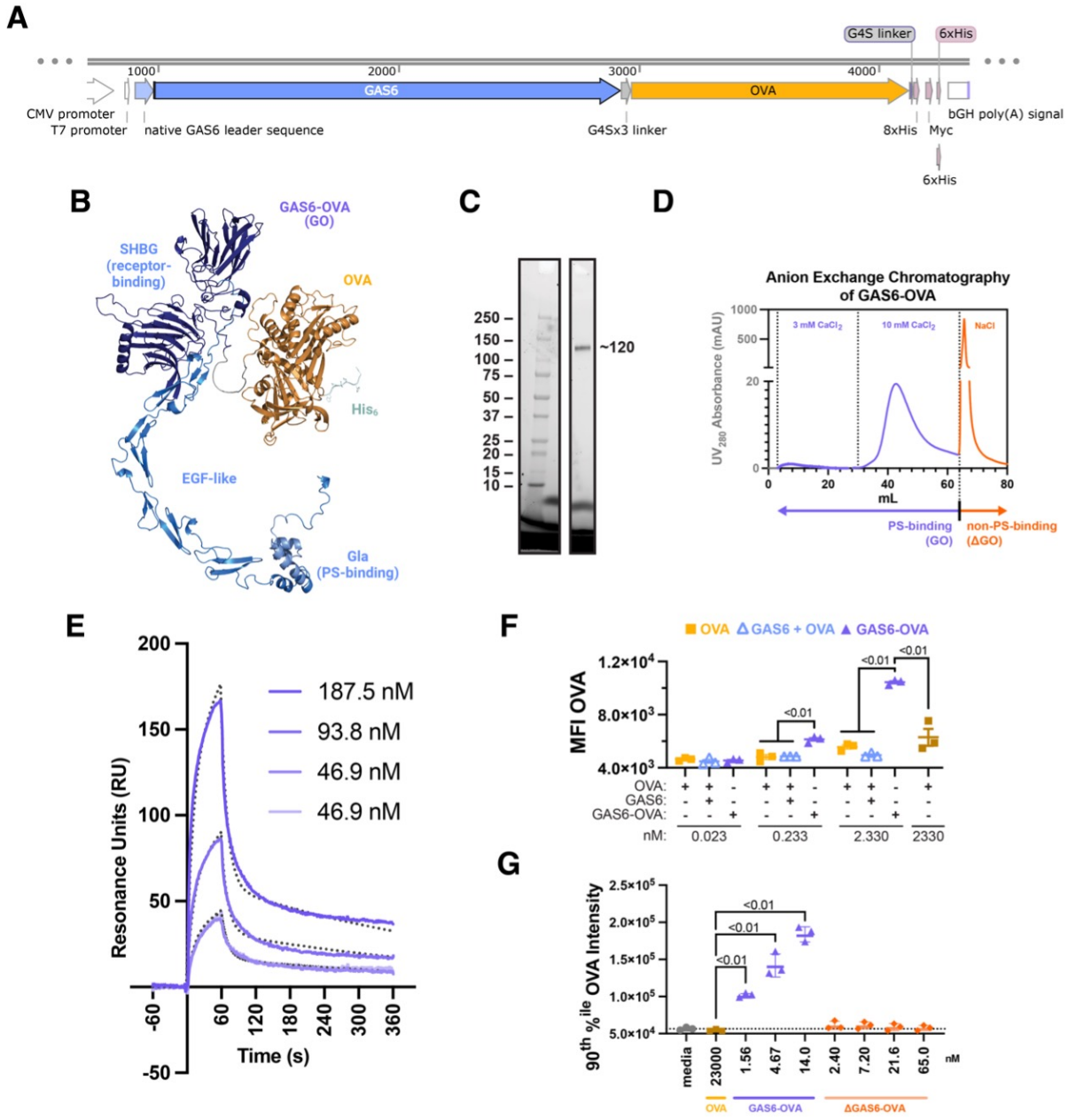

Figure 4.1: **Efferocytic antigen collection via GAS6 is enhanced by PS-specific binding.** The GAS6-OVA (GO) fusion was used to understand the role of PS binding in antigen collection by DCs. **(A)** Plasmid map illustrating the design of the GO fusion protein construct. **(B)** Predicted 3D structure of the GO protein via AlphaFold2. **(C)** SDS-PAGE analysis confirming the molecular weight and purity of purified GO protein. **(D)** Anion exchange chromatography profile of GO purification, distinguishing γ-carboxylated (CaCl2 fractions, purple) and non-γ-carboxylated (NaCl fraction, orange) forms based on elution conditions. **(E)** Surface plasmon resonance (SPR) analysis demonstrating specific binding of GO to PS-containing liposomes at three concentrations, including duplicate runs of the lowest concentration.

(Continued)**(F)** Flow cytometric analysis comparing uptake of OVA at two concentrations (yellow and brown squares), a physical mixture of GAS6 and OVA (empty blue triangles, G+O), and GO (purple triangles) by BMDCs. **(G)** Flow cytometric analysis comparing uptake of OVA at high concentration (brown squares), PS-binding GO at various concentrations (purple triangles), and non-PS-binding GO (ΔGO, orange diamonds).

GAS6 protein with the model antigen OVA was necessary to drive uptake of OVA (Fig. 4.1F, Fig. S1D). This uptake was temperature-dependent, as expected for cellular uptake (Fig. S1E). We then asked if γ-carboxylation of the Gla domain was required to drive uptake of OVA in GO- or ΔGO-treated BMDCs. γ-carboxylated GO demonstrated a temperature- and dose-dependent increase in uptake by BMDCs. By contrast, we did not observe any uptake in ΔGO- or high-concentration OVA (OVA hi)-treated controls (Fig. 4.1G).

4.2.2 Presentation by GAS6-OVA treated APCs leads to robust tolerogenic T cell responses in vitro

We employed GO to probe the nature of T cell priming induced by this efferocytic mechanism. To investigate this, we co-cultured antigen-pulsed mature BMDCs with CellTrace Violet-labeled OT-I or OT-II cells (Fig. 4.2A). During antigen presentation, costimulatory and coinhibitory ligands on antigen-presenting cells tune the outcome of T cell responses. In particular, PD-L1 has been shown to promote $CD4^+$ T cell tolerance when paired with antigen presentation on MHC-II.(38,39) BMDCs incubated with GO and antigen-specific T cells significantly increased expression of PD-L1 compared to both media, equidosed OVA, and high-dose OVA controls (Fig. 4.2B,C). GO-treated BMDCs drove substantial proliferation of both OT-I (Fig. 4.2D) and OT-II cells (Fig. 4.2E) as indicated by CellTrace Violet dilution, demonstrating that OVA epitopes are indeed presented on MHC I and MHC II following antigen collection from the GAS6 fusion.

Given that elevated checkpoint molecule expression on activated T cells suppresses inflammation,(40) we investigated whether antigen presentation by GO-exposed BMDCs altered

T cell phenotype in vitro with or without inflammatory stimulation by LPS. Phenotypic flow cytometric analysis of T cells included markers of activation (e.g., CD44, ICOS) and regulation (CTLA-4, PD-1, TOX). GO-exposed BMDCs induced distinct T cell phenotypes in both OT-I and OT-II cells, especially in the context of inflammatory stimulation (Fig. 4.2F,K, Fig. S2).

GO-exposed BMDCs drove upregulation of the inhibitory markers PD-1 and CTLA-4, which was significantly enhanced under proinflammatory conditions of LPS stimulation. GO treatment without LPS stimulation drove this tolerogenic phenotype significantly more than an 150-fold increased concentration of OVA (OVA hi) in the presence of LPS (Fig. 4.2G,H). In the $CD8^+$ T cell compartment, we observed significant expansion of terminally exhausted TIM-3^+PD-1^+ OT-I cells compared to unstimulated saline controls with or without LPS in GO-treated groups.(41,42) However, LPS-stimulated GO-treated groups drove 3-fold more expansion of terminally exhausted OT-I cells than unstimulated GO-treated groups. Equidosed and high-dose OVA did not expand this population, indicating that both inflammatory stimulation and efferocytic mediation were required for meaningful expansion of terminally exhausted OT-I cells (Fig. 4.2I). TOX is a transcription factor that is associated with exhaustion phenotypes in $CD8^+$ T cells.(26,43) TOX expression of LPS-stimulated OVA hi treated and unstimulated GO-treated OT-I cells was similar and significantly increased compared to unstimulated OVA hi treatment and all equidosed OVA treated controls. However, TOX expression was significantly increased in stimulated GO-treated OT-I cells compared to unstimulated GO-treated and stimulated OVA hi treated controls, indicating that GO treatment is sufficient without inflammatory stimulation to drive significant uptake and presentation of antigen, but has enhanced ability with stimulation (Fig. 4.2J). Taken together these data suggest that efferocytosis is not immunologically silent in $CD8^+$ T cells and instead promotes antigen-specific tolerance via upregulation of checkpoint receptors and an exhausted phenotype.

Similarly, in the $CD4^+$ T cell compartment, OT-II cells co-cultured with GO-treated BMDCs significantly upregulated inhibitory markers PD-1 and CTLA-4 (Fig. 4.2L,M). However, LPS stimulation reduced PD-1 expression compared to non-LPS-stimulated OT-II cells and ablated the difference between OVA hi controls (Fig. 4.2L). GO-treated OT-II cells expressed significantly higher proportion of CTLA-4 than OVA hi controls regardless of LPS stimulation (Fig. 4.2M). GO-exposed BMDCs drove significant expansion of Treg OT-II cells, which was significantly enhanced after LPS stimulation (Fig. 4.2N). CTLA-4 MFI on Tregs was significantly increased compared to controls treated with OVA hi, regardless of LPS simulation (Fig. 4.2O). These data suggest, like effects seen in CD8+ OT-I T cells, that GAS6-mediated antigen collection by efferocytosis drives antigen-specific tolerance in $CD4^+$ OT-II cells. We conclude that GO pretreatment of BMDCs produces significant immunomodulatory antigen presentation resulting in a variety of tolerogenic $CD4^+$ and $CD8^+$ T cell phenotypes in vitro that we hypothesize could dampen pathogenic immune responses via a variety of known mechanisms, including induction of exhaustion of pathogenic T cells and expansion of the Treg population.

4.3 Unreported Results

4.3.1 Exposure to GAS6-associated antigen biases both T cell and APC phenotypes toward tolerance in a T cell dependent manner

We then asked if efferocytic antigen collection and presentation via GAS6 modulated APC phenotype independent of T cell co-culture and investigated whether these phenotypic changes were dependent on the PS-binding function of γ-carboxylated GO. To investigate this, we repeated the experimental format shown in Fig. 4.2 with saline compared to GO and ΔGO-treated groups (Fig. 4.3). Previously, we found that γ-carboxylation on GAS6 was required to drive rapid uptake in vitro. Thus, we asked if γ-carboxylation on GAS6 was also neces-

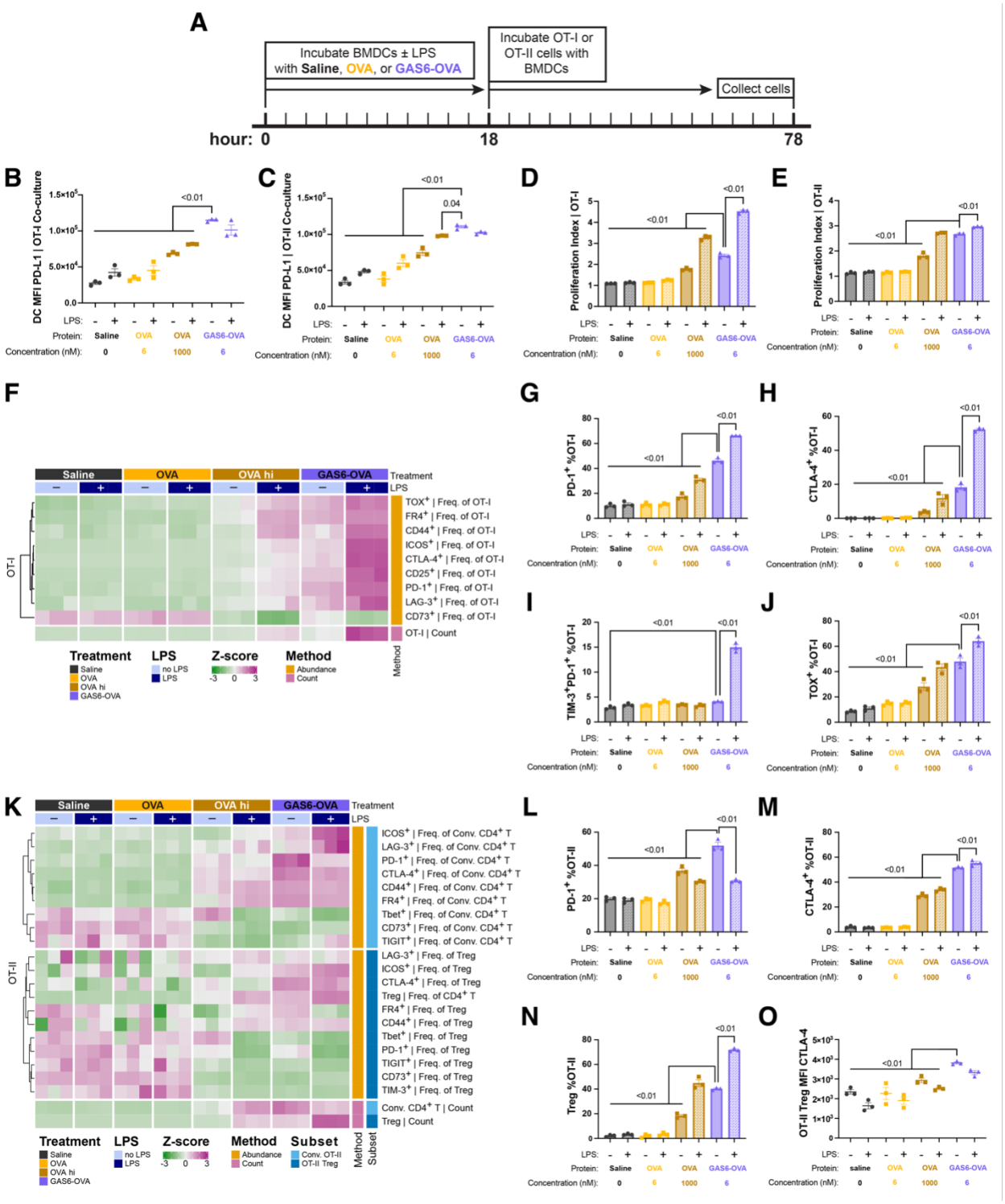

Figure 4.2: **GAS6-mediated efferocytic antigen collection drives antigen processing and presentation by DCs in vitro, stimulating T cell proliferation while inducing tolerance-associated T cell phenotypes.** (A) Experimental timeline detailing the in vitro co-culture of BMDCs with OT-I or OT-II T cells following incubation with free antigen or GAS6-fused antigen.

(Continued)(B) PD-L1 MFI on BMDCs co-cultured with OT-I T cells across treatment groups. (C) PD-L1 MFI on BMDCs co-cultured with OT-II T cells across treatment groups. (D) Proliferation index quantification for OT-I T cells. (E) Proliferation index quantification for OT-II T cells. (F) Heatmap displaying Z-scored expression of immune markers on OT-I T cells across treatment conditions (Saline, OVA, OVA hi, GO ± LPS). Rows are clustered by Euclidean distance. (G) Percentage of PD-1+ cells within the OT-I T cell population. (H) Percentage of CTLA-4+ cells within the OT-I T cell population. (I) Percentage of TIM-3+PD-1+ cells within the OT-I T cell population. (J) Percentage of TOX+ cells within the OT-I T cell population. (K) Heatmap displaying Z-scored expression of immune markers on conventional and regulatory OT-II T cells across treatment conditions. Rows are clustered by Euclidean distance. (L) Percentage of PD-1+ cells within the conventional OT-II T cell population. (M) Percentage of CTLA-4+ cells within the conventional OT-II T cell population. (N) Percentage of FoxP3+CD25+ Tregs within the OT-II T cell population in the co-culture. (O) CTLA-4 MFI on OT-II Tregs.

sary for enhanced antigen presentation. Interestingly, ΔGO drove significant proliferation of OVA-specific $CD4^+$ and $CD8^+$ T cells compared to saline-treated controls, however, to a far lesser extent than GO-treated groups, especially for cross-presentation to prime $CD8^+$ T cells (Fig. 4.3A-D). Interestingly, in the absence of T cells in co-culture, GO treatment did not alter DC phenotype. APC phenotype was significantly altered in a γ-carboxylation- and T-cell-dependent manner in the presence of OT-I cells. In the presence of OT-II cells, APC phenotype was altered in a T cell-dependent, but γ-carboxylation-independent manner (Fig. 4.3E). Tolerogenic PD-L1 and TAM receptor (MerTK, Axl) expression and MFI on BMDCs was significantly upregulated in both OT-I and OT-II co-culture, however PD-L1 expression in OT-I co-culture displayed a far stronger γ-carboxylation dependence than co-culture with OT-II cells (Fig. 4.3E-K). In OT-I and OT-II co-culture, MHC I and MHC II expression on BMDCs was significantly upregulated in ΔGO-treated groups compared to saline controls. However, abundance and intensity of MHC I and MHC II expression in GO-treated BMDCs were significantly increased compared to both ΔGO-treated groups and saline treated controls, indicating that, in the context of both $CD8^+$ and $CD4^+$ T cell co-cultures, γ-carboxylation is necessary to induce the full extent of observed immunomodulation (Fig. 4.3L-O). ICOSL has been shown to support Treg differentiation.44 ICOSL

MFI on BMDCs was upregulated only after co-culture with OT-I and OT-II cells but independently of γ-carboxylation (Fig. 4.3P). OX40L is a well-characterized marker of activation in APCs and acts as a co-stimulatory signal in T cells,(45,46) leading to their long-term survival and function. In contrast to ICOSL expression, significant upregulation of OX40L MFI on BMDCs was dependent on both T cell co-culture and γ-carboxylation of GAS6 (Fig. 4.3Q). CD86 is an activation marker on APCs that can deliver inhibitory co-stimulation to CTLA-4^+ T cells.(47) Significant upregulation of CD86 MFI on BMDCs was γ-carboxylation-dependent on OT-I cells but γ-carboxylation-independent on OT-II cells. Taken together, many phenotypic changes in APCs induced by antigen-specific $CD4^+$ T cell co-culture are independent of Gla domain γ-carboxylation on GAS6. These phenotypic APC changes are sometimes recapitulated in co-culture with $CD8^+$ T cells, but only when the GO is γ-carboxylated. These observed phenotypic changes in BMDCs were absent unless co-cultured with T cells, indicating that either direct or indirect interaction between DCs and T cells is required for phenotypic modulation of BMDCs by their efferocytic antigen presentation. No phenotypic changes were found to be independent of Gla γ-carboxylation in both OT-I cells and OT-II cells, suggesting that efferocytic mechanisms decoupled from inhibition of secondary necrosis may be T cell dependent.

4.4 Continued:Re-analyzed and Re-Interpreted Previously Reported Results

4.4.1 Antigen exposure via GAS6 Promotes Tolerogenic T cell Responses in vivo Even in Inflammatory Contexts in a PS-Binding Dependent Manner.

Given our observations in vitro of the interplay between DC and T cells to drive tolerogenic phenotypes in both the myeloid and lymphoid side when antigen was associated with the

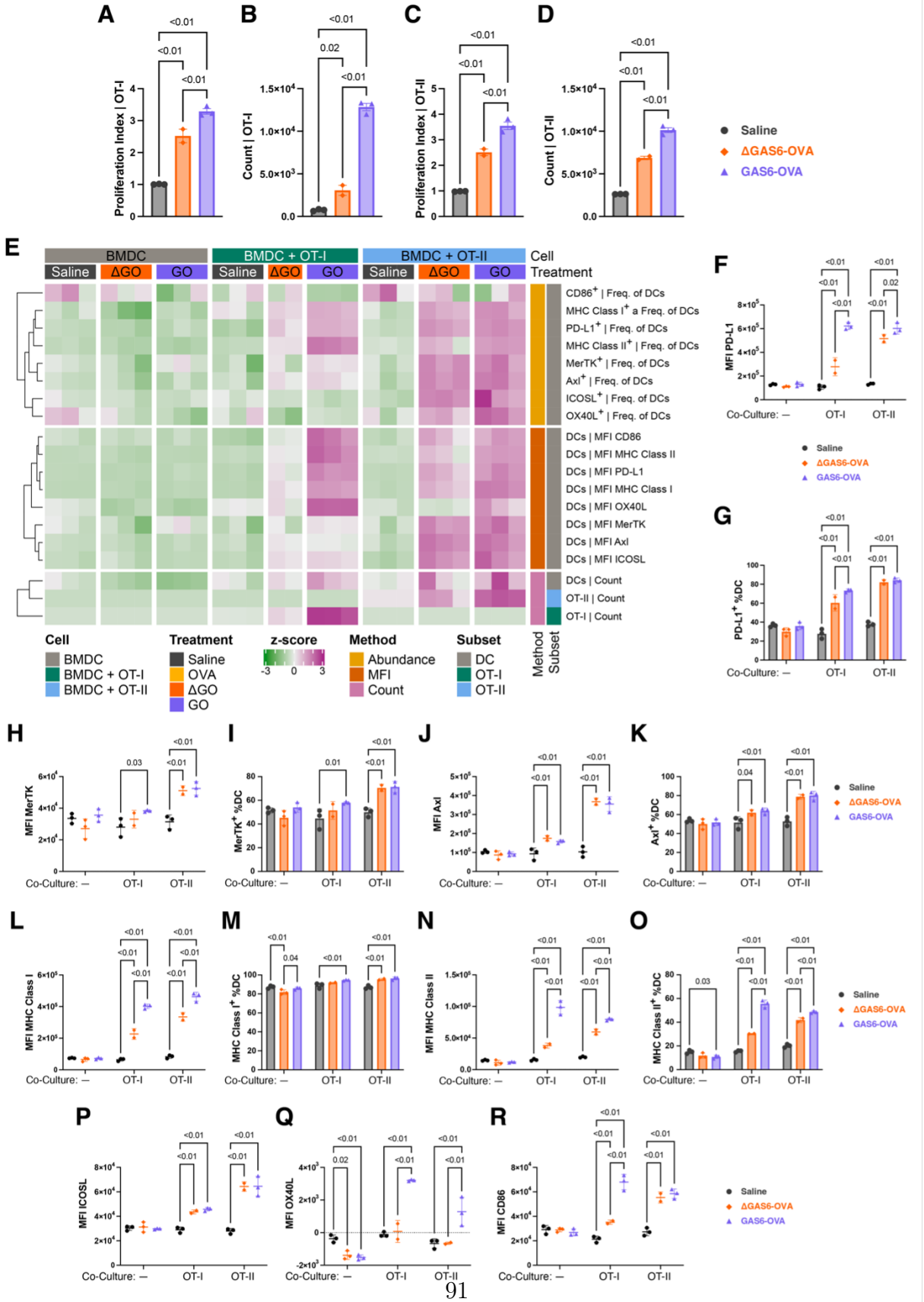

Figure 4.3: **PS-binding capacity shapes GAS6 mediated efferocytic processing to drive DC phenotype toward tolerance in a T cell-dependent manner in vitro.**

(Continued)Fig. 4.3 utilizes the same experimental schema as depicted in Fig. 4.2A. (A) OT-I T cell proliferation index following co-culture with BMDCs that had been incubated with antigen, comparing saline (black circles), ΔGO (orange diamonds), and GO (purple triangles). (B) Absolute counts of recovered OT-I T cells post-co-culture. (C) OT-II T cell proliferation index following co-culture with antigen-pulsed BMDCs. (D) Absolute counts of recovered OT-II T cells post-co-culture. (E) Heatmap displaying Z-scored BMDC characteristics (abundance, counts, MFI, viability) grouped by co-culture (BMDC, BMDC + OT-I, BMDC + OT-II) and antigen treatment. Rows are clustered by Euclidean distance. (F) PD-L1 MFI on BMDCs under different conditions: monoculture or co-culture with OT-I or OT-II T cells. (G) Percentage of PD-L1$^+$ BMDCs across conditions described in (E). (H) MerTK MFI on BMDCs. (I) Percentage of MerTK$^+$ DCs. (J) Axl MFI on BMDCs. (K) Percentage of Axl$^+$ BMDCs. (L) MHC Class I MFI on BMDCs. (M) Percentage of MHC Class I$^+$ BMDCs. (N) MHC Class II MFI on BMDCs. (O) Percentage of MHC Class II$^+$ DCs. (P) ICOSL MFI on BMDCs. (Q) OX40L MFI on BMDCs. (R) CD86 MFI on BMDCs.

efferocytic modulator GAS6, we explored this process in vivo. For this, we adoptively transferred OT-I and OT-II cells into wild-type C57BL/6 mice and dosed them with GO, OVA, or saline. We then challenged the mice with an emulsion of adjuvant and antigen to stimulate adaptive immune responses, reasoning that a blunting of the response to challenge would indicate a tolerogenic bias due GAS6-mediated antigen exposure (Fig. 4.4A). In the lymph nodes and spleen, GO-treated, but not ΔGO-treated mice exhibited a significant reduction in proportion of OT-I T cells compared to both saline- and OVA-treated controls (Fig. 4.4B; Fig. S3A). Similarly, OT-II cells were significantly reduced in the lymphoid organs of GO-treated mice compared to saline-treated mice, whereas neither OVA nor ΔGO treatment had significant effects (Fig. 4.4C; Fig. S3B). To determine whether the reduced cell numbers resulted from inhibited proliferation, we tracked cell division in CTV-labeled OT-I and OT-II cells. We observed no significant changes in proliferation across groups in the lymphoid organs (Fig. S4). These findings indicate that GO reduces T cell expansion independent of cell cycle inhibition. Tregs have an active role in dampening and preventing inflammatory responses. In the lymph nodes of adjuvanted antigen-challenged mice, only GO pretreatment resulted in a significantly higher proportion of Tregs within the OT-II population compared to saline-treated groups (Fig. 4.4D); a similar trend was observed in the spleen (Fig. S3C).

The bulk compartment recovery of Tregs was not changed within any treatment groups in the lymphoid organs (Fig. S3D,E). This suggests that only γ-carboxylated GO pretreatment increases the relative abundance of Tregs.

Based on our observation of increased frequency of Tregs upon exposure to γ-carboxylated GAS6-associated antigen, we sought to evaluate any phenotypic responses. We first assessed the expression of the immunomodulatory receptors TIGIT and TIM-3, which act as co-inhibitory receptors(48–50). In the lymph nodes of GO-treated mice, OT-I cells exhibited no change in the proportion of TIM-3 expression compared to OVA- and saline-treated groups (Fig. 4.4E). Splenic OT-I cells showed an increased MFI of TIM-3 staining in GO-treated groups (Fig. S3F). A significantly larger proportion of cells expressing TIGIT was observed in OT-I cells in the lymph nodes (Fig. 4.4F) and in the spleen (Fig. S3G) of GO-treated groups compared to saline and OVA-treated controls. TIGIT expression was also significantly increased on Treg OT-II cells in the spleen (Fig. S3H) and conventional OT-II cells in the draining LNs (Fig. 4.4G). Finally, conventional OT-II cells from GO-treated mice expressed a significantly reduced proportion of CD69 (Fig. 4.4H), an early activation marker,51 while OT-II Tregs were more likely to express Helios (Fig. 4.4I), a marker of Treg phenotypic robustness(52).

We next evaluated markers associated with T cell exhaustion. OT-I cells from GO-treated mice expressed significantly higher levels of TOX in the lymph nodes (Fig. 4.4J) and the spleen (Fig. S3I), suggesting an increased rate of exhaustion among antigen-specific T cells(26,43). Furthermore, conventional OT-II cells recovered from GO-treated lymph nodes exhibited substantially more CTLA-4 expression (Fig. 4.4K), which is known to compete for costimulatory ligands and suppress T cell activation(53,54). Finally, OT-II Treg populations in the lymph nodes expressed significantly higher levels of FR4 (Fig. 4.4L) and CD73 (Fig. 4.4M), both of which are associated with suppressive capacity(33,55–57). Together, these data indicate that exposure of antigen associated with GAS6 suppresses T

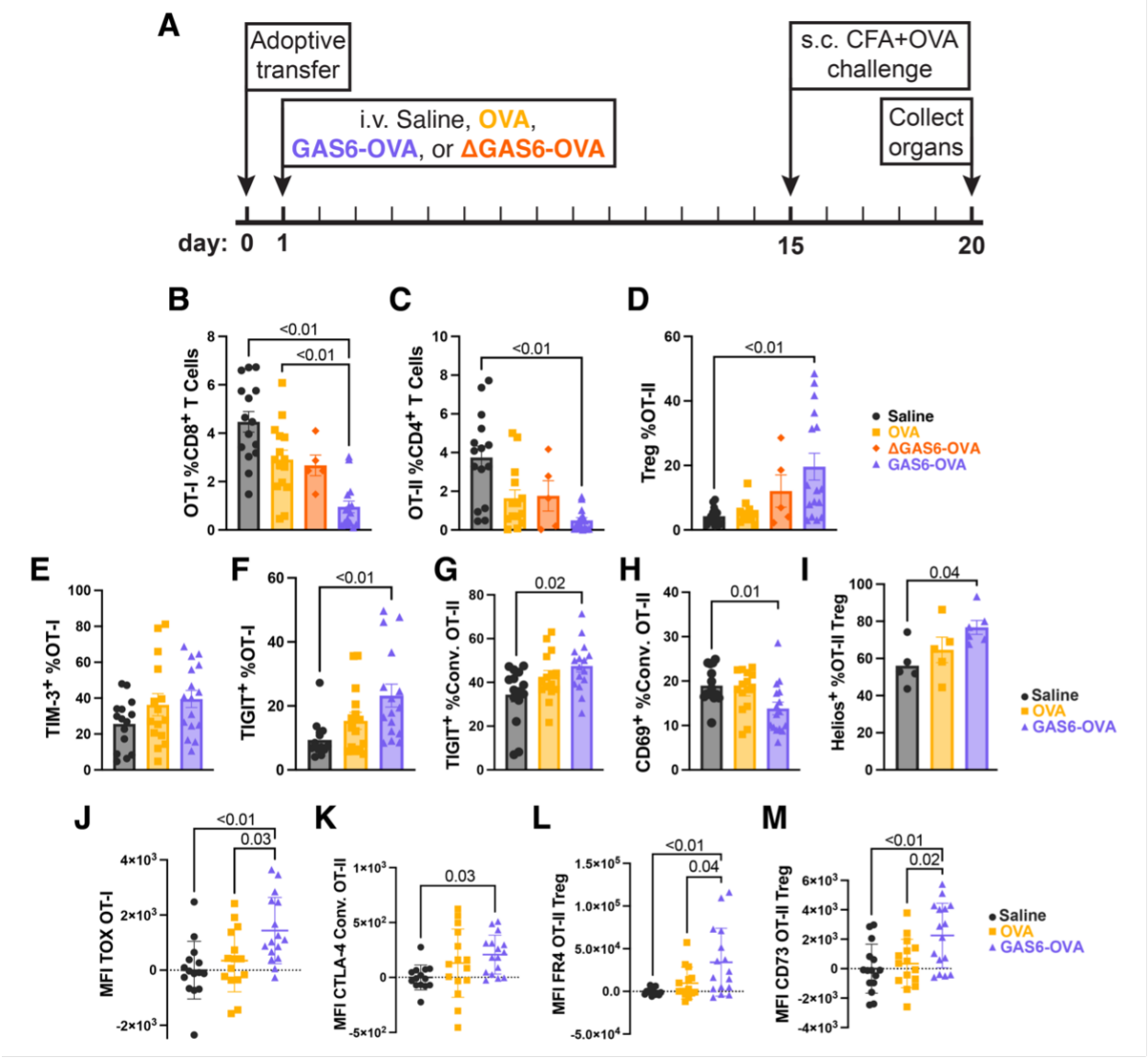

Figure 4.4: **Antigen exposure via the GAS6 pathway of efferocytosis promotes tolerance-associated phenotypes in vivo and blunts response to inflammatory antigen challenge.** (A) Experimental timeline detailing adoptive transfer of OT-I/OT-II cells, intravenous treatment administration, subcutaneous challenge, and endpoint analysis. Fig. 4.4B-M concern cells isolated from the draining lymph nodes of the challenge site. (B) Abundance of OT-I cells as a percentage of the $CD8^+$ T cell compartment. (C) Abundance of OT-II cells as a percentage of the $CD4^+$ T cell compartment. (D) Abundance of $FoxP3^+CD25^+$ regulatory T cells within the OT-II compartment. (E) Percentage of $TIM\text{-}3^+$ OT-I cells. (F) Percentage of $TIGIT^+$ OT-I cells. (G) Percentage of $TIGIT^+$ conventional OT-II cells. (H) Percentage of $CD69^+$ conventional OT-II cells. (I) Percentage of $Helios^+$ cells within the OT-II Treg subset. (J) MFI of TOX on OT-I cells. (K) MFI of CTLA-4 on conventional OT-II cells. (L) MFI of FR4 on OT-II Tregs. (M) MFI of CD73 on OT-II Tregs.

cell responses to antigen exposure even in an inflammatory context by reducing the abundance of antigen-specific cells, promoting the induction or survival of Tregs, and modifying immunoregulatory receptor expression across T cell subsets.

4.4.2 Antigen exposure via GAS6 prevents hallmark characteristics of allergic airway inflammation

To evaluate whether the regulatory biases observed in the adoptive transfer model described above could occur in endogenous T cell populations and could protect from challenge, we investigated the effect of GO in an in vivo model of allergic airway inflammation, exposing GAS6-associated antigen systemically via GO, sensitizing systemically with a Th2-biasing adjuvant, and then repeatedly challenging the airways to the model allergen (Fig. 4.5A). Bronchoalveolar lavage (BAL) IgE, a well-accepted driver of allergic pathology, was significantly reduced in GO-treated mice followed by sensitization (Fig. 4.5B). Severe asthmatic pathology is characterized by goblet cell hypersecretion of mucin, as well as changes in spatial organization of the alveolar space(58–61). Periodic acid-Schiff (PAS) stains mucin-containing goblet cells in the airway epithelia (Fig. 4.5C-F). Pretreatment with GO, but not OVA, significantly reduced mucin hypersecretion (Fig. 4.5G), suggesting an attenuation of pathological tissue repose and remodeling downstream of allergenic challenge. H&E staining demonstrated reduced cellular infiltration into the airway parenchyma (Fig. S5A-D).

Eosinophil infiltration into the airway space and lung parenchyma is known to drive pathological responses to allergen in allergic airway inflammation(62–64). Thus, we tested whether antigen pre-exposure via GAS6 association induces tolerance to OVA, as would be evidenced by reduced airway eosinophilia following challenge. Interestingly, the relative abundance of eosinophils in the $CD45^{+}$ compartment had a bimodal distribution in the BAL and lung samples of the GO-treated group (Fig. 4.5H,I). Levels of eosinophilia in the BAL and lung samples were robustly correlated (Fig. S5E). To further evaluate the

effects of GAS6-associated antigen preexposure on allergic airway inflammation, we examined the distribution of eosinophils among $CD45^+$ cells using a threshold analysis. To separate non-responders from responders, we categorized mice based on whether the percentage of eosinophils among $CD45^+$ cells in the BAL was below or above a 50% threshold (Fig. 4.5J). A significantly higher proportion of mice in the GO-exposed group exhibited eosinophil levels below this threshold compared to both sensitized but untreated and OVA-treated controls, suggesting a shift toward a less inflammatory phenotype in responders. These results show that antigen-exposure via the efferocytic mediator GAS6 can bias immune responses with endogenous populations and can prevent pathology to an inflammatory antigen challenge, here in the context of allergic airway inflammation.

4.5 Discussion

The current paradigm for efferocytosis-induced immune response proposes that multiple pathways are required for tolerance induction other than simple inhibition of secondary necrosis. For instance, MerTK signaling by efferocytic bridge proteins has proven indispensable for this tolerogenic effect, with even a mono-allelic knockout of MerTK sufficient to cause rampant autoimmune pathology. Decoupling the anti-inflammatory effects of efferocytic signaling from clearance of cellular debris is necessary to further characterize discrete pathways contributing to this incompletely understood immunological phenomenon. Antigen presentation, an important component of immune activation and tolerance, remains an incompletely characterized aspect of efferocytic immune regulation. Antigen processing from apoptotic debris plays an important role inducing and maintaining tolerance to proteins in the periphery, some of which may not be present in thymic central tolerogenic processes. For example, in Type 1 diabetes, peripheral neoantigens arise following aberrant post-translational modifications. The current proposed model asserts efferocytosis as a driver of tolerogenic antigen presentation and suppressor of inflammatory activities in innate immune cells, but it is un-

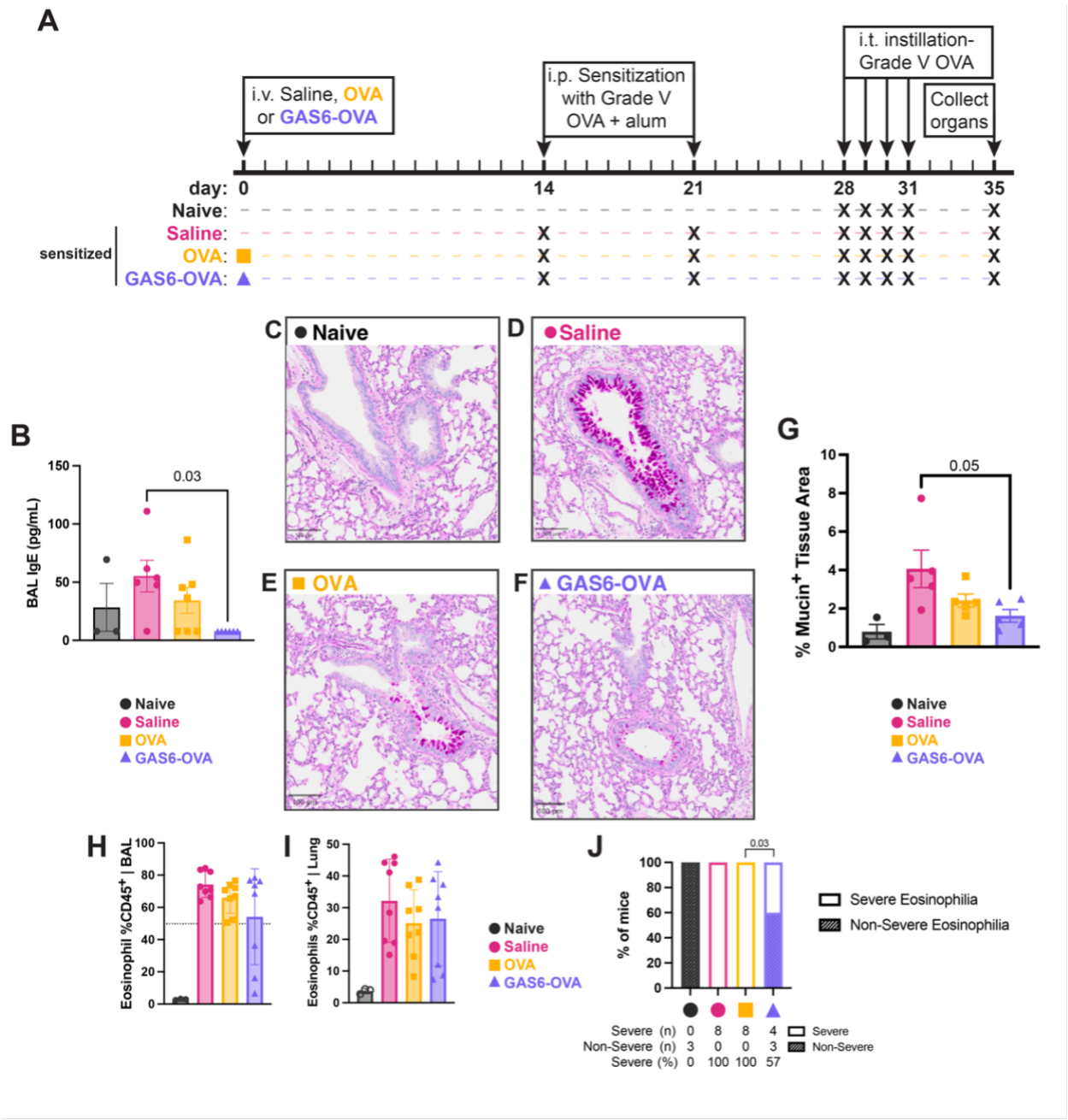

Figure 4.5: **Antigen exposure via the GAS6 pathway of efferocytosis blunts response to inflammatory antigen challenge and characteristic pathology of allergic airway inflammation.** (A) Experimental timeline for the allergic airway inflammation model, including prophylactic treatment, sensitization, challenge, and analysis points. (B) IgE concentration in bronchoalveolar lavage (BAL) fluid. (C) Representative periodic acid-Schiff (PAS)-stained lung section from a naïve mouse. (D) Representative PAS-stained lung section from a sensitized mouse. (E) Representative PAS-stained lung section from an OVA-treated mouse. (F)Representative PAS-stained lung section from a GO-treated mouse.

(Continued)(G) Quantification of the PAS-positive area percentage in lung tissue sections. (H) Percentage of eosinophils among $CD45^+$ cells in BAL fluid. (I) Percentage of eosinophils among $CD45^+$ cells in lung tissue. (J) Contingency analysis showing the proportion of mice per group with eosinophils exceeding 50% of $CD45^+$ cells in BAL.

clear how antigen presentation is modulated or how it contributes to the anti-inflammatory phenotype found in disease contexts.

Secondary necrosis leads to the release of inflammatory mediators, effectively adjuvanting the local microenvironment and potentiating inflammatory presentation of antigens, even those derived from self. Thus, inhibition of secondary necrosis has confounded prior research attempting to understand how efferocytosis modulates antigen-specific immunity. It is difficult to discern whether efferocytosis-associated tolerance results from simple suppression of environmental inflammatory cues versus distinct immunomodulatory cellular signaling or presentation of antigen. Previous attempts using models of apoptotic debris, such as loading antigen within PS-containing liposomes, have probed this question, but, because PS engages several components of efferocytic machinery, cannot probe the necessity and sufficiency of specific pathways. Here, we seek to provide insight into one such path by engineering a suite of novel fusion proteins to decouple the endocytic function of efferocytosis from the TAM receptor stimulation: first, GO, the fully functional bridge protein GAS6 fused to a model antigen OVA, and second, ΔGO, a non-PS binding variant (Fig. 4.1). We sought to explore the function of the GAS6/TAM receptor-mediated tolerogenic pathway both under quiescent and inflamed conditions, exploring the effects of efferocytic antigen presentation on target T cells and on the APCs.

GO demonstrated significantly increased antigen-coupled uptake compared to mixing controls and even very high doses of OVA (Fig. 4.1F,G), indicating that association of OVA to GAS6 was necessary for enhanced antigen uptake. GO, furthermore, exhibited strong preferential affinity for PS. This antigen uptake was temperature-dependent, suggesting uptake may occur via receptor-mediated endocytosis (Fig. S1). This supports the hypothesis

that efferocytic bridge proteins facilitate specific uptake without inducing broad pinocytosis, an important consideration for modulating immunity with antigen specificity. ΔGO is not rapidly taken up by cells, suggesting it does not lead TAM-receptor-bearing APCs to perform efferocytosis (Fig. 4.1E). Prior research reports that bridging molecules such as GAS6, lacking the dying cell linkage required for receptor internalization, still maintain signaling capacity when bound to TAM receptors. These data confirm the hypothesis that GO, but not ΔGO, enables TAM receptor internalization, associated with phagocytosis of dying cells, via specific affinity to PS.

We utilized our single engineered molecule stimulating efferocytosis to characterize the effects of efferocytosis on antigen specific T cell immunity in the OT model system in vitro (Fig. 4.2) and in vivo (Fig. 4.4). Due to strong proliferation of both OT-I $CD8^+$ and OT-II $CD4^+$ T cell populations, we concluded that GO drove antigen processing and subsequent presentation on both MHC I and MHC II (Fig. 4.2). These results contrast with recent claims that efferocytosis reduces MHC expression and thus antigen presentation, resulting in more tolerogenic phenotypes. There may be components of efferocytic machinery besides GAS6 that lead to such a phenomenon. However, here we show that APCs increased expression of both MHC I and II in a linkage-dependent manner (Fig. 4.4B,C), indicating that this mechanism may be coupled to cellular debris clearance. Expansion of Tregs was seen both in vitro and in vivo, suggesting that efferocytosis drives the observed tolerogenic phenotypes and inhibits pathogenesis via active suppression of T cell immunity (Fig. 4.2O, Fig. 4.4D). Furthermore, in vivo, these Tregs exhibited phenotypic shifts associated with robustness, including elevated Helios, FR4, and CD73 (Fig. 4.4I,L,M). Similar to MHC expression, expansion of Treg OT-II cells was dependent on dying cell linkage via PS binding, suggesting delivery of antigen via TAM receptor engagement may be insufficient to produce active tolerance mechanisms without efferocytic clearance. Conventional $CD4^+$ OT-II T cells demonstrated increased expression of CTLA-4 and PD-1, indicating suppressed effector ca-

pacity of non-Treg $CD4^+$ T cells (Fig. 4.2L,M, Fig. 4.4K). In addition to active mechanisms, we observed passive mechanisms of immune suppression, characterized by deletion of both $CD4^+$ and $CD8^+$ T cells in GO-treated groups (Fig. 4.4B,C). In vivo, $CD4^+$ T cells showed further signs of immune suppression, including lower expression of the activation marker CD69 and increased TIGIT expression (Fig. 4.4F,G). Both in vitro and in vivo, we observed strong evidence of terminal exhaustion in the CD8 compartment, including increased expression of TIM-3 and TIGIT (Fig. 4.2I & 4.4E,F). This exhaustion comprises both active suppression in the form of competition for antigen and cytokines as well as passive suppression as pathogenic T cells lose effector capacity. Taken together, these data provide evidence that delivery of antigen via efferocytic GAS6-related pathways leads to both MHC I and MHC II presentation stimulating both active and passive tolerance-inducing phenotypes in $CD4^+$ and $CD8^+$ T cell compartments in a cell-clearance-dependent manner.

Thus, we have presented evidence that efferocytosis-coupled antigen causes tolerogenic antigen-specific T cell responses. We also provide evidence of a reciprocal influence exerted by T cells toward DCs presenting antigen via the GAS6 pathway, biasing them toward tolerance in a T cell dependent manner, with some but not all interactions also requiring PS binding. Thus, phenotypic changes emerged only after antigen-experienced APCs were co-cultured with antigen-specific CD4+ or $CD8^+$ T cells, including upregulation of coinhibitory and costimulatory markers on the APCs (Fig. 4.3E-R), suggesting essential T cell:APC bi-directional communication to enforce a tolerant phenotype on both parties. ΔGO induced significant phenotypic changes in APCs, suggesting MerTK engagement can manipulate immune cell phenotype in the absence of dying cell linkage. However, this Gla-dependent PS linkage more broadly potentiated APC responses (Fig. 4.3); only ICOSL upregulation showed independence from Gla γ-carboxylation in both OT-I and OT-II T cell co-cultures (Fig. 4.3P). Interestingly, many phenotypic changes in OT-II co-culture demonstrated independence of the γ-carboxylation of the Gla domain, indicating that TAM receptor activation

and internalization on APCs in co-culture with $CD4^+$ T cells may influence phenotype to a lesser extent in $CD4^+$ than in $CD8^+$ T cell co-culture (Fig. 4.3E). MHC expression, TAM receptors MerTK and Axl, and co-inhibitory receptor PD-L1 expression were upregulated on DCs in both OT-I and OT-II co-cultures but showed far more γ-carboxylation dependence in $CD8^+$ T cell cultures (Fig. 4.2B-C, Fig. 4.3F-O).

Prior research shows that TLR stimulation, in combination with downstream Type I Interferon signaling, leads to expression of TAM receptors on APCs and subsequent suppression of TLR signaling through NfB. However, others in the field have demonstrated that inflammatory context can "flip" the nature of efferocytosis from tolerizing to immunizing, suggesting nuance in the interplay between differing TLR stimulation and TAM signaling. Incubation of APCs with GO in the presence of inflammatory PAMP stimulation of the cell-surface pattern receptor TLR4 enhanced, rather than dampened, tolerogenic responses to GO. Supporting the hypothesis that efferocytosis acts as a brake on the immune system in the context of inflammation, these data suggest active tolerogenic antigen presentation plays a role in tolerogenic responses to efferocytosis.

Due to the strong bi-directional crosstalk between the target T cell and the presenting DC to modulate the DC toward a tolerogenic program, we investigated naïve immunity with the same xenoantigen (OVA), controlling for prior antigen experience. By enriching the antigen-specific compartment of T cells, adoptive transfer greatly increases the frequency with which we would expect antigen-experienced APCs to encounter cognate T cells. Therefore, immunomodulation seen in the OT model system may result from heightened abundance of antigen-specific T cells. To evaluate whether this heightened abundance was necessary for the observed immunomodulation, we probed effects of GO in a naïve, wild-type mouse, free of adoptive transfer. We utilized an allergic airway inflammation model, characterized by pathological Type 2 responses by endogenous OVA-specific T cells, mimicking the Th2-driven nature of human allergic asthma. In this model, we administered GO before sensitizing to

OVA, such that antigen-specific T cells in the endogenous repertoire were both naïve and at physiological sparse abundance. GO administration indeed mitigated hyperreactivity to OVA as demonstrated by reductions in pathological drivers including mucus hypersecretion and IgE in the airway, without causing obvious immune dysfunction (Fig. 4.5). Importantly, prophylactic exposure to OVA did not significantly inhibit pathogenesis (Fig. 4.5), indicating enhanced tolerizing capabilities of GAS6-associated antigen compared to antigen (here, OVA) exposure alone. Similarly to OVA controls, ΔGO did not yield immunological protection to challenge, suggesting that PS-binding capacity is required for immunological protection (Fig. 4.4B-C). Because we observed tolerogenic immunomodulation in this context, we conclude that tolerance induction by efferocytic antigen fusion can occur even in environments with few antigen-specific T cells, and those being naïve. Given the bi-directional crosstalk, this is important in our model, understanding that it can launch from a naïve state and then self-reinforce.

Secondary necrosis is absent in healthy mice due to endogenous efferocytosis. Thus, we interpret immunological effects of efferocytosis-linked antigen delivery while controlling for inhibition of secondary necrosis. GO effects must then be due to efferocytic clearance, TAM receptor signaling, and downstream antigen presentation. There appears to be tighter control over how efferocytosis regulates $CD8^+$ T cell immunity compared to $CD4^+$ T cell immunity, as implied by the stronger dependence on physical linkage (via Gla:PS interaction) for APC immunomodulation in $CD8^+$ than in $CD4^+$ T cell co-culture experiments. Given that both GO and ΔGO modulated APC phenotype in vitro but only GO drove significant reduction of antigen-specific T cell recovery in vivo, the linkage of antigen with clearance of dying cells in the milieu appears critical for meaningful immunomodulation. Dying cell clearance is known to stimulate metabolism of cellular material, influencing immune cell phenotype. However, receptor signaling is attenuated when receptor crosslinking is absent. Thus, we are unable to confirm if metabolic changes drive outcomes or if stronger receptor signaling would produce

the same results between GO and ΔGO in vivo. Taken together, these results suggest that efferocytosis suppresses pathogenic immunity via exhaustion of antigen-specific $CD8^+$ T cells in a cellular-debris-clearance-dependent manner. These results align with previous reports of enhanced cross-presentation associated with efferocytosis.

Tregs have long been appreciated to mediate dominant tolerance in an antigen-dependent manner, preventing and suppressing inflammatory disease. While Tregs have been shown to promote efferocytosis in macrophages, efferocytosis has also been shown to promote Treg induction by increasing coinhibitory marker expression (ex. CTLA-4) by efferocytes, suggesting a bidirectional relationship. In vitro and in vivo, we observed meaningful expansion of antigen-specific Treg populations only following exposure to GAS6-associated antigen. In vivo, significant expansion of Tregs only occurred with PS-binding GAS6-associated antigen, indicating the importance of linkage of antigen to dying cells. We observed expansion of OT-II Tregs but not the endogenous Treg compartment in vivo, supporting our hypothesis that Treg expansion is antigen specific (Supplementary Fig. 3D-E). Previous research has shown Treg populations with increased Helios, FR4, and CD73 expression to have increased suppressive capacity and commitment to Treg fate(33,52,65). Indeed, exposure to GAS6-associated antigen, but not unmodified antigen, expanded the population of Tregs and increased Treg expression of Helios, FR4, and CD73. Aligning with effects of GAS6-associated antigen on antigen-specific $CD8^+$ T cells, simultaneous exposure of APCs to GAS6-associated antigen and inflammatory stimulation led to significantly increased expansion of antigen-specific Tregs compared to unstimulated groups in vitro. Groups exposed to a large amount of unmodified antigen exhibited the same trend, but had overall less expansion of Tregs compared to GAS6-associated antigen treated groups. Taken together, these data suggest that antigen taken up through efferocytosis significantly promotes Treg expansion. We hypothesize this Treg expansion to mediate the observed suppression of immunity in vivo.

Our tool, GO, allowed direction of one pathway by which antigen is collected and pre-

sented by efferocytosis. We note that there are other mediators that serve as bridge proteins in efferocytosis, such as MFGE-8. We also note that neuraminidases are expressed in apoptosis, leading to remodeling of the cell-surface glycome triggering APC collection by C-type lectins. Our group has explored this latter pathway extensively in murine models of Type 1 diabetes, neuroinflammation, and allergic asthma, in which Tregs have been demonstrated to exert protective effects. Given the high frequency of Tregs generated by GAS6-associated antigen, their robustness, e.g. as indicated by expression of the transcription Helios in combination with FoxP3, and the robustness of the process under inflammatory conditions (at least mimicking a bacterial inflammation, via TLR4), it is conceivable that this pathway may be useful in a translational sense.

4.6 Methods

4.6.1 Design of Recombinant Fusion Proteins

The recombinant fusion protein GO was designed by joining the sequence of murine GAS6 (UniProtKB: Q61592) with chicken ovalbumin (OVA) (UniProtKB: P01012), linked with a flexible glycine-serine (G4S) linker. An 8x histidine tag was added to the C-terminus of the fusion protein to facilitate affinity purification. The fusion protein sequence was cloned into the pSecTag2A vector using standard molecular biology techniques, and the resulting construct was amplified in Escherichia coli DH5-α cells cultured in 2XYT broth with ampicillin (100 μg/mL). Plasmid purification was performed using the QIAprep MaxiPrep Kit (Qiagen).

4.6.2 Transfection in HEK293 Cells

HEK293F cells were cultured in FreeStyle 293 Expression Medium with Glutamax (Gibco #12338-026). Cells were transfected with plasmid encoding GO using Polyethyleneimine

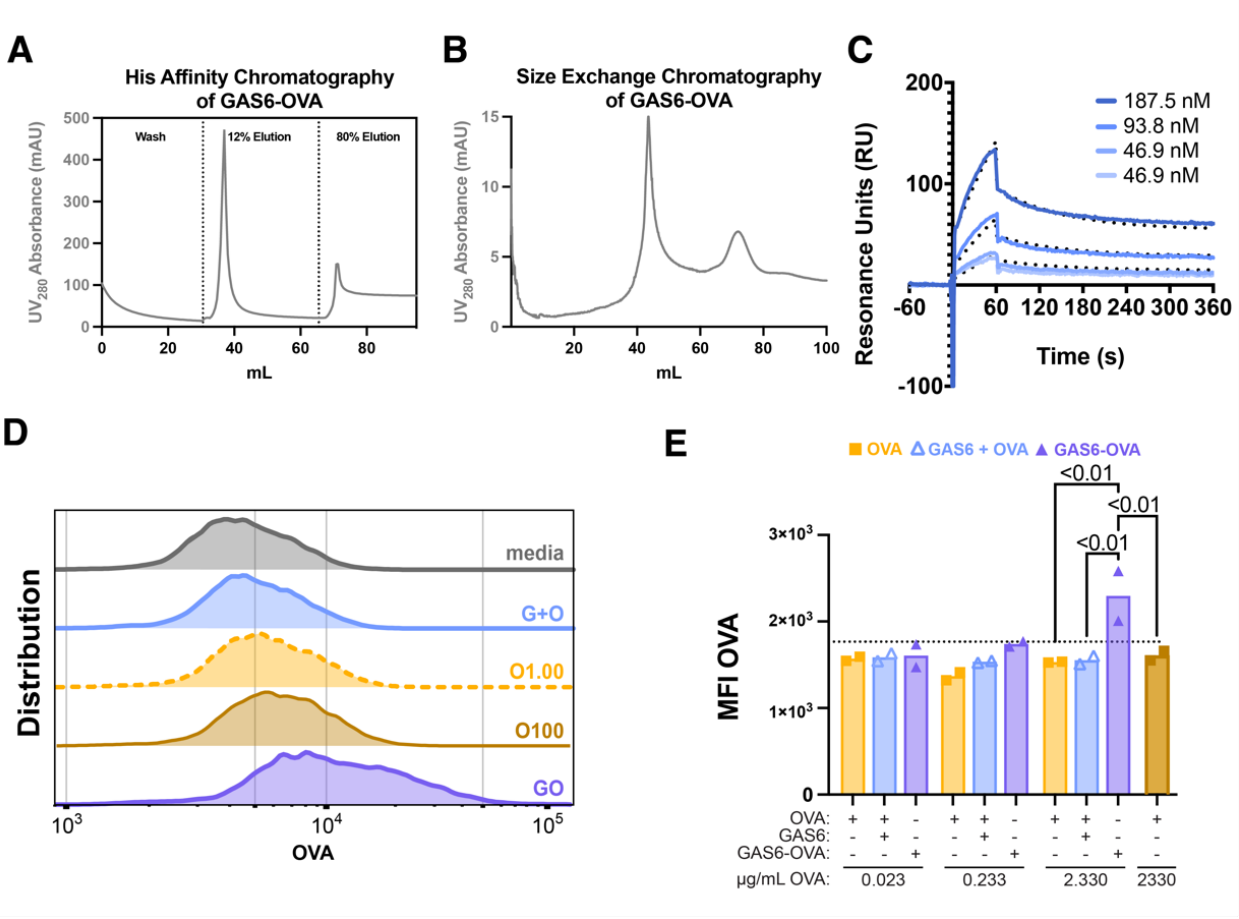

Figure 4.6: **Supplemental Figure 1** Histidine affinity purification (A) and size exclusion purification (B) of GO. (C) Surface Plasmon Resonance (SPR) analysis demonstrating specific binding of wild-type GAS6 to PS-containing liposomes at three concentrations, including two runs of the lowest concentration. This serves as a positive control for the SPR assay in (Fig. 1E). (D) Distribution of fluorescent intensities of OVA staining for BMDCs incubated with media (grey), a mixture of GAS6 and OVA (light blue; G+O), OVA at 1 μg/mL (dashed yellow; O1.00), OVA at 100 μg/mL (brown, O100), or GO at equimolar concentration to O1.00 (purple). (E) BMDC uptake of OVA was assessed at 4C according to the same scheme as Fig. 4.1F

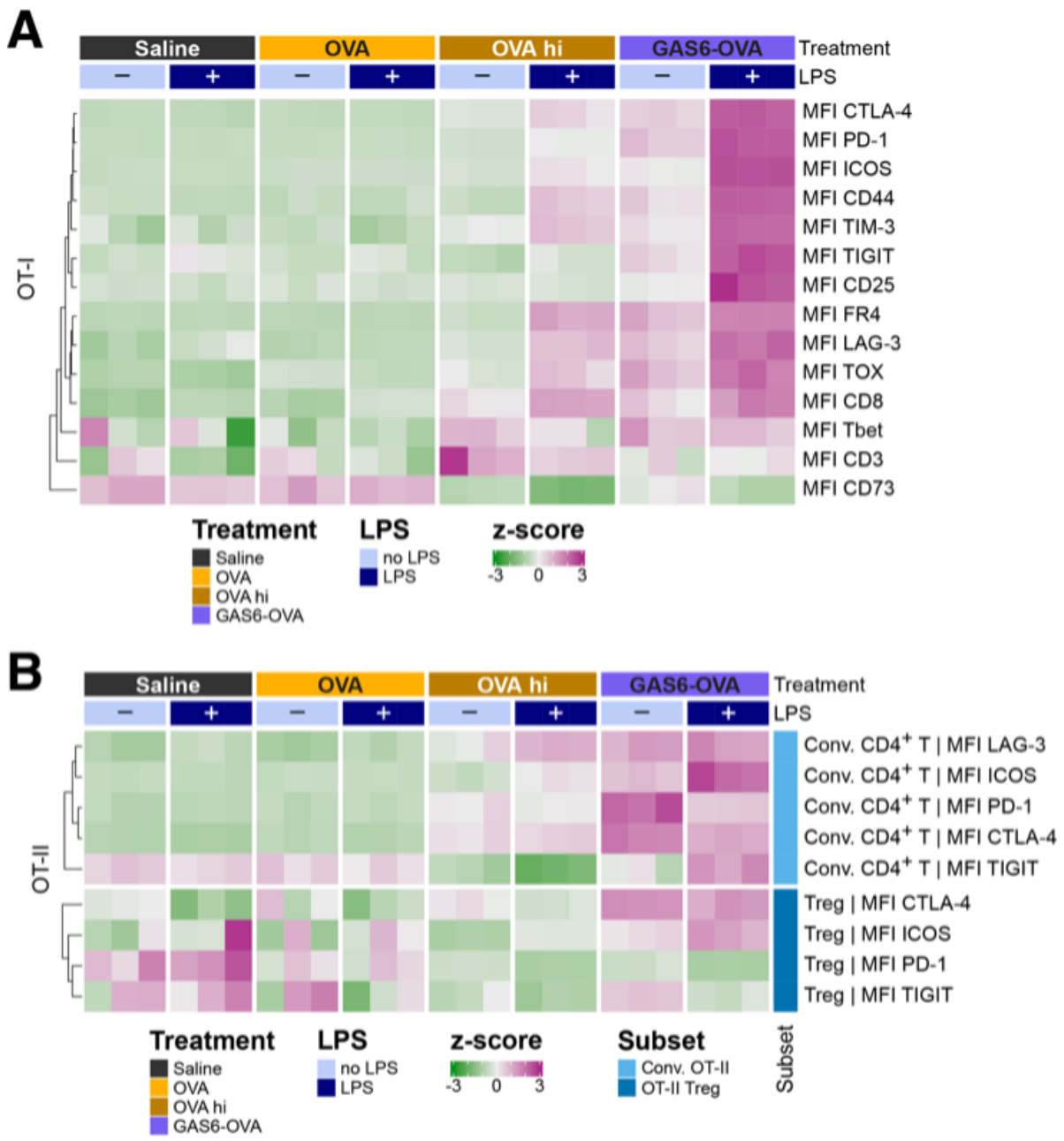

Figure 4.7: **Supplemental Figure 2** (A) Heatmap displaying Z-scored MFI expression of immune markers on OT-I T cells (A) and OT-II T cells (B) across treatment conditions (Saline, OVA, OVA hi, GO ± LPS). Rows are clustered by Euclidean distance.

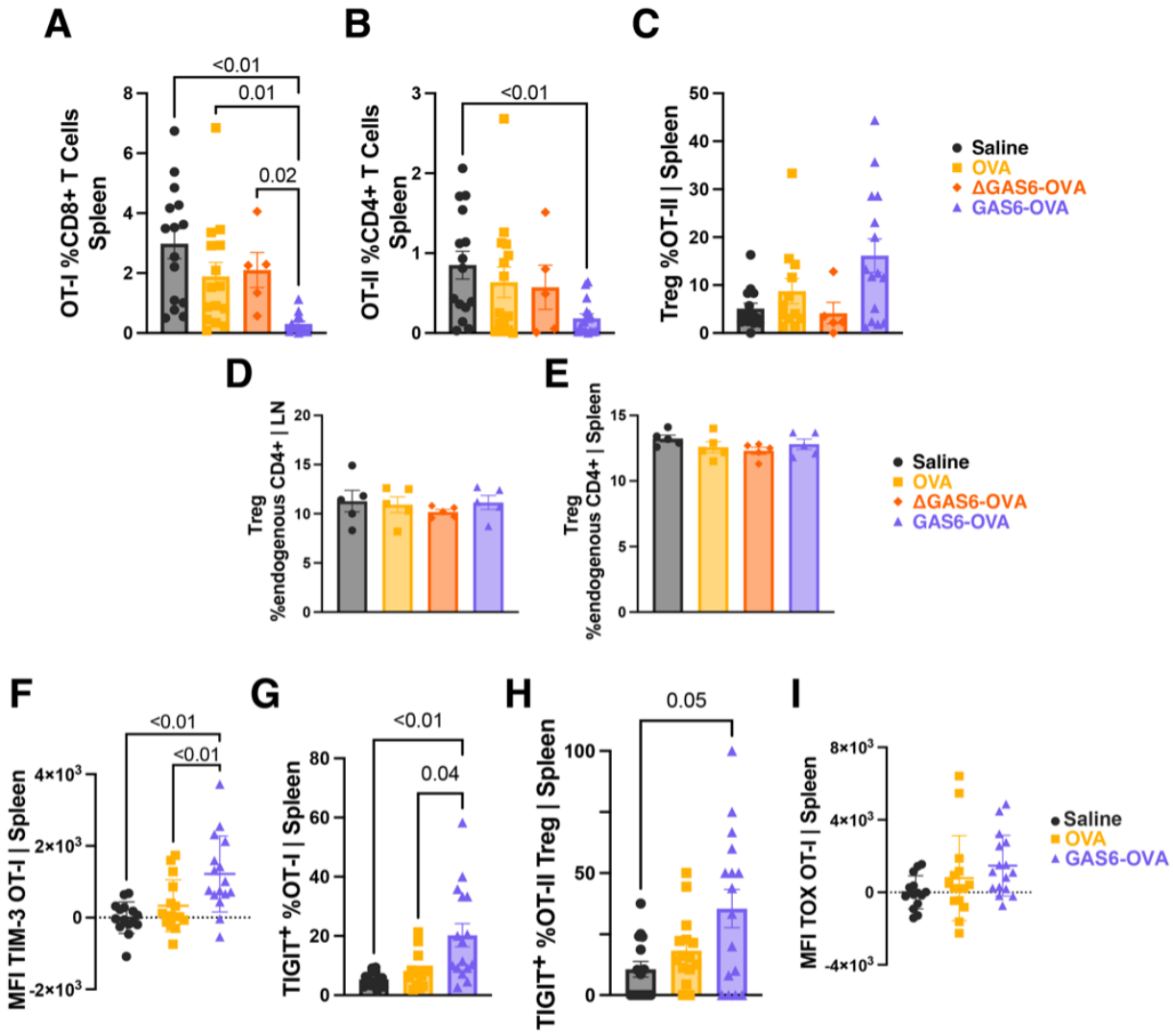

Figure 4.8: **Supplemental Figure 3** Flow cytometric analysis of spleen samples from the same experiment shown for lymph nodes in Fig. 4.3. (A) OT-I cells as a percentage of the $CD8^+$ T cell compartment. (B) OT-II cells as a percentage of the $CD4^+$ T cell compartment. (C) Tregs as a percentage of the OT-II compartment. Relative abundance of Tregs in the bulk $CD4^+$ T cell compartments of cells recovered from the draining LNs (D) and spleen (E). (F) Median fluorescence intensity (MFI) of TIM-3 on OT-I cells. (G) Percentage of $TIGIT^+$ OT-I cells. (H) Percentage of $TIGIT^+$ OT-II Tregs. (I) MFI of TOX on OT-I cells.

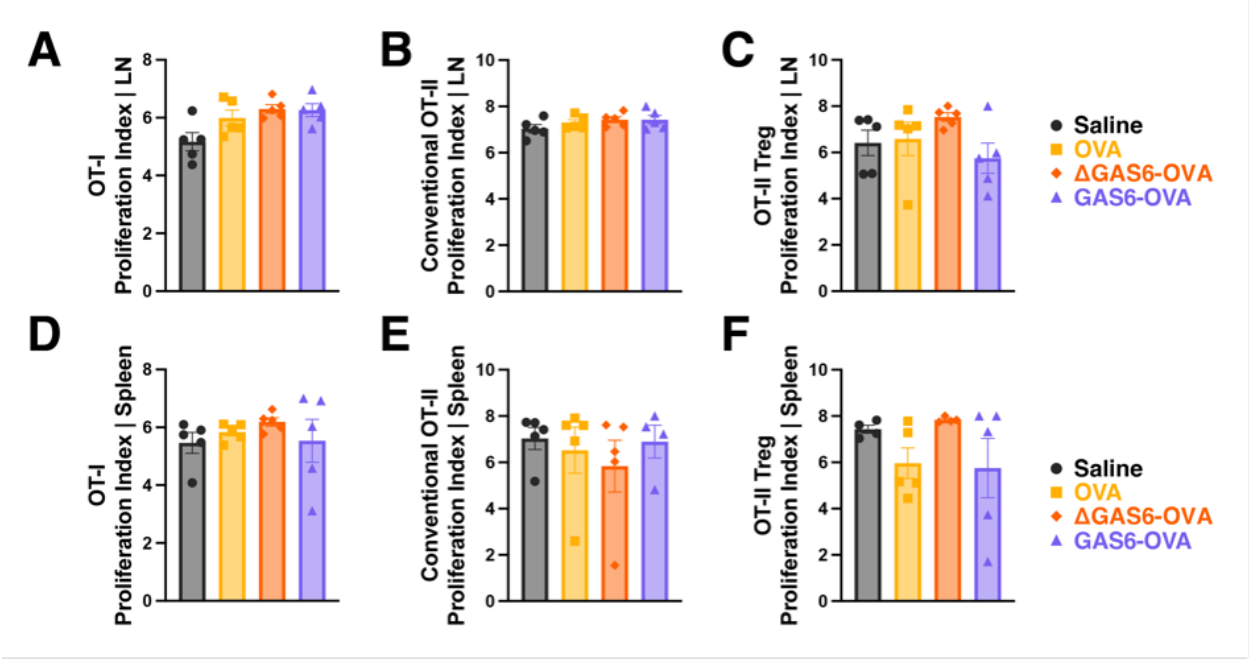

Figure 4.9: **Supplemental Figure 4** (A) Proliferation indices of OT-I cells (A), conventional OT-II cells (B), and FoxP3^{+}CD25^{+} OT-II Tregs (C) isolated from the draining LNs. Proliferation indices of OT-I cells (D), conventional OT-II cells (E), and FoxP3^{+}CD25^{+} OT-II Tregs (F) isolated from the spleen.

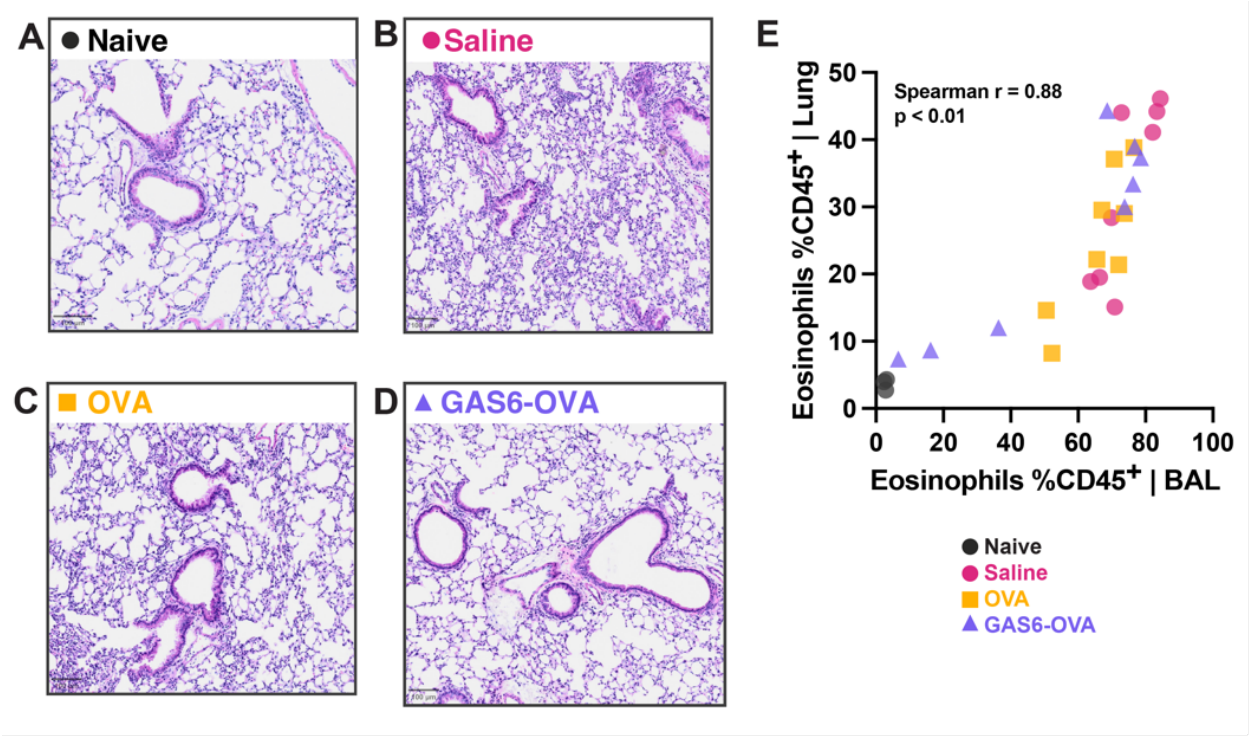

Figure 4.10: **Supplemental Figure 5** (A-D) Representative H&E-stained lung sections displaying mucin-containing airway epithelial cells for the naïve (A), sensitized (B), OVA-treated (C), and GO-treated (D) groups. Scale bar: 100 μm. (E) Scatterplot showing relationship between eosinophil abundance among $CD45^+$ cells in the lung and BAL.

(PEI; Linear, MW 25000, Transfection Grade; Polysciences #23966-1). Transfected cells were cultured for 7 days to allow for protein expression before harvesting and filtering the supernatants containing the secreted recombinant proteins.

4.6.3 Purification via FPLC

Recombinant proteins were purified from HEK293F cell supernatants using an ÄKTA Pure fast protein liquid chromatography (FPLC) system (Cytiva). All chromatography steps were performed at 4°C, and the collected fractions were analyzed by SDS-PAGE to assess purity and to identify the desired protein fractions.

4.6.4 Affinity Chromatography

Histidine-tagged fusion proteins were purified using a HisTrap HP nickel affinity chromatography column (Cytiva). The column was equilibrated with running buffer (20 mM NaH2PO4, 500 mM NaCl, pH 7.4). Cell supernatants were supplemented with imidazole to a final concentration of 15 mM, were loaded onto the column, and the bound proteins were washed with running buffer. Protein elution was performed via a stepwise imidazole gradient, peaking at 300 mM. Fractions containing the desired proteins were collected and pooled for further purification.

4.6.5 Size Exclusion Chromatography

Affinity-purified proteins were further purified by size exclusion chromatography using a HiLoad 16/600 Superdex 200 pg column (Cytiva). The column was equilibrated with PBS. Protein samples were loaded onto the column and eluted with PBS. Fractions corresponding to the monomeric protein peak were collected.

4.6.6 Anion Exchange Chromatography

Anion exchange chromatography was performed for GO using a 5 mL HiScreen Q HP column (Cytiva). The column was equilibrated with running buffer (20 mM Tris, 150 mM NaCl, pH 7.4). GO was supplemented with 4 mM EDTA, loaded onto the column, and washed with running buffer. Elution was carried out using a stepwise gradient of 3 mM CaCl2, 10 mM CaCl2, and 0.5 M NaCl in running buffer. Fractions containing γ-carboxylated GO were collected and stored at -80°C.

4.6.7 Protein Characterization

SDS-PAGE

Purified proteins were analyzed by SDS-PAGE using 4-20% Mini-Protean TGX Stain-Free Gels (Bio-Rad) to assess purity.

Surface Plasmon Resonance (SPR)

Protein-phospholipid interactions were characterized by surface plasmon resonance (SPR) using a Biacore X100 system (Cytiva) with an L1 sensor chip (Cytiva). Liposomes composed of 100% phosphatidylcholine (PC) (Avanti), or 80% PC + 20% phosphatidylserine (PS) (Avanti) were prepared by thin-film hydration and extruded through a 0.22 μm filter. After capturing liposomes on the L1 chip, binding of the fusion proteins was measured in the presence of 4 mM CaCl2.

4.6.8 BMDC Culture

BMDCs were generated from C57BL/6J mice as described by a modified Lutz protocol. Briefly, femurs and tibiae were harvested from 6–15-week-old mice, and bone marrow cells were flushed out using RPMI 1640 medium,The cells were cultured at 3 x 106 cells per 10

cm non-treated dish in 10 mL modified Lutz medium (RPMI 1640 supplemented with 10% fetal bovine serum (FBS), 1% penicillin-streptomycin, 50 μM β-mercaptoethanol (Gibco #21985023), 20 ng/mL GM-CSF (Peprotech #315-03), and 200 ng/mL Flt3L (Peprotech #250-31L)). On day 3, 10 mL fresh medium was added. On day 6, half the medium was replaced. Non-adherent and loosely adherent BMDCs were harvested on day 9 for experiments.

4.6.9 BMDC Uptake Experiments

For uptake experiments, BMDCs were incubated with GO or appropriate controls for 30 minutes at 4°C or 37°C. Cells were then washed with cold FACS buffer (PBS with 2% FBS, 2 mM EDTA), blocked with Fc block, stained with fluorescently labeled anti-CD11c (BV421, BD #565451) and anti-OVA (Rockwell #200-4233) antibodies, and analyzed by flow cytometry.

4.6.10 BMDC:OT Co-Culture

OT-I (CD8+) and OT-II (CD4+) T cells were isolated from mice using magnetic isolation kits (StemCell #19852 & #19853) and labeled with CellTrace Violet (CTV; Thermo #C34557). BMDCs were incubated with GO, OVA (produced in-house in mammalian culture), SIINFEKL, or ISQ peptides with or without 5 ng/mL LPS, for 18-24 hours. Stimulated BMDCs were then washed and co-cultured with CellTrace Violet-labeled OT-I or OT-II T cells at a 1:10 ratio for 60 hours. T cell proliferation was assessed by CellTrace Violet dilution using flow cytometry.

4.6.11 Mice

B6 (C57BL/6J, Stock No: 000664), OT-I (C57BL/6-Tg(TcraTcrb)1100Mjb/J, Stock No: 003831), and OT-II (B6.Cg-Tg(TcraTcrb)425Cbn/J, Stock No: 004194) mice were originally

purchased from The Jackson Laboratory and were subsequently bred in-house with B6 mice bearing CD45.1. All mice were housed under specific pathogen-free conditions in the animal facilities at the University of Chicago. Experiments were performed in accordance with the guidelines of the Institutional Animal Care and Use Committee (IACUC).

4.6.12 OT Adoptive Transfer Model

For adoptive transfer experiments, on day 0, OT-I and OT-II T cells were isolated and labeled with CTV as described above. OT-I and OT-II cells were injected intravenously into naive B6 recipients (1-3 x 105 cells of each type per mouse). The following day, the mice were administered 0.1-10 μg GO, ΔGO, OVA, or saline via intravenous injection. On day 15, mice were challenged via hock injection with 20 μg OVA emulsified in Complete Freund's Adjuvant (CFA; Thermo #77140). On day 20, spleens, hock-draining lymph nodes, and blood were harvested for flow cytometry.

4.6.13 Allergic Airway Inflammation Model

Allergic airway inflammation was induced in 8–12-week-old B6 mice as follows.

Sensitization and Challenge

Mice were sensitized on days 0 and 7 by intraperitoneal injection of 50 μg OVA (Grade V, Sigma-Aldrich) adsorbed to 1 mg aluminum hydroxide (Imject Alum, Thermo Scientific) in 200 μL saline. GO (2.33 pmol = 0.28 μg per dose), OVA (2.33 pmol = 1 μg per dose) or saline was administered intravenously on day 14. On days 28-31, mice were challenged with 25 μg OVA in 50 μL saline via intratracheal instillation.

Sample Collection

On day 35, mice were sacrificed. Bronchoalveolar lavage (BAL) was performed by instilling and recovering a total of 2.9 mL PBS through the trachea. BAL cells were combined across lavages for flow cytometric analysis. Lungs and mediastinal lymph nodes were harvested for flow cytometry. The caudal lobe of the lung was fixed for histology, described below.

H&E and PAS Histology

Lung tissues were sliced into serial 5-µm-thick sections. They were stained with either periodic acid-Schiff (PAS) or hematoxylin and eosin (H&E) staining, which were performed by the Human Tissue Resources Center at the University of Chicago (RRID:SCR 019199). The University of Chicago Integrated Light Microscopy Core then imaged the slides on an Olympus microscope at 40x (RRID:SCR 019197).

Histological Scoring

Data were analyzed in QuPath with the pixel classifiers described in Gómez Medellín et al.(54) In brief, a pixel classifier identifies features of interest including mucin, airway lining, and blood vessels. Abundance of pixels classified as mucin compared to all classified tissue pixels is analyzed.

4.6.14 Quantitative and Statistical Analysis

Prior to hypothesis testing, outliers were identified and removed using the robust regression and outlier removal (ROUT) method with Q = 1%. All remaining datasets were then subjected to Shapiro–Wilk tests for normality. For datasets in which every group passed normality, we compared group standard deviations: if the ratio of the largest to smallest SD exceeded three, Brown–Forsythe and Welch ANOVA were used; otherwise, ordinary one- or

two-way ANOVA with Tukey's multiple comparison correction was applied. When at least one group failed the normality test, we employed Kruskal–Wallis tests with Dunn's post hoc correction. Pairwise comparisons noted in the captions were performed by unpaired two-tailed t-tests, and contingency analyses (e.g., responder vs. non-responder classification) were evaluated by Fisher's exact test. All statistical tests were two-sided with a significance threshold of $p < 0.05$.

Graphing of all bar plots, scatter plots, and statistical summaries was performed in GraphPad Prism v10.4.2. Heatmaps of Z-scored expression data were generated in R (version 4.4.2) using hierarchical clustering (Euclidean distance, complete linkage) and visualized with the ComplexHeatmap package.55

CHAPTER 5

REFERENCES

5.1 References for Chapter 1

1. Bröer S, and Fairweather SJ. Amino Acid Transport Across the Mammalian Intestine. Comprehensive Physiology. 2019;9(1):343-73.

2. Adibi SA, Gray SJ, and Menden E. The Kinetics of Amino Acid Absorption and Alteration of Plasma Composition of Free Amino Acids After Intestinal Perfusion of Amino Acid Mixtures12. The American Journal of Clinical Nutrition. 1967;20(1):24-33.

3. YD B, M M, S S, S R, and V G. Unconventional Functions of Amino Acid Transporters: Role in Macropinocytosis (SLC38A5/SLC38A3) and Diet-Induced Obesity/Metabolic Syndrome (SLC6A19/SLC6A14/SLC6A6). Biomolecules. 2022;12(2).

4. Preston RL, Schaeffer JF, and Curran PF. Structure-Affinity Relationships of Substrates for the Neutral Amino Acid Transport System in Rabbit Ileum. Journal of General Physiology. 1974;64(4):443-67.

5. Lusis AJ, and Pajukanta P. A treasure trove for lipoprotein biology. Nature Genetics. 2008;40(2):129-30.

6. Barter PJ, Caulfield M, Eriksson M, Grundy SM, Kastelein JJP, Komajda M, et al. Effects of Torcetrapib in Patients at High Risk for Coronary Events. New England Journal of Medicine. 2007;357(21):2109-22.

7. Effects of Anacetrapib in Patients with Atherosclerotic Vascular Disease. New England Journal of Medicine. 2017;377(13):1217-27.

8. Hussain SM, and McNeil JJ. An HDL Cholesterol paradox. Cardiovascular Drugs and Therapy. 2025.

9. Feingold KR. Introduction to lipids and lipoproteins. Endotext [internet]. 2024.

10. Randolph GJ, and Miller NE. Lymphatic transport of high-density lipoproteins and chylomicrons. The Journal of Clinical Investigation. 2014;124(3):929-35.

11. Du Y, Li X, Su C, Xi M, Zhang X, Jiang Z, et al. Butyrate protects against high-fat diet-induced atherosclerosis via up-regulating ABCA1 expression in apolipoprotein

E-deficiency mice. British Journal of Pharmacology. 2020;177(8):1754-72.

12. Softic S, Cohen DE, and Kahn CR. Role of Dietary Fructose and Hepatic De Novo Lipogenesis in Fatty Liver Disease. Digestive Diseases and Sciences. 2016;61(5):1282-93.

13. Smith GI, Shankaran M, Yoshino M, Schweitzer GG, Chondronikola M, Beals JW, et al. Insulin resistance drives hepatic de novo lipogenesis in nonalcoholic fatty liver disease. The Journal of Clinical Investigation. 2020;130(3):1453-60.

14. Park EJ, Lee JH, Yu G-Y, He G, Ali SR, Holzer RG, et al. Dietary and Genetic Obesity Promote Liver Inflammation and Tumorigenesis by Enhancing IL-6 and TNF Expression. Cell. 2010;140(2):197-208.

15. Ramachandran P, Dobie R, Wilson-Kanamori JR, Dora EF, Henderson BEP, Luu NT, et al. Resolving the fibrotic niche of human liver cirrhosis at single-cell level. Nature. 2019;575(7783):512-8.

16. Wang X, He Q, Zhou C, Xu Y, Liu D, Fujiwara N, et al. Prolonged hypernutrition impairs TREM2-dependent efferocytosis to license chronic liver inflammation and NASH development. Immunity. 2023;56(1):58-77.e11.

17. O'Neill LA, Kishton RJ, and Rathmell J. A guide to immunometabolism for immunologists. Nature reviews immunology. 2016;16(9):553-65.

18. Tannahill GM, Curtis AM, Adamik J, Palsson-McDermott EM, McGettrick AF, Goel G, et al. Succinate is an inflammatory signal that induces IL-1βthrough HIF-1α. Nature. 2013;496(7444):238-42.

19. Puchalska P, Martin SE, Huang X, Lengfeld JE, Daniel B, Graham MJ, et al. Hepatocyte-Macrophage Acetoacetate Shuttle Protects against Tissue Fibrosis. Cell Metabolism. 2019;29(2):383-98.e7.

20. Loft A, Schmidt SF, Caratti G, Stifel U, Havelund J, Sekar R, et al. A macrophage-hepatocyte glucocorticoid receptor axis coordinates fasting ketogenesis. Cell Metabolism. 2022;34(3):473-86.e9.

21. Guilliams M, Bonnardel J, Haest B, Vanderborght B, Wagner C, Remmerie A, et al. Spatial proteogenomics reveals distinct and evolutionarily conserved hepatic macrophage niches. Cell. 2022;185(2):379-96.e38.

22. Tosello-Trampont A-C, Landes SG, Nguyen V, Novobrantseva TI, and Hahn YS. Kuppfer Cells Trigger Nonalcoholic Steatohepatitis Development in Diet-induced Mouse Model through Tumor Necrosis Factor-α Production*. Journal of Biological Chemistry. 2012;287(48):40161-72.

23. Jain V, Minhas AMK, Ariss RW, Nazir S, Khan SU, Khan MS, et al. Demographic and Regional Trends of Cardiovascular Diseases and Diabetes Mellitus-Related Mortality in the United States From 1999 to 2019. The American Journal of Medicine. 2023;136(7):659-68.e7.

24. Roy P, Orecchioni M, and Ley K. How the immune system shapes atherosclerosis: roles of innate and adaptive immunity. Nature reviews Immunology. 2022;22(4).

25. Engelen SE, Robinson AJB, Zurke Y-X, and Monaco C. Therapeutic strategies targeting inflammation and immunity in atherosclerosis: how to proceed? Nature Reviews Cardiology. 2022;19(8):522-42.

26. Tacke F, Alvarez D, Kaplan TJ, Jakubzick C, Spanbroek R, Llodra J, et al. Monocyte subsets differentially employ CCR2, CCR5, and CX3CR1 to accumulate within atherosclerotic plaques. The Journal of Clinical Investigation. 2007;117(1):185-94.

27. Collins T, and Cybulsky MI. NFκB: pivotal mediator or innocent bystander in atherogenesis? The Journal of Clinical Investigation. 2001;107(3):255-64.

28. P L, PM R, and GK H. Progress and challenges in translating the biology of atherosclerosis. Nature. 2011;473(7347).

29. UK S, S F, and MF L. Residual cardiovascular risk despite optimal LDL cholesterol reduction with statins: the evidence, etiology, and therapeutic challenges. Current atherosclerosis reports. 2012;14(1).

30. Zhao Z, Du S, Shen S, Luo P, Ding S, Wang G, et al. Comparative efficacy and safety of lipid-lowering agents in patients with hypercholesterolemia: A frequentist network meta-analysis. Medicine. 2019;98(6).

31. Cheeley MK, Saseen JJ, Agarwala A, Ravilla S, Ciffone N, Jacobson TA, et al. NLA scientific statement on statin intolerance: a new definition and key considerations for ASCVD risk reduction in the statin intolerant patient. Journal of Clinical Lipidology. 2022;16(4):361-75.

32. Ridker PM. Residual inflammatory risk: addressing the obverse side of the atherosclerosis prevention coin. European Heart Journal. 2016;37(22):1720-2.

33. Ridker PM, Everett BM, Thuren T, MacFadyen JG, Chang WH, Ballantyne C, et al. Antiinflammatory Therapy with Canakinumab for Atherosclerotic Disease. New England Journal of Medicine. 2017;377(12):1119-31.

34. Tardif J-C, Kouz S, Waters DD, Bertrand OF, Diaz R, Maggioni AP, et al. Efficacy and Safety of Low-Dose Colchicine after Myocardial Infarction. New England Journal of Medicine. 2019;381(26):2497-505.

35. Nidorf SM, Fiolet ATL, Mosterd A, Eikelboom JW, Schut A, Opstal TSJ, et al. Colchicine in Patients with Chronic Coronary Disease. New England Journal of Medicine. 2020;383(19):1838-47.

36. Ketelhuth DFJ, Lutgens E, Bäck M, Binder CJ, Van den Bossche J, Daniel C, et al. Immunometabolism and atherosclerosis: perspectives and clinical significance: a position paper from the Working Group on Atherosclerosis and Vascular Biology of the European Society of Cardiology. Cardiovascular Research. 2019;115(9):1385-92.

37. Abbate A, Trankle CR, Buckley LF, Lipinski MJ, Appleton D, Kadariya D, et al. Interleukin-1 Blockade Inhibits the Acute Inflammatory Response in Patients With ST-Segment–Elevation Myocardial Infarction. Journal of the American Heart Association. 2020;9(5):e014941.

38. El Sayed H, Kerensky R, Stecher M, Mohanty P, and Davies M. A randomized phase II study of Xilonix, a targeted therapy against interleukin 1α, for the prevention of superficial femoral artery restenosis after percutaneous revascularization. Journal of Vascular Surgery. 2016;63(1):133-41.e1.

39. Broch K, Anstensrud AK, Woxholt S, Sharma K, Tøllefsen IM, Bendz B, et al. Randomized Trial of Interleukin-6 Receptor Inhibition in Patients With Acute ST-Segment Elevation Myocardial Infarction. JACC. 2021;77(15):1845-55.

40. Furze RC, Molnar J, Parr NJ, Ahmad F, Henry Y, Howe D, et al. Phase 1 and preclinical profiling of ESM-HDAC391, a myeloid-targeted histone deacetylase inhibitor, shows enhanced pharmacology and monocytopaenia. Br J Clin Pharmacol. 2022;88(12):5238-56.

41. Bradshaw D, Abramowicz I, Bremner S, Verma S, Gilleece Y, Kirk S, et al. Hepmarc: A 96 week randomised controlled feasibility trial of add-on maraviroc in people with HIV and non-alcoholic fatty liver disease. PLOS ONE. 2023;18(7):e0288598.

42. Cipriani S, Francisci D, Mencarelli A, Renga B, Schiaroli E, D'Amore C, et al. Efficacy of the CCR5 Antagonist Maraviroc in Reducing Early, Ritonavir-Induced Atherogenesis and Advanced Plaque Progression in Mice. Circulation. 2013;127(21):2114-24.

43. Bot I, Ortiz Zacarías NV, de Witte WEA, de Vries H, van Santbrink PJ, van der Velden D, et al. A novel CCR2 antagonist inhibits atherogenesis in apoE deficient mice by achieving high receptor occupancy. Scientific Reports. 2017;7(1):52.

44. Živković L, Asare Y, Bernhagen J, Dichgans M, and Georgakis MK. Pharmacological Targeting of the CCL2/CCR2 Axis for Atheroprotection: A Meta-Analysis of Preclinical Studies. Arteriosclerosis, Thrombosis, and Vascular Biology. 2022;42(5):e131-e44.

45. Ma H, Yang L, Liu Y, Yan R, Wang R, Zhang P, et al. Butyrate suppresses atherosclerotic inflammation by regulating macrophages and polarization via GPR43/HDAC-miRNAs axis in ApoE$^{-/-}$ mice. PLOS ONE. 2023;18(3):e0282685.

46. Nicholls SJ, Ray KK, Johansson JO, Gordon A, Sweeney M, Halliday C, et al.

Selective BET Protein Inhibition with Apabetalone and Cardiovascular Events: A Pooled Analysis of Trials in Patients with Coronary Artery Disease. American Journal of Cardiovascular Drugs. 2018;18(2):109-15.

47. Davie JR. Inhibition of Histone Deacetylase Activity by Butyrate. The Journal of Nutrition. 2003;133(7):2485S-93S.

48. Bondarev AD, Attwood MM, Jonsson J, Chubarev VN, Tarasov VV, and Schiöth HB. Recent developments of HDAC inhibitors: Emerging indications and novel molecules. British Journal of Clinical Pharmacology. 2021;87(12):4577-97.

49. Elmarasi M, Elmakaty I, Elsayed B, Elsayed A, Zein JA, Boudaka A, et al. Phenotypic switching of vascular smooth muscle cells in atherosclerosis, hypertension, and aortic dissection. Journal of Cellular Physiology. 2024;239(4):e31200.

50. Gallerand A, Dolfi B, Stunault MI, Caillot Z, Castiglione A, Strazzulla A, et al. Glucose metabolism controls monocyte homeostasis and migration but has no impact on atherosclerosis development in mice. Nature Communications. 2024;15(1):9027.

51. Jiang L, Wang, J., Liu, Z., Jiang, A., Li, S., Wu, D., Zhang, Y., Zhu, X., Zhou, E., Wei, Z., & Yang, Z. Sodium butyrate alleviates lipopolysaccharide-induced inflammatory responses by down-regulation of NFκB, NLRP3 signaling pathway, and activating histone acetylation in bovine macrophages. Frontiers in veterinary science. 2020.

52. Volpatti LR, Matos SNd, Borjas G, Reda J, Watkins EA, Zhou Z, et al. LDL-Binding IL-10 Reduces Vascular Inflammation in Atherosclerotic Mice. bioRxiv. 2024:2024.03.04.582839.

53. Li AC, Brown KK, Silvestre MJ, Willson TM, Palinski W, and Glass CK. Peroxisome proliferator–activated receptor γ ligands inhibit development of atherosclerosis in LDL receptor–deficient mice. The Journal of Clinical Investigation. 2000;106(4):523-31.

54. Aguilar EC, Leonel AJ, Teixeira LG, Silva AR, Silva JF, Pelaez JMN, et al. Butyrate impairs atherogenesis by reducing plaque inflammation and vulnerability and decreasing NFκB activation. Nutrition, Metabolism and Cardiovascular Diseases. 2014;24(6):606-13.

55. Courties G, Heidt T, Sebas M, Iwamoto Y, Jeon D, Truelove J, et al. In Vivo Silencing of the Transcription Factor IRF5 Reprograms the Macrophage Phenotype and Improves Infarct Healing. Journal of the American College of Cardiology. 2014;63(15):1556-66.

56. Duewell P, Kono H, Rayner KJ, Sirois CM, Vladimer G, Bauernfeind FG, et al. NLRP3 inflammasomes are required for atherogenesis and activated by cholesterol crystals. Nature. 2010;464(7293):1357-61.

57. Shinohara M, Hirata K-i, Yamashita T, Takaya T, Sasaki N, Shiraki R, et al. Local Overexpression of Toll-Like Receptors at the Vessel Wall Induces Atherosclerotic Lesion Formation. Arteriosclerosis, Thrombosis, and Vascular Biology. 2007;27(11):2384-91.

58. Mullick AE, Tobias PS, and Curtiss LK. Modulation of atherosclerosis in mice by Toll-like receptor 2. The Journal of Clinical Investigation. 2005;115(11):3149-56.

59. Moreno-Gonzalez MA, Ortega-Rivera OA, and Steinmetz NF. Two decades of vaccine development against atherosclerosis. Nano Today. 2023;50:101822.

60. Nettersheim FS, De Vore L, and Winkels H. Vaccination in Atherosclerosis. Cells. 2020;9(12):2560.

61. Wolf D, and Ley K. Immunity and Inflammation in Atherosclerosis. Circulation Research. 2019;124(2):315-27.

62. Bigeh A, Sanchez A, Maestas C, and Gulati M. Inflammatory bowel disease and the risk for cardiovascular disease: Does all inflammation lead to heart disease? Trends in Cardiovascular Medicine. 2020;30(8):463-9.

63. Ait-Oufella H, Herbin O, Bouaziz J-D, Binder CJ, Uyttenhove C, Laurans L, et al. B cell depletion reduces the development of atherosclerosis in mice. Journal of Experimental Medicine. 2010;207(8):1579-87.

64. Ma Z, Mao C, Chen X, Yang S, Qiu Z, Yu B, et al. Peptide Vaccine Against ADAMTS-7 Ameliorates Atherosclerosis and Postinjury Neointima Hyperplasia. Circula-

tion. 2023;147(9):728-42.

65. Zhang L, Al-Ammari A, Zhu D, Zhang H, Zhou P, Zhi X, et al. A nanovaccine for immune activation and prophylactic protection of atherosclerosis in mouse models. Nature Communications. 2025;16(1):2111.

66. Fredrikson GN, Hedblad B, Berglund G, Alm R, Ares M, Cercek B, et al. Identification of Immune Responses Against Aldehyde-Modified Peptide Sequences in ApoB Associated With Cardiovascular Disease. Arteriosclerosis, Thrombosis, and Vascular Biology. 2003;23(5):872-8.

67. Fredrikson GN, Björkbacka H, Söderberg I, Ljungcrantz I, and Nilsson J. Treatment with apo B peptide vaccines inhibits atherosclerosis in human apo B-100 transgenic mice without inducing an increase in peptide-specific antibodies. Journal of Internal Medicine. 2008;264(6):563-70.

68. Slieker RC, Warmerdam DO, Vermeer MH, van Doorn R, Heemskerk MHM, and Scheeren FA. Reassessing human MHC-I genetic diversity in T cell studies. Scientific Reports. 2024;14(1):7966.

69. Nus M, Sage AP, Lu Y, Masters L, Lam BYH, Newland S, et al. Marginal zone B cells control the response of follicular helper T cells to a high-cholesterol diet. Nature Medicine. 2017;23(5):601-10.

70. Barrett TJ. Macrophages in Atherosclerosis Regression. Arteriosclerosis, Thrombosis, and Vascular Biology. 2020;40(1):20-33.

71. Glaubitz J, Wilden A, Golchert J, Homuth G, Völker U, Bröker BM, et al. In mouse chronic pancreatitis $CD25^{+}FOXP3^{+}$ regulatory T cells control pancreatic fibrosis by suppression of the type 2 immune response. Nature Communications. 2022;13(1):4502.

72. Arpaia N, Campbell C, Fan X, Dikiy S, van der Veeken J, deRoos P, et al. Metabolites produced by commensal bacteria promote peripheral regulatory T-cell generation. Nature. 2013;504(7480):451-5.

73. Chinen T, Kannan AK, Levine AG, Fan X, Klein U, Zheng Y, et al. An essential role for the IL-2 receptor in Treg cell function. Nature Immunology. 2016;17(11):1322-33.

74. Zhao TX, Sriranjan RS, Tuong ZK, Lu Y, Sage AP, Nus M, et al. Regulatory T-Cell Response to Low-Dose Interleukin-2 in Ischemic Heart Disease. NEJM Evidence. 2022;1(1):EVIDoa2100009.

75. Trøseid M, Andersen GØ, Broch K, and Hov JR. The gut microbiome in coronary artery disease and heart failure: Current knowledge and future directions. eBioMedicine. 2020;52.

76. Kim S, Rigatto K, Gazzana MB, Knorst MM, Richards EM, Pepine CJ, et al. Altered Gut Microbiome Profile in Patients With Pulmonary Arterial Hypertension. Hypertension. 2020;75(4):1063-71.

77. Wang R, Cao S, Bashir MEH, Hesser LA, Su Y, Hong SMC, et al. Treatment of peanut allergy and colitis in mice via the intestinal release of butyrate from polymeric micelles. Nature Biomedical Engineering. 2023;7(1):38-55.

78. Liu Q, Li Y, Song X, Wang J, He Z, Zhu J, et al. Both gut microbiota and cytokines act to atherosclerosis in ApoE$^{-/-}$ mice. Microbial Pathogenesis. 2020;138:103827.

79. Chan YK, Brar MS, Kirjavainen PV, Chen Y, Peng J, Li D, et al. High fat diet induced atherosclerosis is accompanied with low colonic bacterial diversity and altered abundances that correlates with plaque size, plasma A-FABP and cholesterol: a pilot study of high fat diet and its intervention with Lactobacillus rhamnosus GG (LGG) or telmisartan in ApoE$^{-/-}$ mice. BMC Microbiology. 2016;16(1):1-13. 80. Adolph TE, and Tilg H. Western diets and chronic diseases. Nature Medicine. 2024;30(8):2133-47.

81. Mattace Raso G, Simeoli R, Russo R, Iacono A, Santoro A, Paciello O, et al. Effects of Sodium Butyrate and Its Synthetic Amide Derivative on Liver Inflammation and Glucose Tolerance in an Animal Model of Steatosis Induced by High Fat Diet. PLOS ONE. 2013;8(7):e68626.

82. Pan X, Fang X, Wang F, Li H, Niu W, Liang W, et al. Butyrate ameliorates caerulein-induced acute pancreatitis and associated intestinal injury by tissue-specific mechanisms. British Journal of Pharmacology. 2019;176(23):4446-61.

83. Ciarlo E, Heinonen T, Herderschee J, Fenwick C, Mombelli M, Le Roy D, et al. Impact of the microbial derived short chain fatty acid propionate on host susceptibility to bacterial and fungal infections in vivo. Scientific Reports. 2016;6(1):37944.

84. Pant K, Yadav AK, Gupta P, Islam R, Saraya A, and Venugopal SK. Butyrate induces ROS-mediated apoptosis by modulating miR-22/SIRT-1 pathway in hepatic cancer cells. Redox Biology. 2017;12:340-9.

85. Zhou D, Chen Y-W, Zhao Z-H, Yang R-X, Xin F-Z, Liu X-L, et al. Sodium butyrate reduces high-fat diet-induced non-alcoholic steatohepatitis through upregulation of hepatic GLP-1R expression. Experimental & Molecular Medicine. 2018;50(12):1-12.

86. V G, M T, PD P, PM M, and N S. Transporters and receptors for short-chain fatty acids as the molecular link between colonic bacteria and the host. Current opinion in pharmacology. 2013;13(6).

87. den Besten G, Lange K, Havinga R, van Dijk TH, Gerding A, van Eunen K, et al. Gut-derived short-chain fatty acids are vividly assimilated into host carbohydrates and lipids. American Journal of Physiology-Gastrointestinal and Liver Physiology. 2013;305(12):G900-G10.

88. Zhu L-B. In: Zhang Y-C ed. World Journal of Clinical Pediatrics; 2021.

89. Mayorga-Ramos A B-OC, Simancas-Racines D, Guamán LP. Frontiers | Protective role of butyrate in obesity and diabetes: New insights. Frontiers in Nutrition. 2023;9.

90. Yip W, Hughes MR, Li Y, Cait A, Hirst M, Mohn WW, et al. Butyrate Shapes Immune Cell Fate and Function in Allergic Asthma. Frontiers in Immunology. 2021;Volume 12 - 2021.

91. Portincasa PA-O, Bonfrate L, Vacca MA-OX, De Angelis MA-OX, Farella I, Lanza

E, et al. Gut Microbiota and Short Chain Fatty Acids: Implications in Glucose Homeostasis. LID - 10.3390/ijms23031105 [doi] LID - 1105. (1422-0067 (Electronic)).

92. L Z, C L, Q J, and Y Y. Butyrate in Energy Metabolism: There Is Still More to Learn. Trends in endocrinology and metabolism: TEM. 2021;32(3).

93. Hodgkinson K, El Abbar F, Dobranowski P, Manoogian J, Butcher J, Figeys D, et al. Butyrate's role in human health and the current progress towards its clinical application to treat gastrointestinal disease. Clinical Nutrition. 2023;42(2):61-75.

94. Conley BA, Egorin MJ, Tait N, Rosen DM, Sausville EA, Dover G, et al. Phase I study of the orally administered butyrate prodrug, tributyrin, in patients with solid tumors. Clin Cancer Res. 1998;4(3):629-34.

95. Bo T, Gao L, Yao Z, Shao S, Wang X, Proud CG, et al. Hepatic selective insulin resistance at the intersection of insulin signaling and metabolic dysfunction-associated steatotic liver disease. Cell Metabolism. 2024;36(5):947-68.

96. Zhao X. Gender and Age Differences in the Hepatic Consequences of "Humanized" Bile Acid Compositions in Mice. Cellular and Molecular Gastroenterology and Hepatology. 2021;11(4):1207-8.

97. Endo H, Niioka M, Kobayashi N, Tanaka M, and Watanabe T. Butyrate-Producing Probiotics Reduce Nonalcoholic Fatty Liver Disease Progression in Rats: New Insight into the Probiotics for the Gut-Liver Axis. PLOS ONE. 2013;8(5):e63388.

5.2 References for Chapter 2

1. Cao S, Budina E, Raczy MM, Solanki A, Nguyen M, Beckman TN, et al. A serine-conjugated butyrate prodrug with high oral bioavailability suppresses autoimmune arthritis and neuroinflammation in mice. Nature Biomedical Engineering. 2024.

2. V G, M T, PD P, PM M, and N S. Transporters and receptors for short-chain fatty acids as the molecular link between colonic bacteria and the host. Current opinion in phar-

macology. 2013;13(6).

3. YD B, M M, S S, S R, and V G. Unconventional Functions of Amino Acid Transporters: Role in Macropinocytosis (SLC38A5/SLC38A3) and Diet-Induced Obesity/Metabolic Syndrome (SLC6A19/SLC6A14/SLC6A6). Biomolecules. 2022;12(2).

4. Bröer S, and Fairweather SJ. Amino Acid Transport Across the Mammalian Intestine. Comprehensive Physiology. 2019;9(1):343-73.

5. Ciarlo E, Heinonen T, Herderschee J, Fenwick C, Mombelli M, Le Roy D, et al. Impact of the microbial derived short chain fatty acid propionate on host susceptibility to bacterial and fungal infections in vivo. Scientific Reports. 2016;6(1):37944.

6. Jiang L, Wang, J., Liu, Z., Jiang, A., Li, S., Wu, D., Zhang, Y., Zhu, X., Zhou, E., Wei, Z., & Yang, Z. Sodium butyrate alleviates lipopolysaccharide-induced inflammatory responses by down-regulation of NF-B, NLRP3 signaling pathway, and activating histone acetylation in bovine macrophages. Frontiers in veterinary science. 2020.

7. Aguilar EC, Leonel AJ, Teixeira LG, Silva AR, Silva JF, Pelaez JMN, et al. Butyrate impairs atherogenesis by reducing plaque inflammation and vulnerability and decreasing NFκ activation. Nutrition, Metabolism and Cardiovascular Diseases. 2014;24(6):606-13.

8. Cleophas MCP, Ratter JM, Bekkering S, Quintin J, Schraa K, Stroes ES, et al. Effects of oral butyrate supplementation on inflammatory potential of circulating peripheral blood mononuclear cells in healthy and obese males. Scientific Reports. 2019;9(1):775.

9. Bröer S, and Fairweather SJ. Amino Acid Transport Across the Mammalian Intestine. Compr Physiol. 2018;9(1):343-73.

10. Stary HC. Composition and classification of human atherosclerotic lesions. Virchows Arch A Pathol Anat Histopathol. 1992;421(4):277-90.

11. Hansson GK. Inflammation, Atherosclerosis, and Coronary Artery Disease. New England Journal of Medicine. 2005;352(16):1685-95.

12. Zhang L, Liu C, Jiang Q, and Yin Y. Butyrate in Energy Metabolism: There Is Still

More to Learn. Trends in Endocrinology Metabolism. 2021;32(3):159-69.

13. Liu Q, Li Y, Song X, Wang J, He Z, Zhu J, et al. Both gut microbiota and cytokines act to atherosclerosis in ApoE/ mice. Microbial Pathogenesis. 2020;138:103827.

14. Du Y, Li X, Su C, Xi M, Zhang X, Jiang Z, et al. Butyrate protects against high-fat diet-induced atherosclerosis via up-regulating ABCA1 expression in apolipoprotein E-deficiency mice. British Journal of Pharmacology. 2020;177(8):1754-72.

15. Mattace Raso G, Simeoli R, Russo R, Iacono A, Santoro A, Paciello O, et al. Effects of Sodium Butyrate and Its Synthetic Amide Derivative on Liver Inflammation and Glucose Tolerance in an Animal Model of Steatosis Induced by High Fat Diet. PLOS ONE. 2013;8(7):e68626.

16. Zhou D, Chen Y-W, Zhao Z-H, Yang R-X, Xin F-Z, Liu X-L, et al. Sodium butyrate reduces high-fat diet-induced non-alcoholic steatohepatitis through upregulation of hepatic GLP-1R expression. Experimental & Molecular Medicine. 2018;50(12):1-12.

17. Bieghs V, and Trautwein C. The innate immune response during liver inflammation and metabolic disease. Trends in Immunology. 2013;34(9):446-52.

18. Zhao Z, Du S, Shen S, Luo P, Ding S, Wang G, et al. Comparative efficacy and safety of lipid-lowering agents in patients with hypercholesterolemia: A frequentist network meta-analysis. Medicine. 2019;98(6).

19. Tous M, Ferré N, Camps J, Riu F, and Joven J. Feeding apolipoprotein E-knockout mice with cholesterol and fat enriched diets may be a model of non-alcoholic steatohepatitis. Molecular and Cellular Biochemistry. 2005;268(1):53-8.

20. Liang W, Menke AL, Driessen A, Koek GH, Lindeman JH, Stoop R, et al. Establishment of a General NAFLD Scoring System for Rodent Models and Comparison to Human Liver Pathology. PLOS ONE. 2014;9(12):e115922.

21. Facchin S, Vitulo N, Calgaro M, Buda A, Romualdi C, Pohl D, et al. Microbiota changes induced by microencapsulated sodium butyrate in patients with inflammatory bowel

disease. Neurogastroenterology Motility. 2020;32(10):e13914.

22. Gupta N, Martin PM, Prasad PD, and Ganapathy V. SLC5A8 (SMCT1)-mediated transport of butyrate forms the basis for the tumor suppressive function of the transporter. Life Sciences. 2006;78(21):2419-25.

23. Furusawa Y, Obata Y, Fukuda S, Endo TA, Nakato G, Takahas^{hi} D, et al. Commensal microbe-derived butyrate induces the differentiation of colonic regulatory T cells. Nature. 2013;504(7480):446-50.

24. Arpaia N, Campbell C, Fan X, Dikiy S, van der Veeken J, deRoos P, et al. Metabolites produced by commensal bacteria promote peripheral regulatory T-cell generation. Nature. 2013;504(7480):451-5.

25. Luo Q-J, Sun M-X, Guo Y-W, Tan S-W, Wu X-Y, Abassa K-K, et al. Sodium butyrate protects against lipopolysaccharide-induced liver injury partially via the GPR43/ -arrestin-2/NF-B network. Gastroenterology Report. 2020;9(2):154-65.

26. Ordovas JM, Lopez-Miranda J, Perez-Jimenez F, Rodriguez C, Park J-S, Cole T, et al. Effect of apolipoprotein E and A-IV phenotypes on the low density lipoprotein response to HMG CoA reductase inhibitor therapy. Atherosclerosis. 1995;113(2):157-66.

27. Bea AM, Lamiquiz-Moneo I, Marco-Benedí V, Mateo-Gallego R, Pérez-Calahorra S, Jarauta E, et al. Lipid-lowering response in subjects with the p.(Leu167del) mutation in the APOE gene. Atherosclerosis. 2019;282:143-7.

28. Nevzorova YA, Boyer-Diaz Z, Cubero FJ, and Gracia-Sancho J. Animal models for liver disease – A practical approach for translational research. Journal of Hepatology. 2020;73(2):423-40.

29. Ridker PM, Everett BM, Thuren T, MacFadyen JG, Chang WH, Ballantyne C, et al. Antiinflammatory Therapy with Canakinumab for Atherosclerotic Disease. New England Journal of Medicine. 2017;377(12):1119-31.

30. Tardif J-C, Kouz S, Waters DD, Bertrand OF, Diaz R, Maggioni AP, et al. Efficacy

and Safety of Low-Dose Colchicine after Myocardial Infarction. New England Journal of Medicine. 2019;381(26):2497-505.

31. Moreno-Gonzalez MA, Ortega-Rivera OA, and Steinmetz NF. Two decades of vaccine development against atherosclerosis. Nano Today. 2023;50:101822.

32. Davie JR. Inhibition of Histone Deacetylase Activity by Butyrate. The Journal of Nutrition. 2003;133(7):2485S-93S.

33. Pedersen SS, Prause M, Williams K, Barrès R, and Billestrup N. Butyrate inhibits IL-1-induced inflammatory gene expression by suppression of NF-B activity in pancreatic beta cells. Journal of Biological Chemistry. 2022;298(9).

34. Lian J, Nelson R, and Lehner R. Carboxylesterases in lipid metabolism: from mouse to human. Protein Cell. 2018;9(2):178-95.

35. Kim K, Shim D, Lee JS, Zaitsev K, Williams JW, Kim K-W, et al. Transcriptome Analysis Reveals Nonfoamy Rather Than Foamy Plaque Macrophages Are Proinflammatory in Atherosclerotic Murine Models. Circulation Research. 2018;123(10):1127-42.

36. Furze RC, Molnar J, Parr NJ, Ahmad F, Henry Y, Howe D, et al. Phase 1 and pre-clinical profiling of ESM-HDAC391, a myeloid-targeted histone deacetylase inhibitor, shows enhanced pharmacology and monocytopaenia. Br J Clin Pharmacol. 2022;88(12):5238-56.

37. Averbukh LA-O, Turshudzhyan AA-O, Wu DC, and Wu GY. Statin-induced Liver Injury Patterns: A Clinical Review. (2225-0719 (Print)).

38. Volpatti LR, Matos SNd, Borjas G, Reda J, Watkins EA, Zhou Z, et al. LDL-Binding IL-10 Reduces Vascular Inflammation in Atherosclerotic Mice. bioRxiv. 2024:2024.03.04.582839.

39. Wang R, Cao S, Bashir MEH, Hesser LA, Su Y, Hong SMC, et al. Treatment of peanut allergy and colitis in mice via the intestinal release of butyrate from polymeric micelles. Nature Biomedical Engineering. 2023;7(1):38-55.

40. McMurdie PJ, and Holmes S. phyloseq: An R Package for Reproducible Interactive Analysis and Graphics of Microbiome Census Data. PLOS ONE. 2013;8(4):e61217.

41. Valles-Colomer M, Falony G, Darzi Y, Tigchelaar EF, Wang J, Tito RY, et al. The neuroactive potential of the human gut microbiota in quality of life and depression. Nature Microbiology. 2019;4(4):623-32.

5.3 References for Chapter 3

1. deCathelineau, A. M. & Henson, P. M. The final step in programmed cell death: phagocytes carry apoptotic cells to the grave. Essays Biochem. 39, 105–117 (2003).

2. Cohen, P. L. et al. Delayed Apoptotic Cell Clearance and Lupus-like Autoimmunity in Mice Lacking the c-mer Membrane Tyrosine Kinase. J. Exp. Med. 196, 135–140 (2002).

3. Xiong, W. et al. Gas6 and the Tyro 3 receptor tyrosine kinase subfamily regulate the phagocytic function of Sertoli cells. Reproduction 135, 77 (2008).

4. Morioka, S., Maueröder, C. & Ravichandran, K. S. Living on the Edge: Efferocytosis at the Interface of Homeostasis and Pathology. Immunity 50, 1149–1162 (2019).

5. Hanayama, R. et al. Autoimmune disease and impaired uptake of apoptotic cells in MFG-E8-deficient mice. Science 304, 1147–1150 (2004).

6. Kappler, J. W., Roehm, N. & Marrack, P. T cell tolerance by clonal elimination in the thymus. Cell 49, 273–280 (1987).

7. Klein, L., Kyewski, B., Allen, P. M. & Hogquist, K. A. Positive and negative selection of the T cell repertoire: what thymocytes see (and don't see). Nat. Rev. Immunol. 14, 377–391 (2014).

8. Dransfield, I., Zagórska, A., Lew, E. D., Michail, K. & Lemke, G. Mer receptor tyrosine kinase mediates both tethering and phagocytosis of apoptotic cells. Cell Death Dis. 6, e1646–e1646 (2015).

9. Lew, E. D. et al. Differential TAM receptor–ligand–phospholipid interactions delimit differential TAM bioactivities. eLife 3, e03385 (2014).

10. Sen, P. et al. Apoptotic cells induce Mer tyrosine kinase–dependent blockade of

NF-B activation in dendritic cells. Blood 109, 653–660 (2007).

11. Sharif, M. N. et al. Twist mediates suppression of inflammation by type I IFNs and Axl. J. Exp. Med. (2006) doi:10.1084/jem.20051725.

12. Scutera, S. et al. Survival and Migration of Human Dendritic Cells Are Regulated by an IFN--Inducible Axl/Gas6 Pathway1. J. Immunol. 183, 3004–3013 (2009).

13. Zhang, S. et al. Efferocytosis Fuels Requirements of Fatty Acid Oxidation and the Electron Transport Chain to Polarize Macrophages for Tissue Repair. Cell Metab. 29, 443-456.e5 (2019).

14. Jenkins, M. K., Chen, C. A., Jung, G., Mueller, D. L. & Schwartz, R. H. Inhibition of antigen-specific proliferation of type 1 murine T cell clones after stimulation with immobilized anti-CD3 monoclonal antibody. J. Immunol. 144, 16–22 (1990).

15. Bonifaz, L. et al. Efficient Targeting of Protein Antigen to the Dendritic Cell Receptor DEC-205 in the Steady State Leads to Antigen Presentation on Major Histocompatibility Complex Class I Products and Peripheral CD8+ T Cell Tolerance. J. Exp. Med. 196, 1627–1638 (2002).

16. Thomann, A. S. et al. Conversion of anergic T cells into Foxp3-IL-10+ regulatory T cells by a second antigen stimulus in vivo. Front. Immunol. 12, 704578 (2021).

17. Schwartz, R. H. T cell anergy. Annu. Rev. Immunol. 21, 305–334 (2003).

18. Rocha, B., Grandien, A. & Freitas, A. A. Anergy and exhaustion are independent mechanisms of peripheral T cell tolerance. J. Exp. Med. 181, 993–1003 (1995).

19. Bordon, Y. TOX for tired T cells. Nat. Rev. Immunol. 19, 476–476 (2019).

20. Pauken, K. E. et al. Epigenetic stability of exhausted T cells limits durability of reinvigoration by PD-1 blockade. Science 354, 1160–1165 (2016).

21. Fontenot, J. D., Gavin, M. A. & Rudensky, A. Y. Foxp3 programs the development and function of CD4+CD25+ regulatory T cells. Nat. Immunol. 4, 330–336 (2003).

22. Jung, H. et al. Anti-inflammatory clearance of amyloid-β by a chimeric Gas6 fusion

protein. Nat. Med. 28, 1802–1812 (2022).

5.4 References for Chapter 4

1. deCathelineau, A. M. & Henson, P. M. The final step in programmed cell death: phagocytes carry apoptotic cells to the grave. Essays in biochemistry 39, 105–117 (2003).

2. Cohen, P. L. et al. Delayed Apoptotic Cell Clearance and Lupus-like Autoimmunity in Mice Lacking the c-mer Membrane Tyrosine Kinase. Journal of Experimental Medicine 196, 135–140 (2002).

3. Xiong, W. et al. Gas6 and the Tyro 3 receptor tyrosine kinase subfamily regulate the phagocytic function of Sertoli cells. Reproduction 135, 77 (2008).

4. Morioka, S., Maueröder, C. & Ravichandran, K. S. Living on the Edge: Efferocytosis at the Interface of Homeostasis and Pathology. Immunity 50, 1149–1162 (2019).

5. Vago, J. P. et al. Gas6/Axl Axis Activation Dampens the Inflammatory Response in Osteoarthritic Fibroblast-like Synoviocytes and Synovial Explants. Pharmaceuticals (Basel) 16, 703 (2023).

6. Hanayama, R. Autoimmune Disease and Impaired Uptake of Apoptotic Cells in MFG-E8-Deficient Mice. Science 304, 1147–1150 (2004).

7. Kappler, J. W., Roehm, N. & Marrack, P. T cell tolerance by clonal elimination in the thymus. Cell 49, 273–280 (1987).

8. Klein, L., Kyewski, B., Allen, P. M. & Hogquist, K. A. Positive and negative selection of the T cell repertoire: what thymocytes see (and don't see). Nat Rev Immunol 14, 377–391 (2014).

9. Delong, T. et al. Pathogenic CD4 T cells in type 1 diabetes recognize epitopes formed by peptide fusion. Science 351, 711–714 (2016).

10. Dransfield, I., Zagórska, A., Lew, E., Michail, K. & Lemke, G. Mer receptor tyrosine kinase mediates both tethering and phagocytosis of apoptotic cells. Cell death & disease 6,

e1646–e1646 (2015).

11. Lew, E. D. et al. Differential TAM receptor–ligand–phospholipid interactions delimit differential TAM bioactivities. eLife 3, e03385 (2014).

12. Sen, P. et al. Apoptotic cells induce Mer tyrosine kinase–dependent blockade of NF-κB activation in dendritic cells. Blood 109, 653–660 (2007).

13. Zhang, S. et al. Efferocytosis Fuels Requirements of Fatty Acid Oxidation and the Electron Transport Chain to Polarize Macrophages for Tissue Repair. Cell Metab 29, 443-456.e5 (2019).

14. Hanayama, R. et al. Identification of a Factor That Links Apoptotic Cells to Phagocytes. Nature 417, 182–187 (2002).

15. Sharif, M. N. et al. Twist mediates suppression of inflammation by type I IFNs and Axl. Journal of Experimental Medicine (2006) doi:10.1084/jem.20051725.

16. Scutera, S. et al. Survival and Migration of Human Dendritic Cells Are Regulated by an IFN--Inducible Axl/Gas6 Pathway1. The Journal of Immunology 183, 3004–3013 (2009).

17. Rothlin, C. V., Ghosh, S., Zuniga, E. I., Oldstone, M. B. A. & Lemke, G. TAM receptors are pleiotropic inhibitors of the innate immune response. Cell 131, 1124–1136 (2007).

18. Rothlin, C. V., Carrera-Silva, E. A., Bosurgi, L. & Ghosh, S. TAM Receptor Signaling in Immune Homeostasis. Annual Review of Immunology 33, 355–391 (2015).

19. Yin, C., Argintaru, D. & Heit, B. Rab17 mediates intermixing of phagocytosed apoptotic cells with recycling endosomes. Small GTPases 10, 218–226 (2017).

20. Yin, C., Kim, Y., Argintaru, D. & Heit, B. Rab17 mediates differential antigen sorting following efferocytosis and phagocytosis. Cell Death Dis 7, e2529–e2529 (2016).

21. Jenkins, M. K., Chen, C. A., Jung, G., Mueller, D. L. & Schwartz, R. H. Inhibition of antigen-specific proliferation of type 1 murine T cell clones after stimulation with immobilized anti-CD3 monoclonal antibody. Journal of Immunology 144, 16–22 (1990).

22. Bonifaz, L. et al. Efficient Targeting of Protein Antigen to the Dendritic Cell Receptor DEC-205 in the Steady State Leads to Antigen Presentation on Major Histocompatibility Complex Class I Products and Peripheral CD8+ T Cell Tolerance. J Exp Med 196, 1627–1638 (2002).

23. Thomann, A. S. et al. Conversion of anergic T cells into Foxp3-IL-10$^+$ regulatory T cells by a second antigen stimulus in vivo. Frontiers in Immunology 12, 704578 (2021).

24. Schwartz, R. H. T Cell Anergy. Annual Review of Immunology 21, 305–334 (2003).

25. Rocha, B., Grandien, A. & Freitas, A. A. Anergy and exhaustion are independent mechanisms of peripheral T cell tolerance. The Journal of experimental medicine 181, 993–1003 (1995).

26. Bordon, Y. TOX for tired T cells. Nat Rev Immunol 19, 476–476 (2019).

27. Fontenot, J. D., Gavin, M. A. & Rudensky, A. Y. Foxp3 programs the development and function of CD4+CD25+ regulatory T cells. Nat Immunol 4, 330–336 (2003).

28. Walker, L. S. K. & Sansom, D. M. The emerging role of CTLA4 as a cell-extrinsic regulator of T cell responses. Nat Rev Immunol 11, 852–863 (2011).

29. Read, S., Malmström, V. & Powrie, F. Cytotoxic T lymphocyte-associated antigen 4 plays an essential role in the function of CD25(+)CD4(+) regulatory cells that control intestinal inflammation. J Exp Med 192, 295–302 (2000).

30. Maynard, C. L. et al. Regulatory T cells expressing interleukin 10 develop from Foxp3+ and Foxp3- precursor cells in the absence of interleukin 10. Nat Immunol 8, 931–941 (2007).

31. Barthlott, T. CD25+CD4+ T cells compete with naive CD4+ T cells for IL-2 and exploit it for the induction of IL-10 production. International Immunology 17, 279–288 (2005).

32. Antonioli, L., Pacher, P., Vizi, E. S. & Haskó, G. CD39 and CD73 in immunity and inflammation. Trends in Molecular Medicine 19, 355–367 (2013).

33. Deaglio, S. et al. Adenosine generation catalyzed by CD39 and CD73 expressed on regulatory T cells mediates immune suppression. The Journal of Experimental Medicine 204, 1257–1265 (2007).

34. Vatandoost, J. & Pakdaman, S. F. The effects of influencing factors on -carboxylation and expression of recombinant vitamin K dependent coagulation factors. Journal of Biomedicine 1, (2016).

35. Li, G. et al. Construction of a Linker Library with Widely Controllable Flexibility for Fusion Protein Design. Applied microbiology and biotechnology 100, 215–225 (2016).

36. Grinnell, B. W. et al. Gamma-carboxylated isoforms of recombinant human protein S with different biologic properties. Blood 76, 2546–2554 (1990).

37. Cooper, M. A., Hansson, A., Löfås, S. & Williams, D. H. A vesicle capture sensor chip for kinetic analysis of interactions with membrane-bound receptors. Analytical Biochemistry 277, 196–205 (2000).

38. Casey, L. M. et al. Mechanistic contributions of Kupffer cells and liver sinusoidal endothelial cells in nanoparticle-induced antigen-specific immune tolerance. Biomaterials 283, 121457 (2022).

39. Kenison, J. E., Stevens, N. A. & Quintana, F. J. Therapeutic induction of antigen-specific immune tolerance. Nat Rev Immunol 24, 338–357 (2024).

40. McLane, L. M., Abdel-Hakeem, M. S. & Wherry, E. J. CD8 T cell exhaustion during chronic viral infection and cancer. Annual review of immunology 37, 457–495 (2019).

41. Roussel, M. et al. Functional characterization of PD1+ TIM3+ tumor-infiltrating T cells in DLBCL and effects of PD1 or TIM3 blockade. Blood Advances 5, 1816–1829 (2021).

42. Zhou, Q. et al. Coexpression of Tim-3 and PD-1 identifies a CD8+ T-cell exhaustion phenotype in mice with disseminated acute myelogenous leukemia. Blood 117, 4501–4510 (2011).

43. Sekine, T. et al. TOX is expressed by exhausted and polyfunctional human effector

memory CD8 + T cells. Sci. Immunol. 5, eaba7918 (2020).

44. Wang, H. et al. Single-cell RNA-seq analysis identifies the atlas of lymph fluid and reveals a sepsis-related T cell subset. Cell Rep 44, 115469 (2025).

45. Webb, G. J., Hirschfield, G. M. & Lane, P. J. L. OX40, OX40L and Autoimmunity: a Comprehensive Review. Clinic Rev Allerg Immunol 50, 312–332 (2016).

46. Croft, M., So, T., Duan, W. & Soroosh, P. The significance of OX40 and OX40L to T-cell biology and immune disease. Immunological Reviews 229, 173–191 (2009).

47. Frijlink, E. et al. PD-1 or CTLA-4 blockade promotes CD86-driven Treg responses upon radiotherapy of lymphocyte-depleted cancer in mice. J Clin Invest 134, (2024).

48. Yue, C. et al. TIGIT as a Promising Therapeutic Target in Autoimmune Diseases. Front Immunol 13, 911919 (2022).

49. Annese, T., Tamma, R. & Ribatti, D. Update in TIGIT Immune-Checkpoint Role in Cancer. Front Oncol 12, 871085 (2022).

50. Negishi, N. et al. CD155-Transducing Signaling through TIGIT Plays an Important Role in Transmission of Tolerant State and Suppression Capacity. ImmunoHorizons 2, 338–348 (2018).

51. Ziegler, S. F., Ramsdell, F. & Alderson, M. R. The activation antigen CD69. Stem Cells 12, 456–465 (1994).

52. Kim, H.-J. et al. Stable inhibitory activity of regulatory T cells requires the transcription factor Helios. Science 350, 334–339 (2015).

53. Hossen, M. M. et al. Current understanding of CTLA-4: from mechanism to autoimmune diseases. Front. Immunol. 14, (2023).

54. Walunas, T. L. et al. CTLA-4 can function as a negative regulator of T cell activation. Immunity 1, 405–413 (1994).

55. Kalekar, L. A. et al. CD4+ T cell anergy prevents autoimmunity and generates regulatory T cell precursors. Nat Immunol 17, 304–314 (2016).

56. Ernst, P. B., Garrison, J. C. & Thompson, L. F. Much Ado about Adenosine: Adenosine Synthesis and Function in Regulatory T Cell Biology. The Journal of Immunology 185, 1993–1998 (2010).

57. Kobie, J. J. et al. T Regulatory and Primed Uncommitted CD4 T Cells Express CD73, Which Suppresses Effector CD4 T Cells by Converting 5-Adenosine Monophosphate to Adenosine. The Journal of Immunology 177, 6780–6786 (2006).

58. Kirstein, F. et al. Expression of IL-4 receptor on smooth muscle cells is not necessary for development of experimental allergic asthma. Journal of Allergy and Clinical Immunology 126, 347–354 (2010).

59. Dao, D.-P. D. & Le, P. H. Histology, Goblet Cells. StatPearls (2023).

60. Ma, J., Rubin, B. K. & Voynow, J. A. Mucins, mucus, and goblet cells. Chest 154, 169–176 (2018).

61. Dao, D.-P. D. & Le, P. H. Histology, goblet cells. (2020).

62. Miki, H., Pei, H., Gracias, D. T., Linden, J. & Croft, M. Clearance of apoptotic cells by lung alveolar macrophages prevents development of house dust mite-induced asthmatic lung inflammation. Journal of Allergy and Clinical Immunology 147, 1087–1092 (2021).

63. Persson, C. Lysis of primed eosinophils in severe asthma. Journal of Allergy and Clinical Immunology 132, 1459–1460 (2013).

64. Possa, S. S., Leick, E. A., Prado, C. M., Martins, M. A. & Tibério, I. F. Eosinophilic inflammation in allergic asthma. Frontiers in pharmacology 4, 46 (2013).

65. Tian, Y. et al. A novel splice variant of folate receptor 4 predominantly expressed in regulatory T cells. BMC Immunol 13, 30 (2012).

66. Lutz, M. B. et al. An advanced culture method for generating large quantities of highly pure dendritic cells from mouse bone marrow. Journal of immunological methods 223, 77–92 (1999).

67. Gómez Medellín, J. E. et al. Liver-targeted allergen immunotherapy rapidly and

safely induces antigen-specific tolerance to treat allergic airway disease in mice. Science Translational Medicine 17, eadl0406 (2025).

68. Gu, Z., Eils, R. & Schlesner, M. Complex heatmaps reveal patterns and correlations in multidimensional genomic data. Bioinformatics 32, 2847–2849 (2016).